# Single crystal growth and electron spectroscopy of $d^1$-systems

Inaugural-Dissertation
zur
Erlangung des Doktorgrades
der Mathematisch-Naturwissenschaftlichen Fakultät
der Universität zu Köln

vorgelegt von
Holger Roth
aus Siegen

Köln 2008

# Contents

# Chapter 1

# Introduction

One of the most intriguing aspects of transition metal oxides is the wide variety and richness of their physical properties. They display quite often spectacular magnetic and electronic phenomena, including metal-insulator transitions (MIT), colossal magneto-resistance (CMR), superconductivity, spin-state transitions, magneto-optical activity and spin-dependent transport [1, 2]. Although conceptually simple and beautiful, theoretical simplifications in terms of, for instance, a Heisenberg model or a single band Hubbard model turn out to be inadequate [3–5]. It now becomes more and more clear that a full identification of the relevant charge, orbital and spin degrees of freedom of the metal ions involved is needed to understand the intricate balance between band formation and electron-correlation effects. An important example is the manganates [6], where orbital ordering and charge distribution [7] of the Mn ions play an important role for its CMR behavior. For the newly synthesized layered cobaltates, it is the spin state transitions that are thought to govern the CMR and MIT phenomena [8,9]. Another example is $V_2O_3$ [10] and $VO_2$ [11–13] for which it has been found that the orbital occupations across the various MITs change dramatically, leading to a switch of the nearest-neighbor spin-spin correlations so that in turn the effective band widths are strongly modified. This is surprisingly also the case for the ruthenates: here one would expect that the larger band widths of the $4d$ orbitals would make the system to be less correlated, but in reality the orbital switching across the metal-insulator [14–16] or magnetic phase [17] transitions is nevertheless no less dramatic. This indicates that not only electron-electron Coulomb repulsion, but also spin-spin correlations

must be considered in order to understand the transitions.

The class of the $RETiO_3$ (RE = rare earth) materials forms in this context a very interesting 'playground' for the quantitative study of the properties and excitation spectra of correlated oxides. It has the relatively simple perovskite crystal structure, and the Ti ions have (formally) only one electron in their $3d$ shell so that complications related to atomic multiplet effects can be avoided. Yet, the orbital degeneracy together with the presence of a small band gap lead to a number of interesting physics which are then subject of a flurry of detailed experimental and theoretical studies. Efforts are being made for a quantitative analysis as to test the accuracy of various theoretical approaches.

$LaTiO_3$ is an antiferromagnetic insulator with a pseudocubic perovskite crystal structure [18–20]. The Néel temperature varies between $T_N = 130$ and 146 K, depending on the exact oxygen stoichiometry [20–22]. Interestingly, a reduced total moment of about 0.45-0.57 $\mu_B$ in the ordered state has been observed [20–22]. One could speculate that this suggests the presence of an orbital angular momentum that is antiparallel to the spin momentum in the $Ti^{3+}$ $3d^1$ ion [22, 23]. Recently, however, Keimer *et al.* [24] have carried out neutron scattering experiments and observed that the spin wave spectrum of $LaTiO_3$ is nearly isotropic with a very small gap. They suggested that therefore the orbital momentum must be quenched. To explain the reduced moment, they proposed the presence of strong orbital fluctuations in the system. This seems to be supported by the theoretical study of Khaliullin and Maekawa [25], who suggested that $LaTiO_3$ is in an orbital liquid state. This is a very exciting proposition, since if true, this would in fact constitute a completely novel state of matter.

Nevertheless, Cwik *et al.* [20], Mochizuki and Imada [26], as well as Pavarini *et al.* [27] estimated that small orthorhombic distortions present in $LaTiO_3$ would produce a crystal field (CF) splitting strong enough to lift the Ti $3d$ $t_{2g}$ orbital degeneracy. Another theoretical study, however finds a much smaller CF splitting, leaving still open the possibility for an orbital liquid state [28]. The experimental determination of the magnitude of the CF splitting is difficult. Using soft-x-ray absorption spectroscopy at the Ti $L_{2,3}$ edges as a local probe, Haverkort et al. [29] estimated that the CF splitting should be of order $0.12 - 0.30\,eV$. This value is large enough to prevent the formation of an orbital liquid. It is also large enough to strongly reduce the orbital moment from its ionic value, as found by the neutron

study by Keimer et al. [24] and also by the spin-resolved photoelectron spectroscopic experiment with circularly polarized light by Haverkort et al. [29]. Nevertheless, the intriguing question remains whether one could find ways to modify $LaTiO_3$, for instance by doping or substitution, in order to minimize the influence of crystal fields and to generate orbital fluctuations. In this respect it is interesting to note that the $T_N$ of the sample used in the neutron study [24] is less than optimal, opening the possibility that the sample is slightly off-stoichiometric and therefore, perhaps also slightly metallic. Would this cause sufficient charge fluctuations and, along with them, also orbital fluctuations? This issue is intimately connected to another aspect for which the titanates turned out to be an ideal model system for the study of the electronic structure of strongly correlated system, as described next.

One of the long standing topics in theoretical solid state physics concerns the single-particle spectral weight distribution in Mott-Hubbard systems in the vicinity of the metal-insulator transition [2, 30]. The class of $d^1$ perovskites has been recognized in the last decade as a materialization of this topic on which experimental tests can be carried out [31–37]. The comparative photoemission (PES) study on the band-width-controlled $Ca_{1-x}Sr_xVO_3$ material by Inoue *et al.* [34] yields striking systematic changes which triggered strong interest from the correlated electron community.

Also in the titanates one could observe very interesting features: upon doping, e.g. $La_{1-x}Sr_xTiO_3$, $T_N$ is quickly suppressed and new states are created in the vicinity of the chemical potential as seen by PES [31–37]. Somewhat surprising is that the doped system has an appreciable sharp Fermi cut-off, very much unlike magnetite in the metallic phase [38,39]. This seems to indicate that polaronic effects do not play a major role, making the system ideal to study the basics of the evolution of spectral weight in doped magnetic insulators without extra complications. Important is that the PES studies have found very heavy masses for the charge carriers in those doped titanates.

Nevertheless, the above mentioned photoemission results seem to be not consistent with data obtained from transport or thermodynamic measurements. Also the photoemission spectra of the undoped $LaTiO_3$ and $YTiO_3$ system cannot be reproduced by the various theoretical models presently available. There are now indications that those observations could be plagued by the surface sensitivity of the type of photoemission used in

those studies. It is being realized only in recent years, that the electronic structure of the surface of a material could be quite different from that of the bulk, especially for strongly correlated systems, in which the on-site and nearest neighbor interactions play the most relevant role. This is true not only for rare-earth intermetallics [40–44], but also for oxides. More recent PES studies using high photon energies to be more bulk sensitive [45,46], reveal that for the $Ca_{1-x}Sr_xVO_3$ system, the changes between bulk $CaVO_3$ and $SrVO_3$ are too small to be detected. Also studies based on the dynamical mean field theories (DMFT) [47–50] indicate that the differences in band width are too small to have a noticeable impact on the spectra [27, 45, 51]. The objective of this thesis is to study the electronic structure of the titanates as valuable model compound for a $d^1$ system, with emphasis on the evolution of the spectral weight as function of band width and doping. In view of the existing discussions in the literature, it is crucial to use better defined samples: we have to grow titanate single crystals with well defined stoichiometry and with well characterized magnetic and transport properties. Another essential aspect of the work is to use photoelectron spectroscopy techniques which can deliver spectra which are truly representative for the bulk material. Only in this manner we can do a critical and quantitative evaluation of the various advanced many-body models currently available trying to describe the excitation spectra of strongly correlated systems.

The lay-out of the thesis is as follows:

We will start in chapter 2 with a description of the basic physical properties of the titanates. A detailed description of the growth and characterization of the samples will be given in chapter 3. Issues concerning photoelectron spectroscopy as a technique to measure the electronic structure will be explained in chapter 4. The results, including comparison with various theories, will be presented in chapter 5, followed by summary and acknowledgements.

# Chapter 2

# Titanates: Basic Properties

In this chapter we will describe several key physical properties of the $RE$TiO$_3$ system. These include the crystal structure, electrical and magnetic properties, as well as the basic electronic structure including crystal fields.

## 2.1 Crystal Structure

Like many chemical compounds with a AMX$_3$ composition the $RE$TiO$_3$ crystallizes in the well known perovskite structure, which is shown in figure 2.1. Here the oxygen- together with the rare earth ions build a cubic closed package structure. The smaller Ti- ions are located in every fourth octahedral voids. These octahedra are connected with its six neighbors through corner sharing [53]. From this geometrical view ideal ratios of the ionic radii can be derived [53] for the structure to be cubic. The oxygen and rare earth ions should have the same size:

$$r_A = r_O, \tag{2.1}$$

while the titanium ion must fit in the octahedral void and therefore must have as radius $r_{Ti}$:

$$r_{Ti} = \left( \sqrt{2} - 1 \right) r_O = 0.414 \, r_O. \tag{2.2}$$

Deviations from this ratios can be treated by the tolerance factor of Goldschmidt [54]:
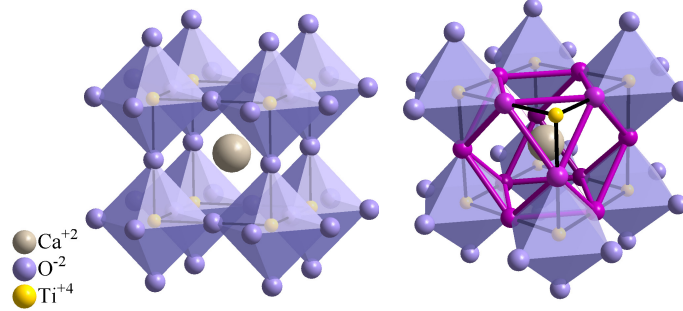
**Figure 2.1:** The cubic perovskite structure. In the left picture is the focus on the network of corner shared octahedra and in the right on the cubic closed ball package of the oxygen and Ca ions in the perovskite structure. to illustrate the ccp structure the 12 neighbor atoms of the Ca ion colored purple from [52].

$$t = \frac{r_{RE} + r_O}{\sqrt{2}\,(r_{Ti} + r_O)}. \tag{2.3}$$

For $t < 0.96$ the octahedra become tilted against each other, what leads to the $GdFeO_3$ structure which is shown in figure 2.2 with the corresponding space group Pbnm [55,56]. This is the structure of the $RETiO_3$ compounds.

In the observed rare earth series the radius of the trivalent ions gets smaller with its atomic number and is smallest for the $Gd^{3+}$ and $Y^{3+}$ ions. This is connected with an increasing tilt of the Ti-O-Ti bond angle $\theta$. For the compound with the largest rare earth ion, namely $LaTiO_3$, the bond angle is $\theta \approx 155°$ while for the $YTiO_3$ the bond angle is reduced to an value of $\approx 142°$ [18–20, 57].

## 2.2   Magnetic Properties

The $RETiO_3$ materials order magnetically. $LaTiO_3$, for example, is a G-type antiferromagnet with a Néel temperature which varies between $T_N =$ 130 and 146 K, depending on the exact oxygen stoichiometry [18, 20–22]. $YTiO_3$ on the other hand, is a ferromagnet with a Curie temperature of about $T_C = 29$ K [18, 58].
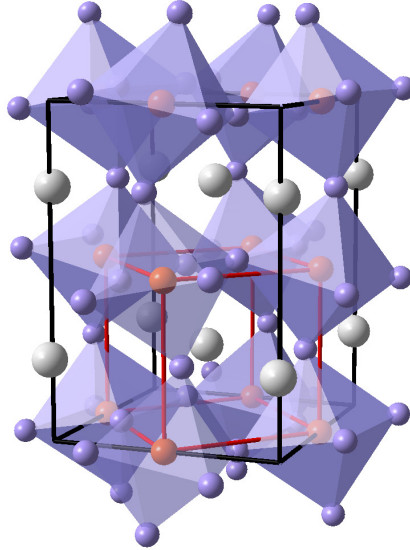
**Figure 2.2:** $GdFeO_3$ unit cell; the orange cube in the middle shows the unit cell of the cubic perovskite.

Figure 2.3 shows the magnetic phase diagram of $RETiO_3$ as a function of the rare-earth ionic radius [57]. One can clearly see that the crossover between ferromagnetic and antiferromagnetic order is linked to the size of the rare-earth ion. This in turn, as we will see later, determines the crystal field levels and consequently the orbital occupations governing the sign and magnitude of the superexchange interactions via the Goodenough-Kanamori-Anderson rules [62–64].

## 2.3 Electrical Transport Properties

Temperature dependent resistivity measurements on the $La_{1-x}Sr_xTiO_{3+\delta}$ and $Y_{1-x}Ca_xTiO_3$ series show that the parent $LaTiO_3$ and $YTiO_3$ compounds are essentially insulators [60, 65]. It is only upon doping with Sr, Ca or excess of oxygen that the material acquire a metallic-like behavior as indicated by the positive resistivity-temperature slopes as displayed in figure 2.4. Here one must note that the oxygen content in the La(Sr)-titanates is a parameter which is difficult to control, and yet very important for the
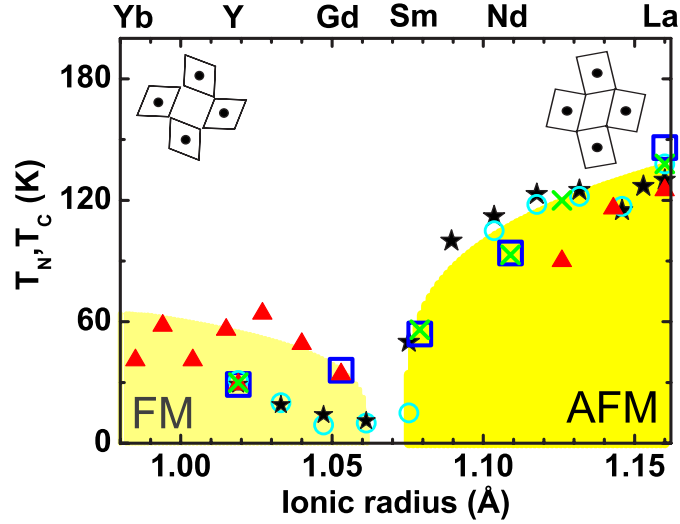
**Figure 2.3:** Magnetic phase diagram for $RETiO_3$ and $La_{1-x}Y_xTiO_3$ taken from [57]. $T_c$ and $T_N$ are plotted as a function of the rare-earth ionic radius. Squares: $T_c$ and $T_N$ for $RETiO_3$ from this work. Triangles: values for $RETiO_3$ from Greedan [59]. Crosses: values for $RETiO_3$ from Katsufuji *et al.* [60] Circles: values for $La_{1-x}Y_xTiO_3$ from Okimoto *et al.* [35]. Stars: values for $La_{1-x}Y_xTiO_3$ from Goral *et al.* [61]. The inset shows the principal octahedra of the end members.

properties of the material. Not only has a slight oxygen off-stoichiometry a strong reduction effect on the Néel temperature of $LaTiO_3$ [18, 20–22], but it also drives the material quickly away from its insulating character. This is demonstrated in figure 2.5, where one can observe that $\delta$=0.01 is already sufficient to make $LaTiO_{3+\delta}$ to have a temperature independent resistivity curve. One really needs to have $\delta$ values much smaller than 0.01 to find a clear insulating behavior.
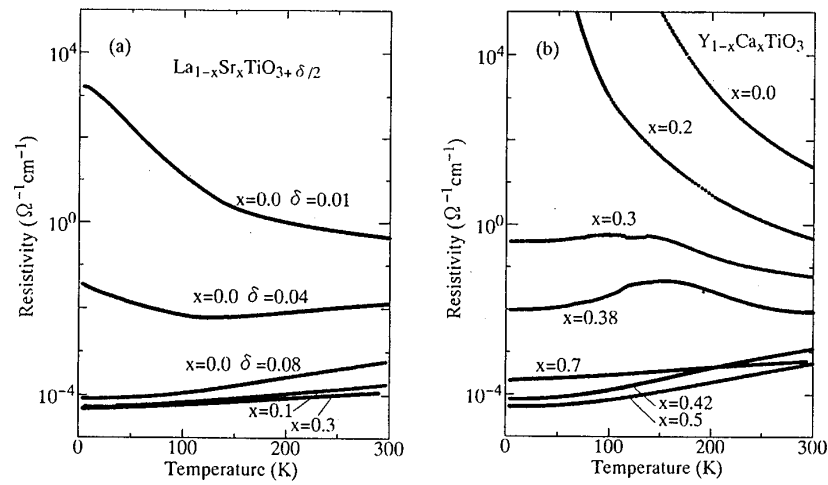
**Figure 2.4:** Temperature dependence of the resistivity for $LaTiO_{3+\delta}$ or $La_{1-x}Sr_xTiO_3$ and for $Y_{1-x}Ca_xTiO_3$ from [60,65].



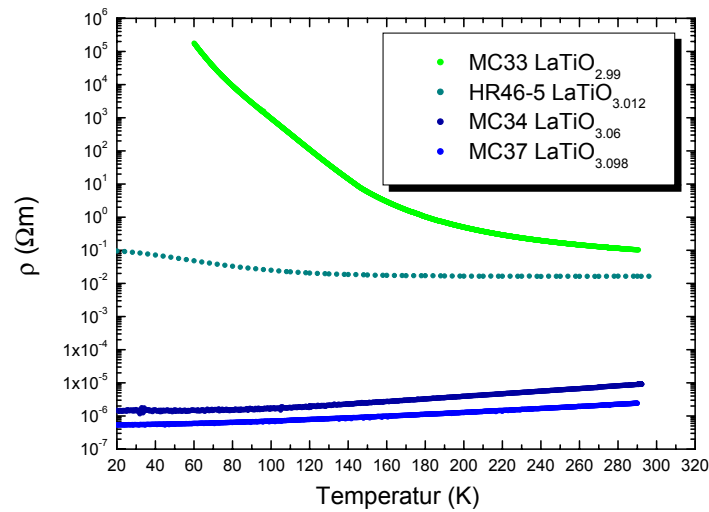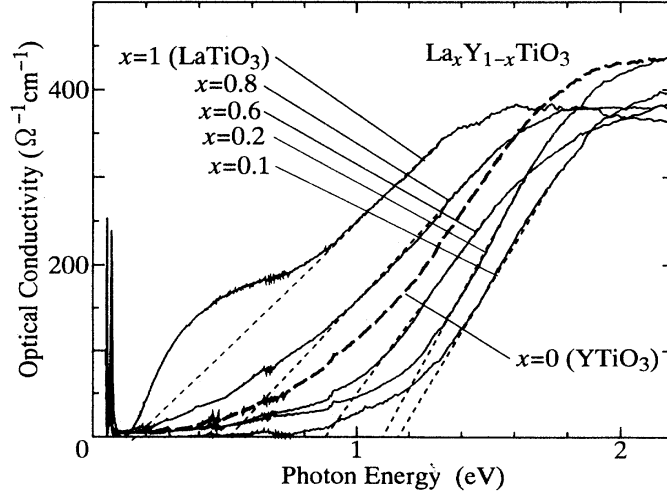**Figure 2.5:** Resistivity of the Sr-doped $LaTiO_3$ system [52].

**Figure 2.6:** Spectra of optical conductivity in $La_{1-x}Y_xTiO_3$ at room temperature. A crossing point of a baseline and a dashed line is defined as the Mott-Hubbard gap energy. Taken from [35].

## 2.4   Band Gaps

With the resistivity experiments indicating the insulating nature of the un-doped or parent titanates, e.g. $LaTiO_3$ and $YTiO_3$, it is then natural to raise the question about the size of the conductivity gap. This is important for the understanding and modelling of the electronic structure of the material as we will see later. Figure 2.6 show the optical conductivity of $La_xY_{1-x}TiO_3$ measured by Okimoto *et al.* [35]. For the pure $YTiO_3$ ($x$=0), one can clearly see that the onset of strong absorption is located at about $0.6\,eV$ photon energy. This can be identified as the band gap value. For $LaTiO_3$ ($x$=1) however, the situation is somewhat unclear. One does not observe a smooth onset but rather a bump centered at about $0.3\,eV$. The origin of this bump is not clear, and it has been speculated that this is caused by slight oxygen off-stoichiometry. Nevertheless, if one is willing to make an extrapolation from the range between 0.8 and $1.4\,eV$, then a value of about $0.2\,eV$ can be found for which the optical conductivity vanishes. More recent optical data are provided by Rückamp *et al.*, see Figure 2.7. Also here one can deduce a band gap value of $0.6\,eV$ for $YTiO_3$ by taking
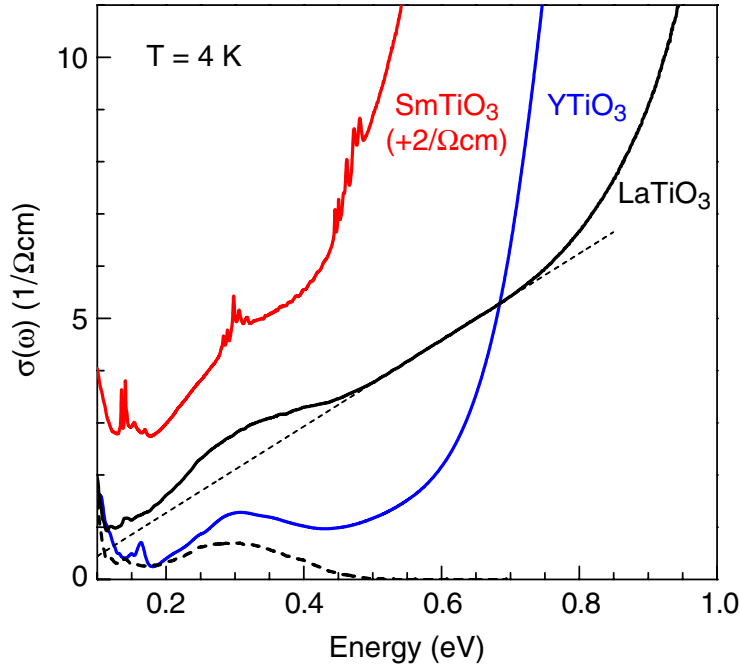
**Figure 2.7:** Optical conductivity of (twinned) single crystals of $LaTiO_3$, $SmTiO_3$ and $YTiO_3$ at T = 4 K. An offset of $2\,\Omega^{-1}$ $cm^{-1}$ has been added to the data of $SmTiO_3$ for clarity. Phonon-activated orbital excitations are observed at $0.3\,eV$ in all three compounds. For $LaTiO_3$, an estimate of the orbital excitation band has been obtained by subtracting a linear background (- - - -). The additional sharp features in $SmTiO_3$ at 0.15, 0.3 and $0.45\,eV$ are due to crystal-field transitions within the $Sm\,4f$ shell [111], taken from [66].

the onset of strong absorption. The $LaTiO_3$ spectrum shows surprisingly also a bump at about $0.3\,eV$, similar to the Okimoto data, although here great efforts were made to secure the stoichiometry of the sample. This lead Rückamp *et al.* to conclude that the $0.3\,eV$ gap originates from $d - d$ excitations associated with the crystal field splitting of the Ti $3d$ orbitals [66]. Yet, it is not clear from this spectrum what the band gap of $LaTiO_3$ should be.

## 2.5   Band Structure

Electronic structure calculations are indispensable for a better understanding of the physical properties and correct interpretation of the experimental data. This is especially true for transition metal oxides in which the correlated motion of the electrons more than often is cause for unexpected entanglement of competing interactions. We will use the *ab-initio* density functional theory (DFT) within the local density approximation (LDA) as a first step to obtain a general orientation on the relationship between crystal structure, chemical composition and basic electronic structure features such as the one-electron band widths and crystal fields.

Various groups have calculated the band structure of the $RE\mathrm{TiO}_3$ system with very consistent results [27,31–33,37,67–69]. The basic features are shown for $\mathrm{LaTiO}_3$ and $\mathrm{YTiO}_3$ in figures 2.8 and 2.9 as reproduced from the work by Pavarini *et al.* [71]. The O $2p$ derived bands are located between -3 eV and -8 eV energy indicating that the O $2p$ bands are essentially full, i.e. complying with the $\mathrm{O}^{2-}$ formal valence. The Ti $3d$ bands can be found between -1 eV and +6 eV energy, whereby the lower lying parts (i.e. between -1 eV and +1 eV) are built up from the $t_{2g}$ orbitals and the higher lying parts from the $e_g$ orbitals. The La $5d$ and Y $4d$ like bands are positioned above the Fermi level, reflecting their trivalent ionic states.

In comparing the band structures calculated for the hypothetical ideal cubic structure and for the real structures, one notices immediately that the bands become narrower. This is not only true for the O $2p$ bands, but also for the Ti $3d$, whereby the band narrowing even results in an opening of a gap between the $t_{2g}$ and $e_g$ bands. Important also is to notice that the bands of the $\mathrm{YTiO}_3$ are narrower than those of the $\mathrm{LaTiO}_3$, consistent with the larger distortions and tilts of the $\mathrm{TiO}_6$ octahedra in the Y system.

The most striking result of the LDA calculations is that Ti $3d$-$t_{2g}$ bands straddle through the Fermi level giving the prediction that $\mathrm{LaTiO}_3$ and $\mathrm{YTiO}_3$ are metallic. This is clearly a failure. The insulating nature of the materials as found from resistivity measurements is not explained by the calculations. The sizable 0.6 eV band gap as observed clearly by optical spectroscopy for $\mathrm{YTiO}_3$ is not at all reproduced. The implications of this failure are far reaching. It can be taken as a direct evidence for the strongly correlated motion of the electrons in these materials, calling for a quite different approach for the description for their electronic structure.
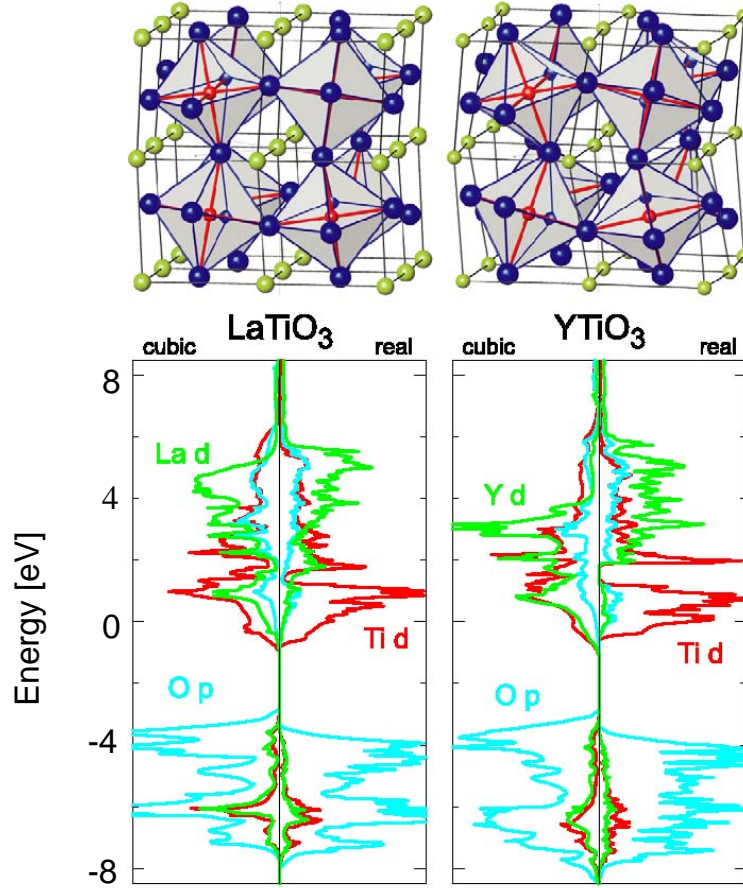
**Figure 2.8:** Crystal structures and electronic bandstructures for the $3d(e_g)$ orthorhombic perovskites $LaTiO_3$ and $YTiO_3$: A (green), B (red) and O (blue). The bottom part shows densities of one-electron states (DOSs) calculated in the LDA for the real structures (right-hand panels) and for hypothetical, cubic structures with the same volumes (left-hand panels). The green, red, and blue DOSs are projected onto, respectively, $(La, Y)$ $d$, $Ti 3d$, and O $2p$ orthonormal orbitals [70]. The $Ti 3d(t_{2g})$ bands are positioned around the Fermi level (zero of energy) and their widths, W, decrease from $\sim 3$ to $\sim 2$ eV along the series. The much wider $Ti 3d(e_g)$ bands are at higher energies. This figure resulted from linear muffin-tin orbitals (LMTO) calculations in which the energies, $\epsilon_{\nu Rl}$, of the linear, partial-wave expansions were chosen at the centers of gravity of the occupied, partial DOS. Since those energies are in the O $2p$ band, the LMTO errors proportional to $(\varepsilon - \epsilon_{\nu Rl})^4$ slightly distort the unoccupied parts of the DOS.
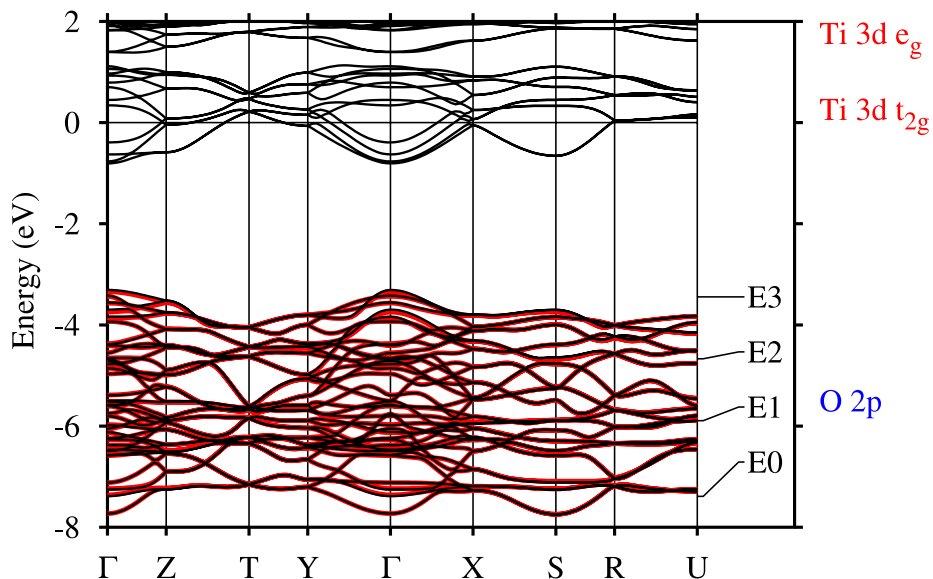
**Figure 2.9:** LDA bandstructure of orthorhombic $LaTiO_3$. The bands obtained with the truly minimal (downfolded) O $2p$ NMTO basis (red) are indistinguishable from those obtained with the full NMTO basis (black), from [71].

## 2.6 Hubbard Model

The failure of the band structure calculations to describe the insulating state of the titanates can be traced back to the neglect of the strong on-site Coulomb interaction in the Ti $3d$ shell. In conventional band-structure theory, every electron is presumed to move independently through a periodic potential dictated by the positive ion cores that make up the lattice, and the collective potential of all the other electrons together in a mean-field manner. These effectively single-particle theories work actually surprisingly well to describe large classes of solids, mostly wide band materials like semiconductors and many common metals. But for transition metal oxides, including the titanates, the electron-electron repulsion at the transition metal sites are so strong that their effect have to be taken into account in an explicit manner.
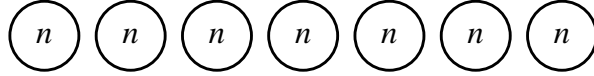
To illustrate the basic features of a strongly correlated system, let us consider the case of the so–called Hubbard model. This model consists of $f$-fold degenerate orbitals at each atomic site and electrons can hop from site to nearest-neighbor site with transfer integral $t$. In the absence of electron-electron interactions, this will result in a total band width $W = Zt$ where $Z$ is a parameter proportional to the coordination number, and $W$ is then called the one-electron band width. Electron-electron interactions can then be introduced in the form of a Coulomb repulsion between pairs of electrons on one atom, and is indicated by the quantity $U$, often also called the Hubbard $U$. The pair interaction $U$ can be shown to be equivalent to the energy it costs to move an electron from one part of the system to another, over a large distance.

Consider the following ground-state system in the tight-binding limit, consisting of $M$ sites, in which every site has $n$ electrons, for a total of $N$ electrons in the whole system: For the moment we leave out the electron spin and consider each site as consisting of a single infinitely-degenerate orbital. Moving an electron from one site to another site far away means creating a non-local electron-hole pair.

The total Coulomb energy in the initial state is $M{\cdot}\frac{1}{2}n(n{-}1)U$, while in the final state it is $(M{-}2){\cdot}\frac{1}{2}n(n{-}1)U + \frac{1}{2}(n{-}1)(n{-}2)U + \frac{1}{2}(n{+}1)nU$. It is easy to work out that, whatever the ground-state occupation $n$ is, the difference between the initial and final state, and thus the creation energy of a far-apart electron-hole pair, is always equal to $U$.

To determine the magnitude of $U$, one could carry out an photo- conductivity absorption experiment. In the limit of zero band width ($W{=}0$), the measured band gap will give the $U$ value. The process of creating such a far-apart electron-hole pair can also be split up into two independent actions, namely removing an electron (which costs the ionization energy $E_I$),
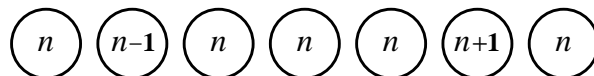
and adding an electron somewhere else (which gains the electron affinity $E_A$). The pair interaction $U$ is then equivalent to the difference $E_I$ - $E_A$. These two processes, which create, respectively, an $N$-1 and an $N$+1 electron system, are commonly called photoemission and inverse photoemission processes.

Whether the system is a metal or an insulator depends on the relative magnitude of $U$ and the bandwidth $W$. Consider an electron-hole excitation as described above. This excitation costs an energy $U$, but after this the electron and the hole it left behind are free to propagate through the lattice basically in a one-electron manner, because the total potential of the $n$-occupied sites they encounter is again periodic. An energy $W$ (the one-electron bandwidth) is thus gained. If this gain is large enough, the system is likely to be a metal. The presence of the two energy scales $U$ and $W$ suggests that the quantity that governs the metallicity of the material is their ratio. For $U > W$, it is energetically not favorable for an electron to move, and the system will become a so-called Mott-Hubbard insulator. The point at which the metal-to-insulator cross over occurs is usually called the Mott transition.

Very useful diagrams for understanding correlated electron systems are obtained by plotting the photoemission and inverse photoemission spectra on a common energy scale, with their zero-energy points coinciding. The chemical potential $\mu$ is then by definition situated at the meeting-point, as it is the point at which the costs of both adding or removing an electron are zero. In the case that there is actually a non-zero spectral weight at the chemical potential, the system can be called a metal, and we can define the Fermi level $E_F$ as being equivalent to the chemical potential.

The top panel of figure 2.10 shows the photoemission and inverse photoemission spectrum for a half filled Hubbard model in the limit $U = 0$. This spectrum yields a band with a width given by the one-electron band width $W$, since here we are back at the single particle picture, and the spectrum is identical to the occupied and unoccupied density of states of the system. The bottom panel of figure 2.10 displays the case where $U \gg W$. Here a band gap is opened, and the peak-to-peak distance of the photoemission and inverse photoemission spectra is given by $U$. The magnitude of the band gap of this Mott-insulator depends on the value of $W$. The photoemission part is often called the lower Hubbard band (LHB) and the inverse photoemission part the upper Hubbard band (UHB). Note that, al-
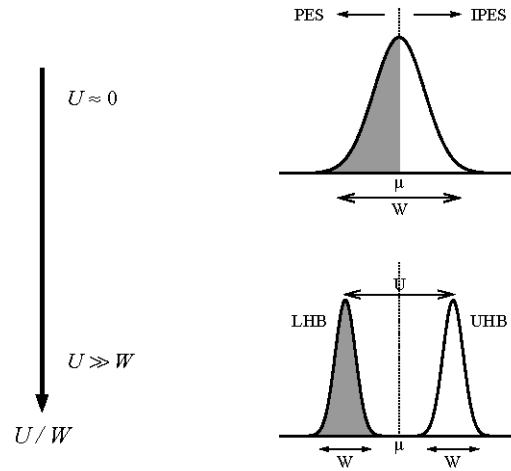
**Figure 2.10:** Photoemission and inverse photoemission spectra as expected in a Hubbard model for different values of U/W. The grey shading indicates occupied states. Adapted from Morikawa *et al.* [37].

though the picture looks similar to that of the density of states of a band insulator in one-electron theory, it describes a completely different system. The UHB and LHB on either side of the chemical potential represent one and the same partially-filled band, respectively in the N +1 and the N -1 electron systems. The N electron system does not enter in this picture at all, and neither do electron-number-conserving (e.g., optical) excitations. It is also incorrect to call the UHB to be the occupied Hubbard band and the LHB the unoccupied Hubbard band, since the terms occupied and unoccupied refer to the language used within the frame work of the one-particle theory, which is no longer valid here.

## 2.7 Crystal Field Splitting

Having established that the undoped titanates are Mott insulators, we now have to reconsider the energy scale of the fluctuations relevant for the properties of these materials. This will no longer be given by the one-electron

band width of the Ti $3d$ band (of order $5\,\mathrm{eV}$), nor of the Ti $3d$-$t_{2g}$ sub-band (of order $2\,\mathrm{eV}$). Instead it will determined by virtual processes in which one electron hops to a neighboring site and back, giving an energy gain of $t^2/U$, which is of order $100\,\mathrm{meV}$ only or even less. This in turn means that we have to look more carefully at the energetics of the Ti $3d$ orbitals, since energy splittings of order $100\,\mathrm{meV}$, caused by crystal fields, can then already destroy the degeneracy of the $t_{2g}$ orbitals, with consequences for the magnitude of the orbital moment, isotropy or anisotropy of the spin wave spectrum [24], and the stability of the proposed orbital liquid state [24, 25].

As mentioned above, the Ti ions in the $\mathrm{RETiO_3}$ series are surrounded by six oxygen ions in octahedral geometry. This cubic crystal field leads to a level splitting of the $d$ levels of $10\,\mathrm{Dq} \approx 2\,\mathrm{eV}$ between the $t_{2g}$ ($d_{xy}$, $d_{yz}$, $d_{zx}$) and the $e_g$ levels ($d_{z^2}$ and $d_{x^2-y^2}$). The two $e_g$ levels involve orbitals with lobes facing the oxygen ions, thus they are raised in energy because of the stronger electrostatic repulsion [72, 73], see figure 2.11.
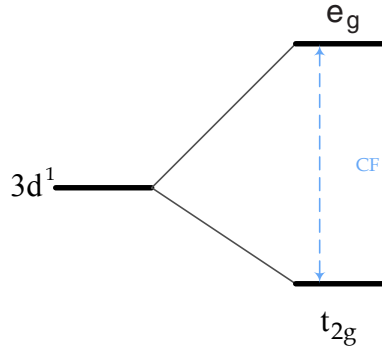


**Figure 2.11:** Crystal field splitting in an octahedral surrounding.

Through the tilting and rotation of the octahedra in the $\mathrm{GdFeO_3}$ structure the surrounding of the Ti ions exhibit a deviation from cubic symmetry caused by the crystal field of the $\mathrm{RE^{3+}}$ ions. Here the distances between the ions along the $\pm(111)$ direction are shortened. This is leading to a nearly trigonal crystal field with the (111) axes as trigonal axes. Thus the degeneracy of the $t_{2g}$ orbitals is lifted due to the attractive Coulomb potential between the $\mathrm{R^{3+}}$ ions and the $t_{2g}$ levels. The lowest level at each site is specified as a linear combination of the $|xy\rangle, |yz\rangle, |zx\rangle$ wave functions:

$$
\begin{array}{ll}
\text{site 1:} & a|xy\rangle + c|yz\rangle + b|zx\rangle \\
\text{site 2:} & a|xy\rangle + b|yz\rangle + c|zx\rangle \\
\text{site 3:} & a|xy\rangle - c|yz\rangle - b|zx\rangle \\
\text{site 4:} & a|xy\rangle - b|yz\rangle - c|zx\rangle
\end{array} \tag{2.4}
$$

with $a^2 + b^2 + c^2 = 1$. For $LaTiO_3$, using a point charge model and their recent crystal structure data, Cwik *et al.* found $a$=0.636, $b$=0.544, and $c$=0.544 [20]. Using also the point charge model, Mochizuki and Imada obtained $a$=0.60, $b$=0.39 and $c$=0.69 [74]. LDA+DMFT calculations by Pavarini *et al.* produced $a$=0.599, $b$=0.32 and $c$=0.735 [71]. The latter two groups thus found very similar and consistent results.

Interestingly, with increasing tilt angle the parameter b is reduced systematically as shown in figure 2.12 from the Mochizuki and Imada study [74].
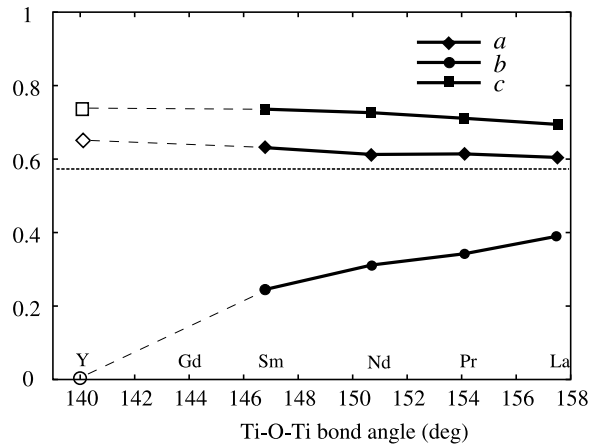


**Figure 2.12:** Systematical change of the orbital ground state in the $RETiO_3$ series. With increasing bond angle the parameter b in equation 2.4 is enhanced, too.

For the ferromagnetic $YTiO_3$ with its very large tilt angle, the orbital ground state can be even approximated as a linear combination of:

$$
\begin{array}{ll}
\text{site 1:} & a|xy\rangle \pm c|yz\rangle \\
\text{site 2:} & a|xy\rangle \pm c|zx\rangle \\
\text{site 3:} & a|xy\rangle \mp c|yz\rangle \\
\text{site 4:} & a|xy\rangle \mp c|zx\rangle
\end{array}
\tag{2.5}
$$

with $a=\sqrt{0.4}=0.63$ and $c=\sqrt{0.6}=077$ [74,75]. The LDA+DMFT calculations by Pavarini *at el.* yielded $a=0.620$, $b=-0.073$, $c=0.781$. This point charge model and the LDA+DMFT results are in good agreement.

With regard to the crystal field splittings, Cwik *et al.* [20] arrived at an estimate of about $0.24\,\text{eV}$ for $LaTiO_3$ from their point charge model: the lower $t_{2g}$ level is non-degenerate while the upper is doubly degenerate. Pavarini *et al.* [27] found $0.19\,\text{eV}$ and $0.21\,\text{eV}$ splitting. Experimentally, Rückamp *et al.* [66] attributed the bump at $0.3\,\text{eV}$ in their optical conductivity spectra for $LaTiO_3$ to forbidden $d-d$ excitations involving these crystal field split $t_{2g}$ orbitals. Using soft-x-ray absorption spectroscopy at the Ti $L_{2,3}$ edges as a local probe, Haverkort et al. [29] estimated that the CF splitting should be of order $0.12$ - $0.30\,\text{eV}$. All these estimates point to the conclusion that the crystal field splitting in $LaTiO_3$ is strong enough to lift the Ti $3d$ $t_{2g}$ orbital degeneracy as to prevent the formation of an orbital liquid state. It is also large enough to strongly reduce the orbital moment from its ionic value, consistent with the neutron study by Keimer et al. [24] and with the spin-resolved photoelectron spectroscopic experiment with circularly polarized light by Haverkort et al. [29]. Finally, the crystal field splitting for $YTiO_3$ is estimated to be $0.20$ and $0.33\,\text{eV}$ from the LDA+DMFT study. These values are larger than for $LaTiO_3$, consistent with the larger distortions and tilts in the Y system.

# Chapter 3

# Crystal Growth

## 3.1  Zone Melting

The zone melting technique is a recrystallization technique which was originally developed for purification. Now it is also established as a standard method for growing single crystals for intermetallic and transition metal oxide compounds. A sketch of the zone melting technique is shown in picture 3.1. At the beginning a bar of polycrystalline material is molten at one side
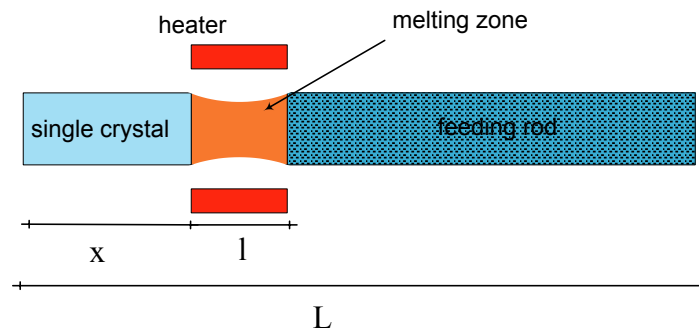


**Figure 3.1:** Zone melting technique. A heater melts one part of a bar. Then the heater is driven along the whole bar, thus the whole feeding bar melts and recrystallizes partially.

and connected with the seed to generate the melting zone. Then the melting zone is moved through the whole feeding rod by driving the heater system in

one direction (or the bar in the other). In the optimal case will the feeding rod recrystallize as a single crystal [76, 77].

One advantage of the floating zone technique over methods where the crystallization happens via the gas phase like chemical transport is the speed of crystal growth. For example the growing rate of $VO_2$ crystals obtained by chemical transport is only $\approx 3\,mg/h$ [78], while in this thesis these crystals could be pulled through floating zone with a speed of $10\,mm/h$, what means a growing rate of $\approx 1000\,mg/h$. Furthermore the crystals grown by chemical transport often reach only a size of a view millimeters, which sometimes limits the physical experiments possible for these crystals. A typical size, however, of crystals grown by floating zone is a few centimeters, what is satisfactory for the most experiments.

In principle with other methods, where the growth happens not via gas phase, crystals can be grown with grow rates and sizes comparable to the floating zone technique. Even the size of crystals which were grown by the Choralsky method can reach more than one meter. But in this technique the whole feeding material must kept molten during the whole growth, therefore a crucible is needed. In contrast the floating zone technique can be done crucible free, because only a small part of the feeding material is molten, namely the melting zone, which can be stabilized by the surface tension only. So the serious problem of contamination with crucible material at very high temperatures ($\approx 1900\,°C$) is eluded.

## 3.2 Floating Zone Furnace

The floating zone furnace which is used for all the crystal growths in this thesis is the model FZ-T-10000-H-VI-VP from the company *Crystal Systems INC* and is shown in picture 3.2. Its heart is the heating system consisting of four aluminium metalized Pyrex glass mirrors. With these mirrors the light of four halogen lamps is focused into the center of the floating zone furnace to heat the melting zone as shown in picture 3.3. To accommodate for different melting points it is possible to equip the furnace with various sets of lamps. With the most powerful lamps of $4 \times 1500\,W$ a maximum temperature of $\approx 2100\,°C$ can be reached [52]. The regulation of the power of the lamps and therefore the temperature happens via an Eurotherm controller in $0.1\,\%$ steps of the maximum current.

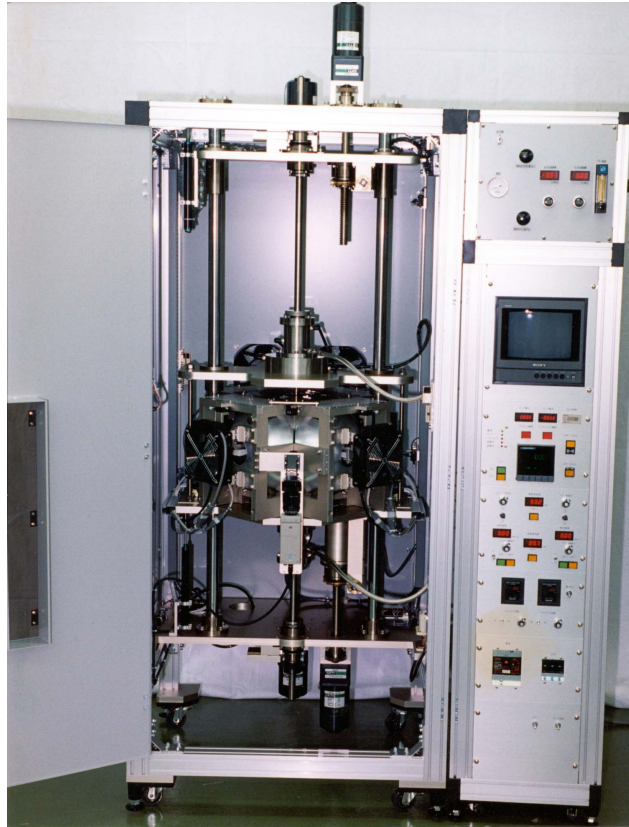Both the mirror stage and the upper shaft can be driven separately

**Figure 3.2:** The floating zone furnace *FZ-T-10000-H-VI-VP*.

within a speed range from $0 - 27.15\,\mathrm{mm/h}$ by stepper motors. The velocity of the mirror stage is equal to the growing speed [80], while with the speed of the upper shaft the thickness of the melting zone and the pulled crystal can be controlled. In general in this thesis the upper shaft was only moved to stabilize the melting zone by means of varying the amount of feeding material. Additionally both shafts can also be rotated around the growing axis up to 60 r/min to stir the melt.

The preparation chamber is consisting of a quartz glass tube which can be locked gas tight, hence it is possible to use different atmospheres for the growth up to a pressure of $10\,\mathrm{bar}$, especially $\mathrm{Ar}$, $\mathrm{N_2}$ and $\mathrm{O_2}$. To observe the melting zone during the growth the furnace is equipped with a CCD camera.
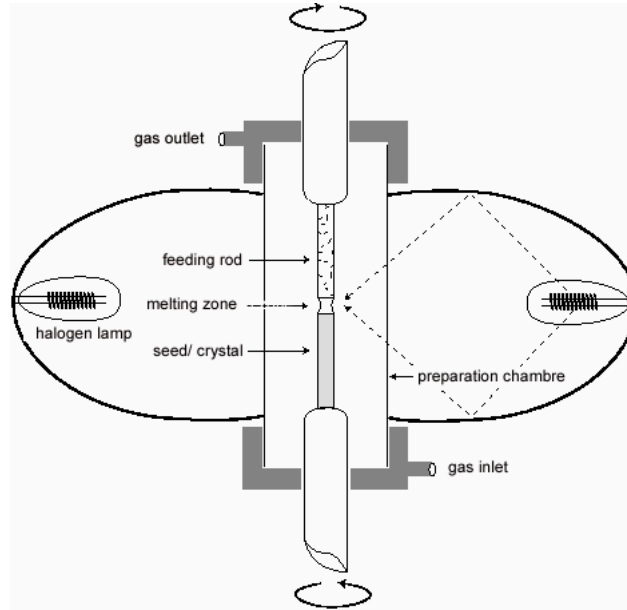
**Figure 3.3:** Sketch of the preparation chamber and heating system of the floating zone furnace, taken from [79].

## 3.3 Stability of the Melting Zone

### 3.3.1 Zone Length

When using the floating zone technique crucible free, only the surface tension $\sigma$ of the melt prevents the melting zone from dropping down. The maximum length $l$ of a stable melting zone is determined by:

$$l = 2.84\sqrt{\frac{\sigma}{\varrho g}}, \tag{3.1}$$

where $\varrho$ is the density of the material and $g$ the acceleration of earth gravity [81–83]. In practice especially turbulences can reduce this theoretical value $l$.

### 3.3.2 Stirring and Heat Profile

When growing crystals from the melt stirring has two main functions, namely to balance material and temperature inhomogeneities. While for the Choral-

sky technique the material aspect is more important because the volume of the melt can reach sometimes more than $0.1\,\mathrm{m}^3$, it is less relevant in the floating zone technique [83]. Here the amount of molten material is only $\approx 0.1\,\mathrm{cm}^3$, so an inhomogeneous material distribution will be balanced quite well by thermal fluctuations.

In the floating zone technique (with a mirror furnace) the melt is stirred primarily to compensate a thermal gradient. Due to the optical heating system, the horizontal temperature profile is strongly inhomogeneous, because only the part of the melting zone, which is facing to a mirror is heated up. In figure 3.4 the temperature profile of a two mirror furnace is shown. At high temperatures ($T > 1500\,^\circ$C) the temperature differences $\Delta T$ in the
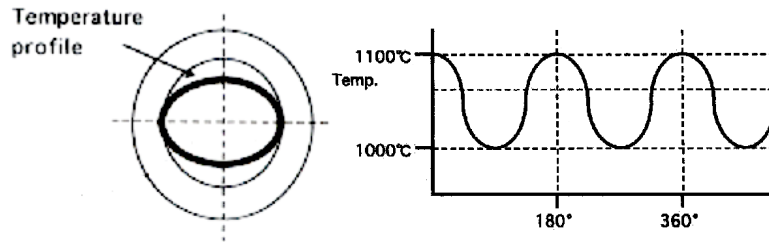


**Figure 3.4:** Temperature profile of a two mirror floating zone furnace taken from [80]. Due to the focusing mirrors the melting zone is heated up only at two points what leads to a tremendous horizontal temperature gradient.

horizontal plane between the hottest and coldest part of the melting zone are typically more than $150\,^\circ$C, much larger than acceptable for single crystal growth [80].

It is easy to understand that a four mirror furnace, which was used here, has a more homogeneous temperature distribution in the horizontal plane. For the used four mirror furnace the temperature profile is shown in figure 3.5. The constructer company reports [80] that in comparison with a two mirror furnace the temperature difference in the horizontal plan is strongly reduced to

$$\Delta T < 10\,^\circ\text{C}. \tag{3.2}$$

This advantage was used especially for the growth of the $\mathrm{RETiO_3}$[1] crystals.

While in the growth of $\mathrm{Y\,TiO_3}$ single crystals controlling of the melting zone is very easy, for the $\mathrm{RETiO_3}$ growth the maximum length $l_{max}$ of a

---

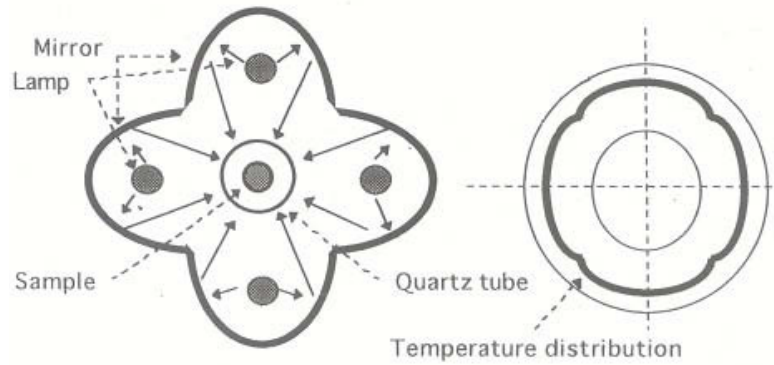[1]$\mathrm{RE} = \mathrm{Nd}$, Sm and Gd

**Figure 3.5:** The used floating zone furnace exhibits a very homogeneous temperature profile because of the four mirror design [80].

stable melting zone is strongly reduced, which could be caused by the higher specific mass (see equation 3.1).

But in practice when turning the feed and the seed the zone length can't be reduced under an certain threshold, because the feed and the seed must be separated quite well. Otherwise they trundle around each other, what disconnects the melting zone immediately. So with stirring, a further reduction of the zone length to stabilize the melting zone was not possible.

But due to the homogeneous temperature distribution through the four mirror design, crystal growth without stirring was possible and therefore the trundling problem could be avoided. Thus it was possible to keep the melting zone short enough to be stable in the growth of the $RETiO_3$ crystals (see chapters 3.9 – 3.11).

### 3.3.3 Growth Rate

As known from [52] in the growth of Titanates evaporation effects occur which are changing the material composition. To keep this effect small, the idea was to hold the material only a short time at high temperatures, that means in the melting zone. Therefore the growth rate should be much higher than for typical crystal growths like Co- or Cu-oxide compounds, which were typically grown with a speed of $\approx 2\,mm/h$ [79, 84–86]. On the other hand the growth rate should be not to high, because when the speed of crystal pulling exceeds an upper limit, the crystals grow no longer as (twinned)

single crystals but consist of small domains [81]. Thus to respect these both effects an intermediate growth rate around $\approx 8\,\mathrm{mm/h}$ was chosen in this thesis and turned out to be a good choice resulting in high stoichiometric (twinned) single crystals of the prepared systems[2].

The only exception is the $(\mathrm{La,Sr})\mathrm{TiO}_3$ system which is known to grow only as polycrystals even with growing rates of $\approx 1\,\mathrm{mm/h}$ [52]. But obviously the here obtained $(\mathrm{La,Sr})\mathrm{TiO}_3$ crystals do not need this quality because they were grown for a neutron powder diffraction experiment (see [87, 88]) and therefore they were crushed into powder after growing.

When the growth rate of a particular system was chosen quite satisfactory (to obtain single crystals) then this value was not optimized any longer and kept constant. Because changing the growing speed would change the amount of evaporating material, which is obviously the most important parameter to maintain this evaporation effect.

### 3.3.4 Segregation Effects

At first the zone melting technique was used to eliminate impurities out of a crystal [77]. In general the concentration of a solvent in a liquid, $c_l$, and the solid phase, $c_s$, are not equal in the thermal equilibrium [53]

$$
\begin{aligned}
c_s &\neq c_l \\
\Leftrightarrow \frac{c_s}{c_l} &\neq 1.
\end{aligned}
\tag{3.3}
$$

Thus moving the melting zone with a length of $l$ through a bar with a length $L$ leads to a concentration gradient in the recrystallized part like shown in picture 3.6. Let the starting concentration of the impurities in the bar be $c_0$, then the concentration of the melting zone at the beginning is $c_0$, too. By moving the melting zone through the rod the melting zone is fed with material of the concentration $c_0$. On the other side of the melting zone recrystallizes material with a concentration $c_s = kc_l$. Thus in the general case depending on $k < (>)1$, travelling through the bar lets the concentration of impurities in the floating zone raise (lower). That means the concentration of the melting zone depends on the length of the recrystallized part of the bar. Thus the concentration $c_s$ in the recrystallized material is

---

[2]The precise value of the growing rate of the particular system is mentioned in the corresponding chapter.
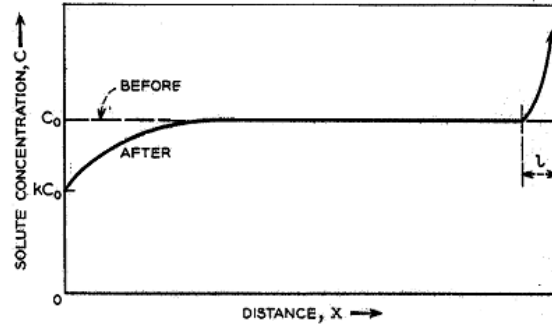
**Figure 3.6:** Concentration profile of a recrystallized rod by floating zone technique taken from [77].

also shifting with the growing length as shown in figure 3.6. A slightly different situation is the case $x < L - l$ also shown in 3.6. The melting zone is at the end of the feeding rod and so the zone cannot be fed with additional material.

One can see in picture 3.6 that the segregation effect is strongest at the beginning and at the end of a crystal growth but quite small in the middle. So first of all the very first and the very last part of a grown crystal were discarded to handle this problem.

For the earth alkaline doped systems $(Y,Ca)TiO_3$ and $(La,Sr)TiO_3$ it was to proof, if an segregation effect of the earth alkaline concentration like reported in [52] for the $(La,Sr)TiO_3$ occurs. In these two systems no concentration gradient was observable via EDX, what is in agreement with the results of [52], where no segregation effect was detected for the $(Y,Ca)TiO_3$ system, and for the $(La,Sr)TiO_3$ only at higher doping levels.

A significant segregation of the oxygen content occurred in the crystal growth of the $LaTiO_{3+\delta}$, $(La,Sr)TiO_3$ and $VO_2$ systems. This effect was countered by an opposite composition gradient of the feeding bar (details in chapter 3.7 and 3.12). In the other crystal systems this segregation was less pronounced, and hardly observable. This can be seen by means of the very good agreement of the lattice parameters or, if existing, transition temperatures of the top and bottom side of the crystals (details in the chapters of the particular crystal growth). Thus the estimated oxygen gradient in these

systems is

$$\Delta\delta < 0.005, \tag{3.4}$$

and therefore the valence of the metal ion varies less 0.01 in these crystals.

## 3.4 Educts

For preparation and growth of crystals containing rare earth elements or Lanthanum $RE_2O_3$ oxides were used. Before weighing, these oxides were dried in air at $900\,^\circ C$ for at least 12 hours. In the case of $Y_2O_3$ no pretreatment was necessary, because it is less hygroscopic. For titanium-containing crystals several Ti oxides, $TiO$, $Ti_2O_3$, $TiO_2$ and pure Ti, were used.

The nominal $TiO$ and $Ti_2O_3$ oxide educts exhibit small oxygen excess. Figure 3.7 shows the powder pattern of the $Ti_2O_3$ from the charge 21.11.04
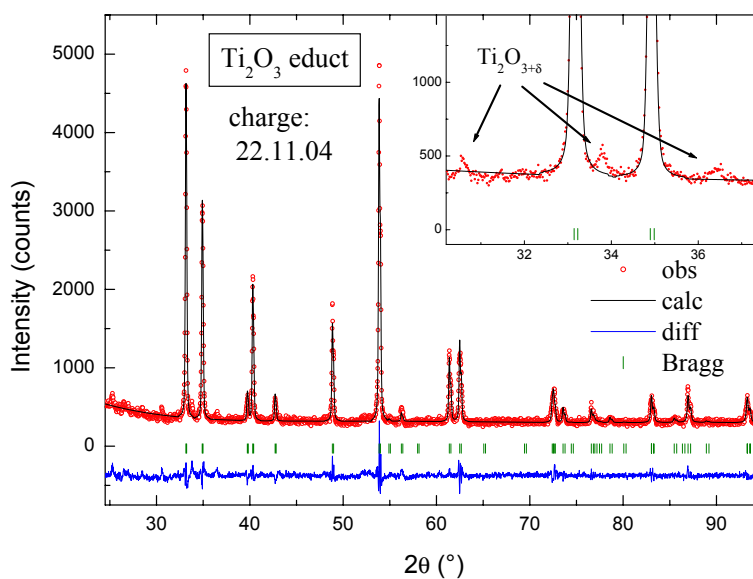


**Figure 3.7:** Diffractogram of the nominal $Ti_2O_3$ educt as bought containing Bragg peaks of an impurity phase which is a higher titanium oxide.

as bought. In the Bragg pattern peaks can be seen which don't belong to pure $Ti_2O_3$ but to a higher oxidized phase. Controlling the oxygen content

was the most crucial problem in the crystal growth in this thesis, hence knowing the oxygen content of the starting material is very important. Therefore the oxygen content was determined very thoroughly several times for each charge by TGA. The resulting values are listed in table 3.4 by the date when the respective charge was used the first time.

| Charge | Nominal | TGA |
|--------|---------|-----|
| 15.07.03 | $Ti_2O_3$ | $Ti_2O_{3.078}$ |
| 21.11.04 | $Ti_2O_3$ | $Ti_2O_{3.037}$ |
| 21.04.05 | $Ti_2O_3$ | $Ti_2O_{3.036}$ |
| 09.02.06 | $Ti_2O_3$ | $Ti_2O_{3.037}$ |
| 23.08.03 | $TiO$ | $TiO_{1.012}$ |
| 12.06.04 | $TiO$ | $TiO_{1.008}$ |

**Table 3.1:** Oxygen content of the Titanium oxide educts.

For later grown titanate crystals elementary Ti and $TiO_2$ were taken as educts because the valences of these materials are well defined. In $TiO_2$ the titanium is $Ti^{4+}$. It is the end point of the oxidizing reaction of titanium, and has noble gas electron configuration. Hence this Ti valence is very stable. Elementary Ti is the endpoint of a reduction reaction with hydrogen. Thus the oxygen content is well defined in this material, too.

Because of the same reasons for the growths of $VO_2$ and $NbO$ crystals a mixture of the elementary metals, vanadium and niobium and the oxides with a noble gas configuration, $V_2O_5$ and $Nb_2O_5$, were used.

Doping of the $VO_2$ with chromium was done via $Cr_2O_3$. Because of the low doping level (1% and 2%) of the crystals grown here, Oxygen deviations of $Cr_2O_3$ have practically no influence of the total oxygen content. Thus the exact valence of the Chromium in the $Cr_2O_3$ was not determined.

In the case of the solid solutions containing $CaTiO_3$, $CaCO_3$ was taken as educt and was reacted together with $TiO_2$ in a calcination reaction at a temperature of $1050\,°C$ for at least $15\,h$:

$$CaCO_3 + TiO_2 \longrightarrow CaTiO_3 + CO_2 \uparrow .  \tag{3.5}$$
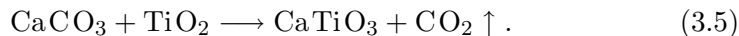
### 3.4.1 Preparing the Feeding Rod

After weighing the educts, they were mixed thoroughly in an agate mortar for at least 30 minutes. Then the powder was filled in latex tubes and pressed with a hydraulic press into two bars with a typical length of 7 cm and 3 cm. The longer one was taken as the feeding rod, the shorter one as seed for the growth. For the first crystals that I have grown [52] a standard procedure for single crystal growth was used. The pressed rods were sintered in airtight chamber furnaces in an argon atmosphere by solid state reaction at a temperature $T \approx 1400\,^\circ$C for $\approx 15\,$h [89, 90].



**Figure 3.8:** Parts of an inhomogeneously oxidized $YTiO_3$ bar due to sintering in a chamber furnace.

Parts of a $YTiO_3$ rod which was sintered in such a way are shown in picture 3.8. The white color of parts of this bar is indicating that these parts are totally oxidized and the Ti exhibits a $3d^0$ electron configuration. Hence such reactions in these furnaces are unsuitable for controlling the oxygen content.

But controlling the oxygen content was the most essential aspect for the crystals grown in this thesis. Therefore to avoid any uncontrolled oxidation the bars were not prereacted, but the unreacted feeding rods were directly loaded in the floating zone furnace for the crystal growth after pressing them[3]. As an additional advantage of this new variant, the growth is much faster, because of skipping reaction steps, which take typically several days. So it is in principle possible to to obtain a single crystal in only one day.

---

[3]Except $CaTiO_3$, this was calcined before using. There the Ti has already a $3d^0$ electron configuration and can't be further oxidized.

## 3.5   NbO

Even without such solid state reactions, but doing the reaction and the single crystal growth in one preparing step in the floating zone furnace, does not mean that the composition of the starting material stays unchanged during crystal preparation. Evaporation of one (or even more) components can happen. In general these processes are crucial for the valence of the transition metal ions and therefore crucial for the behavior of the obtained samples. So for obtaining highly stoichiometric crystals – that means deviations of the valency of only $\approx 0.01$ – an itineration of the growth of the same material was done. After growing one crystal, the resulting composition of the obtained crystal was analyzed with various methods like, thermogravimetry (TGA), or more indirectly, via lattice parameters and magnetization measurements. Then for the next crystal growth the composition of the educts was changed correspondingly until the quality of the obtained crystals was high enough for the planned experiments.

For example this can be seen very nicely by means of the growth of $NbO$. For a first crystal, HR146, elementary Nb and $Nb_2O_5$ was weighed in a nominal mixture of $NbO_{1.085}$ in expectancy of a slightly reduction of the niobium in inert atmosphere by vaporization [91]. As growing atmosphere argon with an overpressure of $5\,bar$ and an gas flow of $0.800\,l/min$ was chosen. The rotation speed of $13\,rpm$ was used for the upper shaft, while the lower shaft was not rotated to avoid turbulences in the recrystallization region. The growth rate was set to 8 mm/h. At a power of $2400\,W$ the melting zone could be established and was stable during the whole crystal growth.

The so grown crystal HR146 has a grey color and can easily be cleaved along the (100) plane shown in picture 3.9. Single crystallinity was analyzed by Laue photography. The comparison of the Laue pattern of the top and bottom side of the crystal HR146 are shown in figure 3.10 indicating that the obtained crystal is a single crystal. Therefore the parameters of crystal growth, especially the growing speed were chosen quite well, and a change is not needed.

But the X-ray powder diffractogram (XPD)[4] of this crystal shows structural impurities of an $NbO_x$ phase (see figure 3.11). A first rough measure-

---

[4] All diffractograms shown in this thesis were recorded with a Cu X-ray tube as light source with a corresponding wave length of $\lambda_{\alpha 1} = 1.5444\,\text{Å}$ and $\lambda_{\alpha 2} = 1.5406\,\text{Å}$ [92] . The
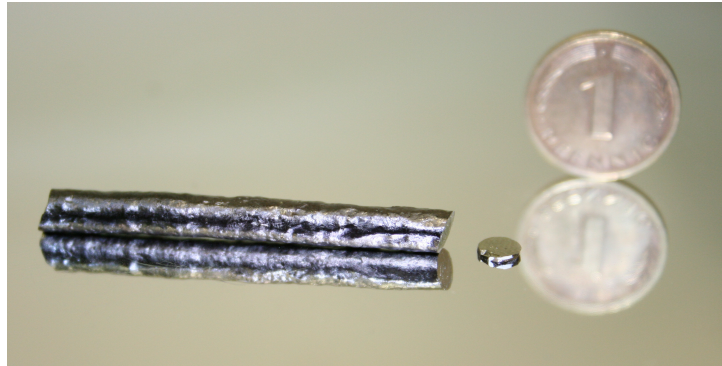
**Figure 3.9:** The first obtained $NbO$ crystal HR146.

ment of the oxygen content by TGA results in $NbO_{1.06}$. Therefore for the next crystal growths the oxygen content was lowered step by step.

Finally for the crystal HR156 a starting composition of nominal $NbO_{0.974}$ was chosen and pulled under the same conditions like the further $NbO$ crystals. In contrast to the other crystal growths a strong facetting during the growth could be seen and this crystal HR156 shows a more regular

---

data were analyzed with the program FullProf [93].
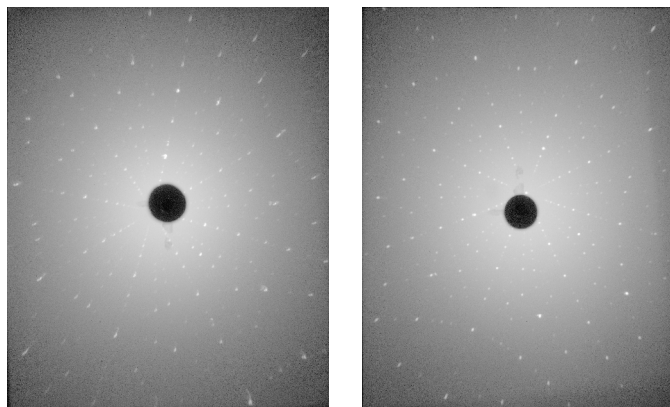


**Figure 3.10:** Laue pattern of the top and bottom side of the first $NbO$ crystal HR146 indicating single crystallinity.
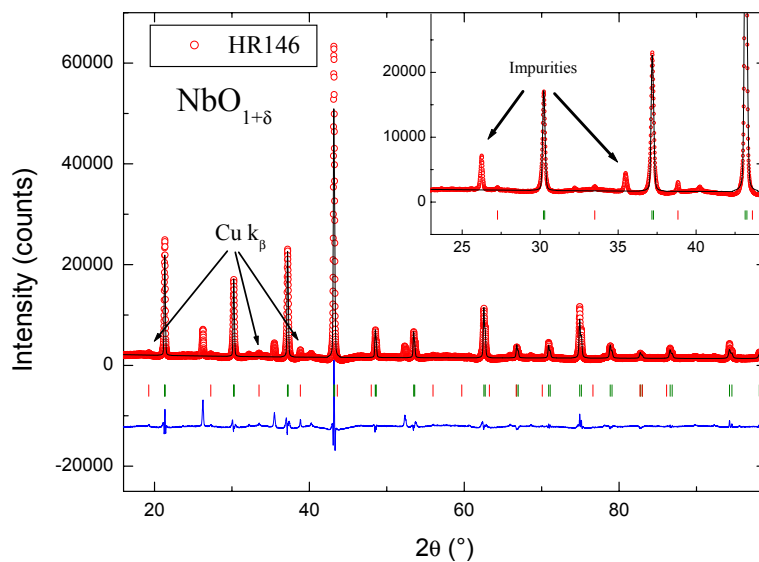
**Figure 3.11:** In the X-ray diffractogram of the NbO crystal HR146 additional Bragg peaks of an impurity phase can be seen. The red marked Bragg positions result from a small $Cu-k_\beta$ content in the X-ray beam.

surface than the other obtained crystals (see figure 3.12). The XPD of the crystal HR156 in figure 3.13 shows no impurities and the oxygen content
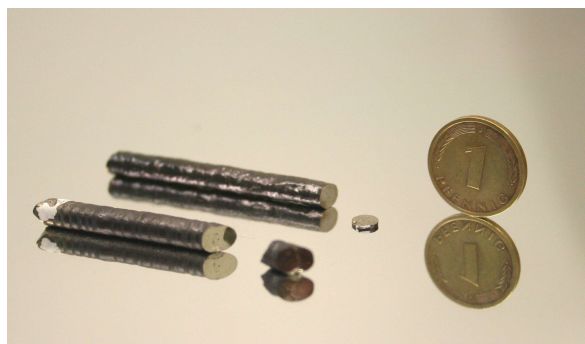


**Figure 3.12:** Two NbO crystals. The more regular grown crystal in the front HR156 has a well defined oxygen content, while the crystal in the back is not of pure phase.
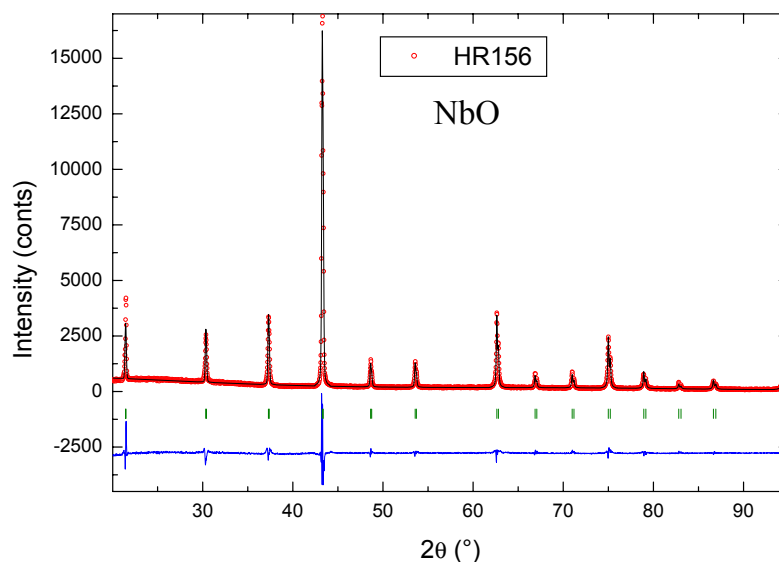
**Figure 3.13:** X-ray powder diffractogram of the NbO crystal HR156. No impurities can be seen.

and was determined by TGA to NbO$_{1.005}$.

## 3.6   Ti$_2$O$_3$

For a first crystal, HR85, a stoichiometric mixture of the educts Ti$_2$O$_{3+\delta}$ and TiO$_{1+\delta}$ was weighed in and mixed thoroughly in an agate mortar like described in [52]. Then the powder was pressed into two rods. For Ti$_2$O$_3$ this process is very crucial because the bars break very easily.

As growth atmosphere argon with an overpressure of 1.8 bar was used which is the standard pressure for inert atmospheres in this thesis. To stir the melt and to level an horizontal temperature gradient the rotation speed of the upper shaft was set to 13 rpm while the lower shaft was not rotated to minimize turbulences in the crystallization region. The growing speed was set to 8 mm/h and the relative feeding speed to 1 mm/h. During the whole crystal growth the melting zone was very stable. The obtained crystals show a blue shiny color at their grown surface while cleaving planes are shiny purple. Via TGA the determined oxygen content of this crystal HR85 is

$Ti_2O_{3.007}$ what is quite acceptable. Nevertheless to optimize stoichiometry for the later grown crystals a starting mixture of nominal $Ti_2O_{2.995}$ was used. The diffractogram of a sample[5] of the so grown $Ti_2O_3$ crystal is
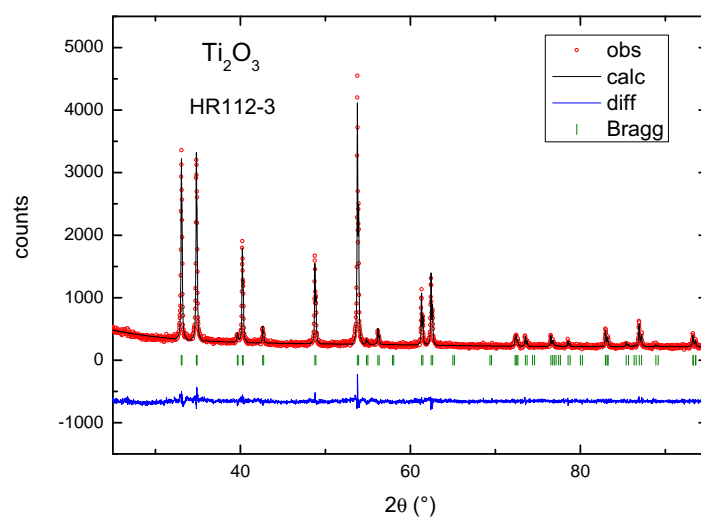


**Figure 3.14:** X-ray diffractogram of the $Ti_2O_3$ crystal HR112 indicating phase purity.

shown in figure 3.14 and exhibits no structural impurities (like the crystal HR85 too), indicating a very high stoichiometry. The structural data of the grown $Ti_2O_3$ crystals are listed in table 3.6.

### 3.6.1 Single Crystallinity

All the grown crystals were identified as single crystals by Laue photography and polarization microscopy as described in [52]. The Laue pictures of the top and bottom side of the crystal HR162 are shown in figure 3.15 indicating that domains with the same orientation were observed. The in-

---

[5]When a crystal was cut the samples were top down numbered, for example HR112-3 means the used sample was the third piece start counting from the top of the crystal

| Sample | $a$ (Å) | $b$ (Å) | $c$ (Å) |
|--------|---------|---------|---------|
| HR85-2 | 5.154 | 5.154 | 13.613 |
| HR85-4 | 5.152 | 5.152 | 13.606 |
| HR112-2 | 5.148 | 5.148 | 13.603 |
| HR112-3 | 5.148 | 5.148 | 13.603 |
| HR116-4 | 5.152 | 5.152 | 13.606 |
| HR162-2 | 5.148 | 5.148 | 13.624 |
| HR162-4 | 5.148 | 5.148 | 13.625 |

**Table 3.2:** Lattice parameters of the Ti$_2$O$_3$ crystals.

vestigated surface via polarization microscopy looks homogeneous and is changing the color when rotating the crystal, shown in figure 3.16, what is a strong evidence for single crystallinity.

HR112.
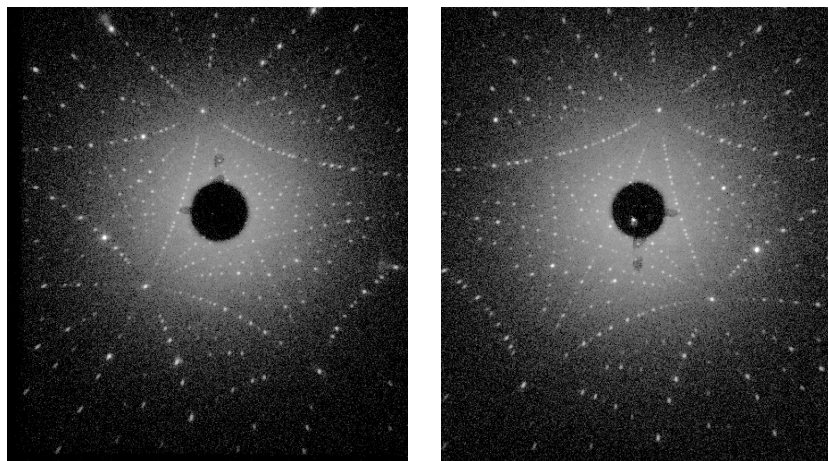


**Figure 3.15:** The Laue photos of the crystal HR162 indicating single crystallinity.
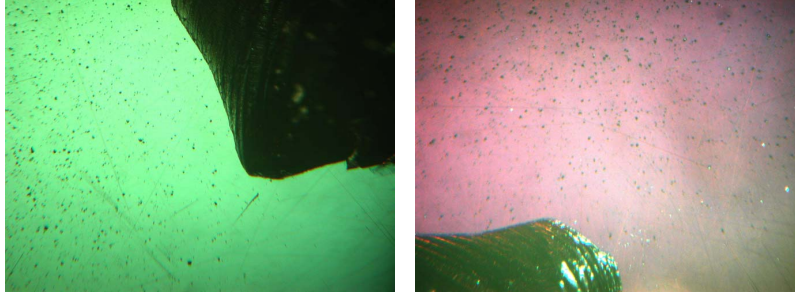
**Figure 3.16:** Pictures of a polished dish of the crystal HR162 in the polarization microscope. The different colors due to different sample orientations and the homogeneous color of the surface are indicating that the sample is a single domain crystal.

## 3.7   LaTiO$_3$

For an inelastic neutron spectroscopy experiment LaTiO$_3$ crystals should be grown [94]. The crystals should be of very precise stoichiometry with a $T_N >$ 145 K, what means an oxygen excess $\delta < 0.005$, which is nearly the same value than the error of TGA measurements. This is corresponding value is corresponding to a lattice constant $a \geq 5.633$ Å. The LaTiO$_3$ crystals grown in [52] exhibit a small oxygen gradient along the growing axis, where the lower part has slightly more oxygen than the upper part. Hence to balance this oxygen inhomogeneity, a gradient of also $\Delta\delta = 0.005$ was weighed in the feeding bar, with less oxygen content at the bottom side. For a first crystal growth a composition of LaTiO$_{2.92}$ at the top and LaTiO$_{2.915}$ at the bottom of the feeding rod was used. The growing speed was settled to 7.00 mm/h and the upper shaft was moved into the melting zone with a speed of 2.00 mm/h.

The obtained crystal was characterized by magnetization measurements and shows a Néel transition at $T_N \approx 130$ K (see table 3.7). Thus the Néel temperature of this crystal, HR88, is $\approx 20$ K too low, indicating an oxygen excess of $\Delta\delta \approx 0.01$. Furthermore the crystal has a small oxygen gradient along the growth axis, manifested in the different $T_N$'s of the upper and lower part of this crystal (figure 3.18). Powder X-ray diffraction was also done and the results are presented in table 3.7, too. Also the lattice parameters are slightly smaller than reported for highly stoichiometric LaTiO$_3$ samples [20]
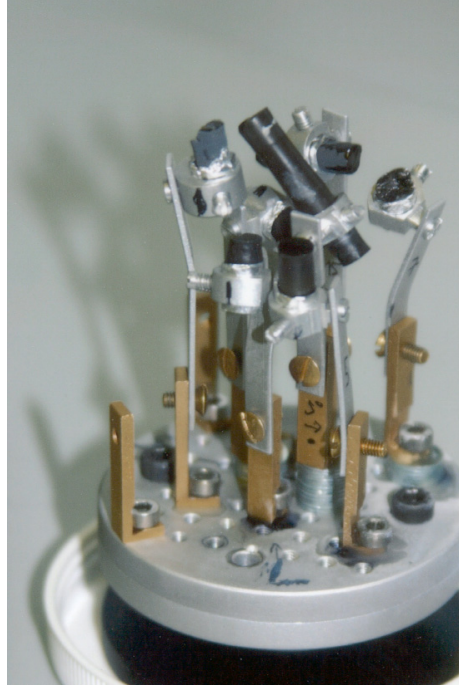
**Figure 3.17:** Ensemble of orientated La TiO$_3$ crystals grown in this thesis.

indicating an oxygen excess, too. Hence for a next crystal the oxygen content

| Sample | $a$ (Å) | $b$ (Å) | $c$ (Å) | $T_N$ (K) |
|--------|---------|---------|---------|-----------|
| HR88-2 | 5.630 | 5.609 | 7.917 | 136 |
| HR88-4 | 5.620 | 5.602 | 7.611 | 124 |

**Table 3.3:** Results of the characterization of the crystal HR88.

of the feeding bar was lowered. Additionally the oxygen gradient was raised to a value of

$$\Delta\delta = 0.01, \tag{3.6}$$

to reach high homogeneity. The obtained crystal, HR89, is more homogeneous what can be seen by means of the characterization data shown in table 3.7. This crystal has nearly no oxygen gradient, but the oxygen con-

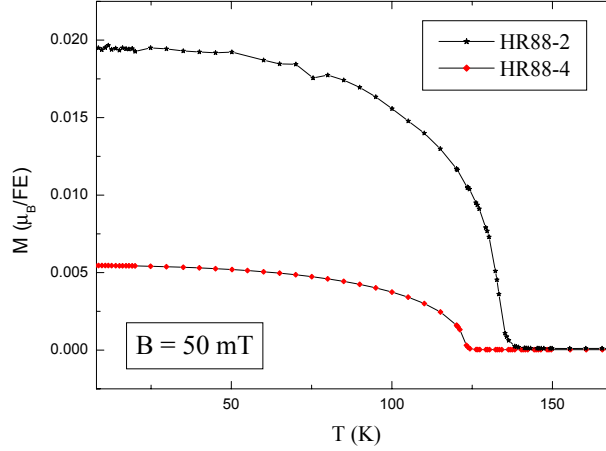tent is still to high. Therefore for further grown crystals the oxygen content



**Figure 3.18:** Magnetization $M(T)$ of the upper (-2) and lower part (-4) of the crystal HR88 indicating a small oxygen gradient along the grown crystal.

| Sample | $a$ (Å) | $b$ (Å) | $c$ (Å) | $T_N$ (K) |
|--------|---------|---------|---------|-----------|
| HR89-2 | 5.629 | 5.611 | 7.915 | 140 |
| HR89-4 | 5.628 | 5.610 | 7.614 | 137 |

**Table 3.4:** Lattice parameters and $T_N$ of the crystal HR89.

was lowered step by step until a crystal, HR92, with a Néel temperature of $T_N = 148 \, \text{K}$ could be obtained, which is among the highest reported for $LaTiO_3$ [20,58] indicating high stoichiometry. In figure 3.19 the magnetization curve of the upper (HR92-2) and lower part (HR92-4) can be seen. The measured samples have nearly identical Néel temperatures, thus the crystal shows practically no oxygen gradient, too. Therefore the weighted oxygen gradient and content was chosen quite well. Further crystals were grown in the same way to get enough material for the planned neutron experiment. The characterisation data of these crystals are shown in table 3.7. A typical X-ray diffractogram is presented in figure 3.20, too.
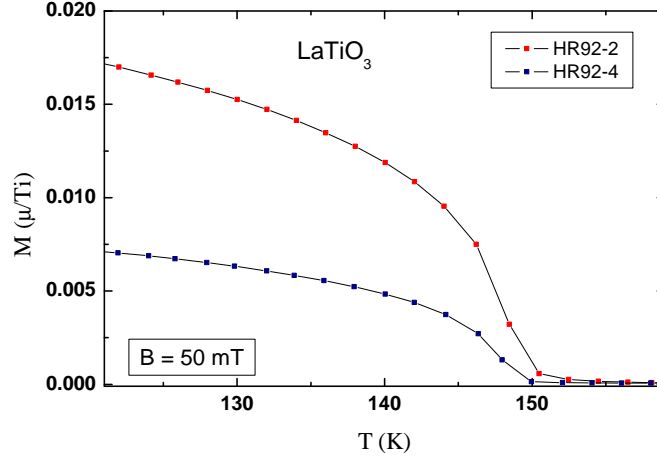
**Figure 3.19:** The magnetization $M(T)$ of the top (HR92-2) and bottom (HR92-4) part of the crystal HR92 indicates very high homogeneity and stoichiometry.

### 3.7.1 LaTiO$_{3+\delta}$

LaTiO$_3$ can be doped with charge carriers by varying the oxygen content. With oxygen excess $\delta$, holes were injected and the electron configuration becomes $d^{1-2\delta}$. For detailed structure investigations [87] of so doped LaTiO$_3$, crystals should be grown [94]. The first crystal growth of the LaTiO$_{3+\delta}$ was done with exactly the same parameters as the undoped LaTiO$_3$ except of the oxygen content of the feeding rod. It was varied by different ratios of the titanium oxides (or pure titanium) used as starting material.

In contrast to the pure LaTiO$_3$ the so grown crystals exhibits a much stronger oxygen gradient due to the growth. For example the crystal HR104 was grown with a weighted oxygen gradient of $\Delta\delta = 0.01$, but the obtained crystal is less homogeneous than the undoped crystals. This can be seen by means of the lattice parameters of the top and bottom part of the crystal listed in table 3.7.1. Therefore in later crystal growths the oxygen gradient was enhanced systematically up to a value of $\Delta\delta = 0.04$. The obtained crystals possess then only a small oxygen gradient, what can be seen for example by the lattice parameters of crystal HR109 in table 3.7.1. The oxygen slope of the obtained crystal is now small enough to cut samples with a well
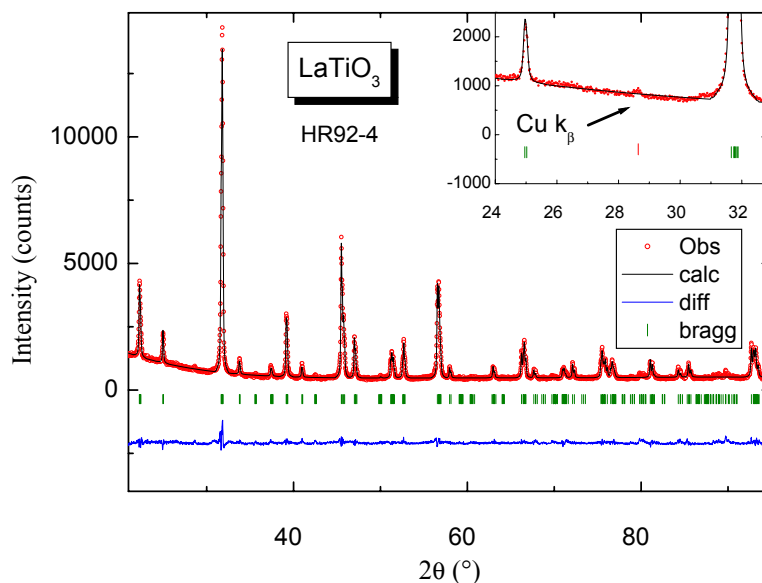
**Figure 3.20:** X-ray powder pattern of $LaTiO_3$.

defined oxygen content. As result of this project several $LaTiO_{3+\delta}$ crystals with different oxygen contents could be obtained. Some parts of these crystals are shown in figure 3.21. Lattice parameters and Néel temperatures of this doping series are shown in figures 3.22 and 3.23.



**Figure 3.21:** Some crystals of the $LaTiO_{3+\delta}$ series.

| Sample | $a$ (Å) | $b$ (Å) | $c$ (Å) | $T_N$ (K) |
|---|---|---|---|---|
| HR92-2 | 5.636 | 5.619 | 7.916 | 148 |
| HR92-4 | 5.636 | 5.619 | 7.617 | 149 |
| HR93-2 | 5.634 | 5.616 | 7.915 | 148 |
| HR93-4 | 5.636 | 5.619 | 7.617 | — |
| HR94-2 | 5.635 | 5.618 | 7.920 | 148 |
| HR94-3-3 | — | — | — | 148 |
| HR95-2 | 5.636 | 5.619 | 7.916 | 150 |
| HR95-4 | — | — | — | 148 |
| HR96-2 | 5.637 | 5.619 | 7.917 | 150 |
| HR96-4 | 5.635 | 5.617 | 7.617 | 150 |
| HR102-2 | 5.633 | 5.614 | 7.915 | 145 |
| HR102-4 | 5.635 | 5.617 | 7.618 | 147 |
| HR103-2 | 5.635 | 5.617 | 7.917 | — |
| HR103-4 | 5.634 | 5.614 | 7.616 | 148 |
| HR114-2 | 5.635 | 5.617 | 7.918 | — |
| HR114-3-3 | 5.637 | 5.619 | 7.616 | — |
| HR115-2 | — | — | — | 149 |
| HR115-4 | 5.636 | 5.618 | 7.618 | — |

**Table 3.5:** Characterization data of the grown La TiO$_3$ crystals.

### Determination of the Oxygen Content

In principle the oxygen content of La TiO$_{3+\delta}$ can be determined by TGA directly. But this method is very susceptible for systematic errors [52]. The

| Sample | $a$ (Å) | $b$ (Å) | $c$ (Å) |
|---|---|---|---|
| HR104-2 | 5.626 | 5.607 | 7.914 |
| HR104-4 | 5.613 | 5.596 | 7.908 |

**Table 3.6:** The lattice parameters of the top and bottom side of the crystal HR104 are differing strongly from each other.

| Sample | $a$ (Å) | $b$ (Å) | $c$ (Å) |
|--------|---------|---------|---------|
| HR109-2 | 5.589 | 5.579 | 7.896 |
| HR109-4 | 5.592 | 5.580 | 7.900 |

**Table 3.7:** Lattice parameters of the top and bottom side of the crystal HR109 indicating high homogeneity.

required precision of the specified mass should be at least

$$\Delta m < 0.003 \, \text{mg}. \tag{3.7}$$

But nobody would do such a precise weighing with a balance staying in an gas flow and heating it up to $1000\,°\text{C}$, as done in TGA measurements. So it was impossible to determine the Oxygen content by TGA for all samples, because of the very high experimental effort for accurate TGA investigations.

Alternatively the Oxygen content can be estimated via the lattice parameters (or the Néel temperature $T_N$, too). Here the lattice constant $a$ of the Pbnm space group is the most suited because it varies strongest with
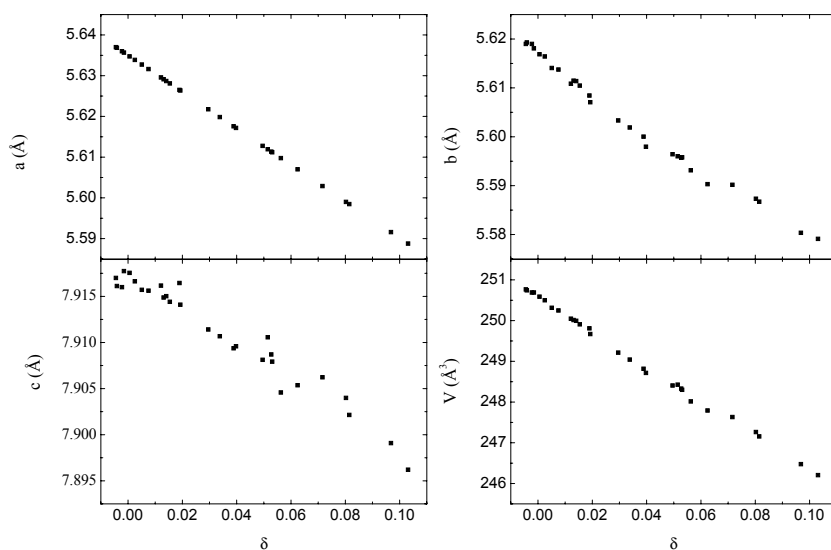


**Figure 3.22:** Lattice constants and cell volume of $\text{La TiO}_{3+\delta}$.
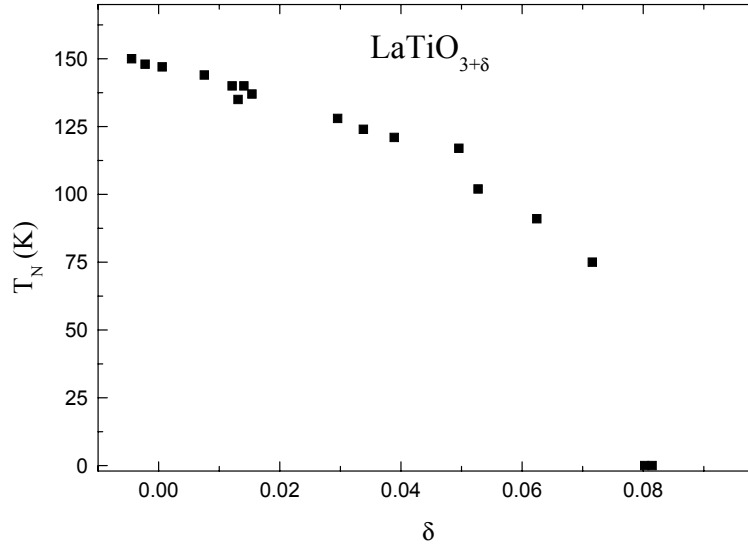
**Figure 3.23:** Oxygen content depending $T_N$ of La TiO$_{3+\delta}$.

the oxygen content. For that the oxygen of several La TiO$_{3+\delta}$ samples were measured by TGA very thoroughly to get reliable data. These values were used as nodes for a linear fit of the lattice constant $a$ to estimate the oxygen content (see figure 3.24). The equation which is describing this linear fit is,

$$a = (6.9789 - 0.44846 \cdot (3 + \delta)) \, \text{Å}, \tag{3.8}$$

what leads to an excess oxygen estimation equation,

$$\delta = \frac{5.6352 - a/\text{Å}}{0.44846}. \tag{3.9}$$

### 3.7.2 Single Crystallinity

All the grown crystals were tested for single crystallinity by Laue photography. For example Laue pictures of the upper and the lower part of such a crystal (HR103) are shown in figure 3.25 indicating (twinned) single crystallinity. Single crystallinity was also proved by polarization microscopy on polished surfaces of the crystals, what is shown in picture 3.26. The surfaces show a stripe-like domain pattern which is typical for a twinning along the pseudo cubic (100) axis. On the other hand the measured magnetic moment
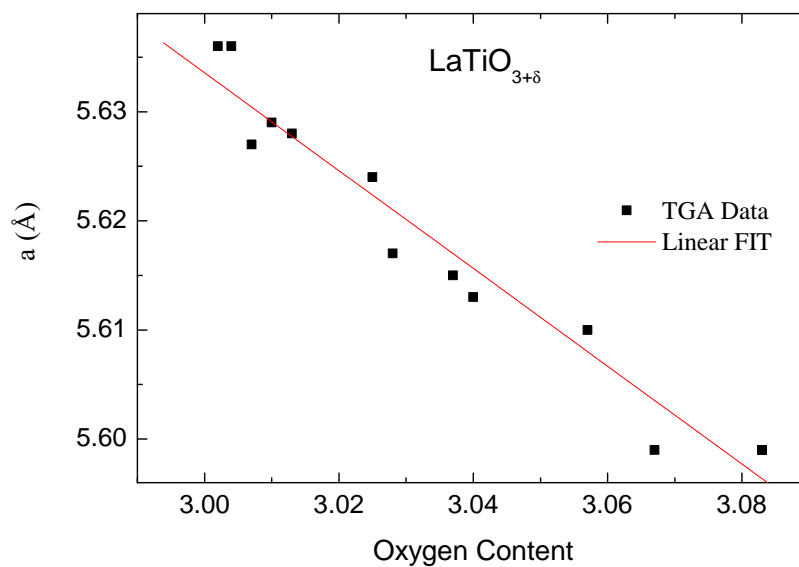
**Figure 3.24:** Determination of the oxygen content via the lattice constant $a$.

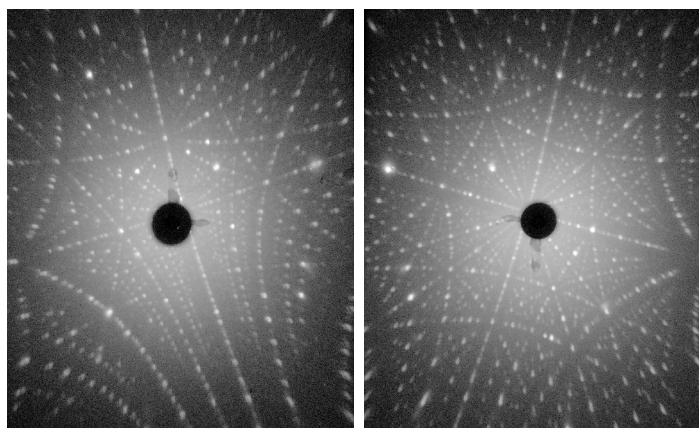of different $LaTiO_3$ samples (see figure 3.18 and 3.19) differ strongly from



**Figure 3.25:** Laue pictures of the front and backside of the $LaTiO_3$ crystal HR103.

**Figure 3.26:** Strip-like domain pattern of the LaTiO$_3$ sample HR92-2 observed via polarization microscopy. In the right picture the sample was turned 90° hence the light stripes become dark, indicating different domain orientation.

each other, indicating a strong anisotropy, thus there is strong evidence for at least one untwinned axis in some of the grown LaTiO$_3$ crystals, which should be the c axis.

### 3.7.3  Structural Phase Width

As reported in [90] a structural phase transition from orthorhombic Pbnm to a tetragonal Immm phase appears at an oxygen doping level of LaTiO$_{3.18}$. On the other side the phase boundary of oxygen deficit, LaTiO$_{3-\delta}$, is not reported yet.

In figure 3.27 the magnetization curves of several LaTiO$_3$ crystals can be seen. The Néel temperature of the sample HR96-2 is with $T_N \approx 150\,\mathrm{K}$ higher than the $T_N$ of all the other samples, here. But in the diffractogram of this sample (figure 3.28) Bragg peaks of a second phase can be seen.

So, on the one hand the $T_N$ is slightly higher than that of the other samples, indicating that this sample should be the most stoichiometric LaTiO$_3$. On the other hand the additional Bragg peaks indicate a second phase in the diffractogram as a result of slight oxygen underdoping: LaTiO$_{3-\delta}$. Hence the phase boundary of oxygen underdoping is very close to the stoichiometric composition at an oxygen deficit $\delta_{PT}$:

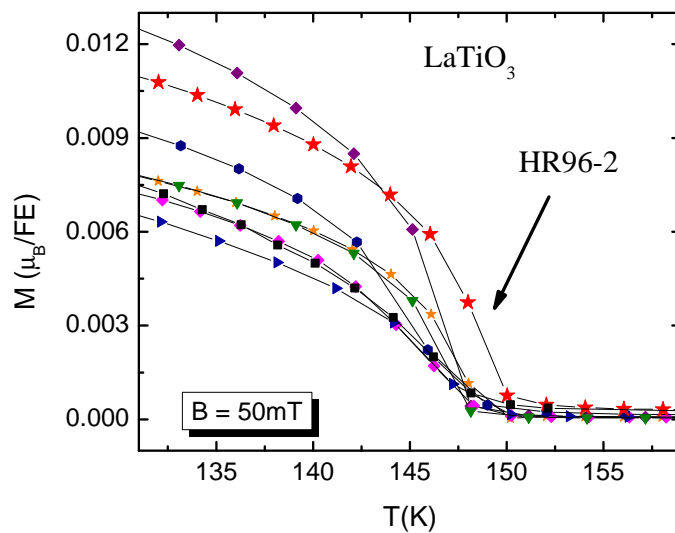$$\delta_{PT} \leq 0.005. \tag{3.10}$$

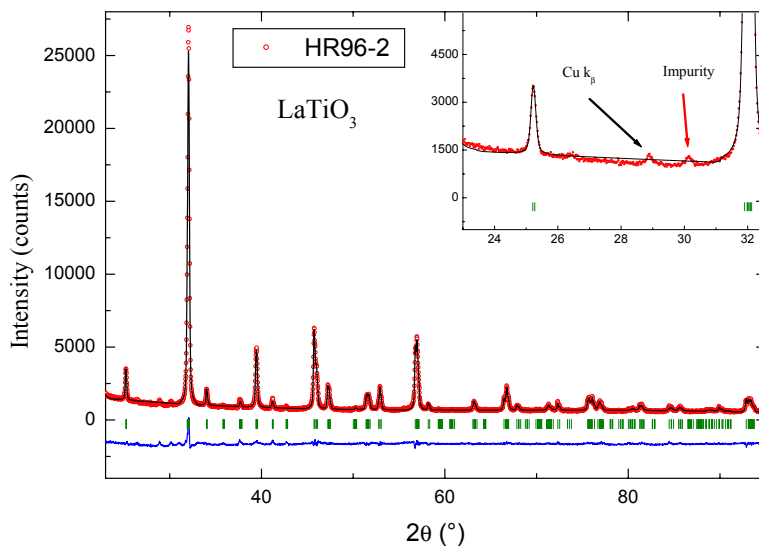**Figure 3.27:** Magnetization curves of different La TiO₃ samples.



**Figure 3.28:** Diffraction pattern of the sample HR96-2. Bragg peaks of an impurity phase are indicating oxygen deficit.

### 3.7.4 La$_{0.96}$Sr$_{0.04}$TiO$_3$

Alternatively LaTiO$_3$ can be hole doped by substituting trivalent La$^{3+}$ ions through divalent Sr$^{2+}$ ions: La$_{1-x}$Sr$_x$TiO$_3$. Then the titanium gets a $d^{1-x}$ electron configuration. For a comparison between the oxygen and the strontium doped LaTiO$_3$ systems a La$_{0.96}$Sr$_{0.04}$TiO$_3$ sample should be prepared, big enough for structural investigations via neutron scattering [94], because this compound has comparable lattice parameters and T$_N$ to the LaTiO$_{3.05}$ sample investigated via neutron diffraction in [87], which are: $T_N = 110$ K, $a = 5.615$ Å, $b = 5.600$ Å and $c = 7.910$ Å.

As reported in [52] the melting point of the compound La$_{0.96}$Sr$_{0.04}$TiO$_3$ can hardly be reached with the used floating zone furnace. Thus the diameter of the feeding bars was reduced from $\approx 6$ mm, what is the standard diameter used in this thesis, to $\approx 4$ mm to lower the needed power for the crystal growth. For the first crystal grown in such a way, a slightly lower oxygen content than for the undoped LaTiO$_3$ was chosen in expectation of a stronger oxidation through evaporation, caused by the higher melting point. Additionally the feeding rod was prepared with an oxygen gradient like for the undoped LaTiO$_3$ crystals, too. So the nominal composition of the feeding rod was La$_{1-x}$Sr$_x$TiO$_{2.85}$ for the lower and La$_{1-x}$Sr$_x$TiO$_{2.865}$ for the upper part. As another change the growing speed was settled quite high to 10 mm/h, because even twinned single crystallinity is practically not reachable with the floating zone technique [52] in this system, and moreover it is not needed for the planned experiment, which is a powder neutron scattering experiment.

The lattice parameters of the so grown crystal, HR119, are listed in table 3.7.4. They are even much smaller than the lattice parameters of 5%

| Sample | $a$ (Å) | $b$ (Å) | $c$ (Å) |
|---|---|---|---|
| HR119-2 | 5.578 | 5.564 | 7.878 |
| HR119-4 | 5.580 | 5.567 | 7.879 |

**Table 3.8:** Lattice parameters of the La$_{0.96}$Sr$_{0.04}$TiO$_3$ crystals HR119.

Sr doped LaTiO$_3$ [52, 95] indicating a strong oxygen excess. Hence with a thinner feeding rod the oxidizing effect through evaporation seems to be much stronger. The enhancement of the surface of the feeding rod in ratio

to its volume could cause this effect.

Therefore in the next crystal growths the oxygen content of the feeding rod was reduced by 0.06. The oxygen gradient was not changed, because the lattice parameters of the top and bottom side of the crystal HR119 (see table 3.7.4) are nearly equal.

While the lattice parameters of the first so grown crystal, HR122, are slightly to small indicating oxygen excess, the lattice parameters of another crystal grown with identical parameters, HR126, exhibits lattice parameters which are comparable to those of pure $LaTiO_3$ (see table 3.7.4). In figure

| Sample | $a\,(\text{Å})$ | $b\,(\text{Å})$ | $c\,(\text{Å})$ |
|---------|-------|-------|-------|
| HR122-3 | 5.607 | 5.592 | 7.907 |
| HR126-2 | 5.636 | 5.618 | 7.920 |
| HR126-4 | 5.533 | 5.615 | 7.921 |

**Table 3.9:** Lattice parameters of the two $La_{0.96}Sr_{0.04}TiO_{3\pm\delta}$ crystals grown under the same conditions.

3.30 the magnetization curve of a sample of the crystal HR126 is shown. Also the Néel temperature is with $T_N = 146\,\text{K}$ as high as the one of pure $LaTiO_3$. Hence the titanium seems to exhibit nearly a perfect $d^1$ electron configuration what means that the oxygen content is much lower than in the crystal HR122.

Thus caused through the very strong evaporation effect by using the thinner feeding rods the oxygen content becomes uncontrollable. To underline this, in table 3.7.4 the nominal composition of the feeding rods together with the resulting lattice parameters and Néel temperatures of different crystal growths are listed.

Finally for the next crystal, HR130, the diameter of the feeding bar was raised to the value of the feeding bars used for the undoped and oxygen doped $LaTiO_3$. The oxygen content was 2.87 for the bottom and 2.88 for the top side which are exact the same values as used for the undoped $LaTiO_3$ as is the chosen growth speed. To accommodate for the higher melting point both the upper and lower shaft were not rotated. Hence the growth could happen also with only partly molten material.

The resulting lattice parameters of the so grown $La_{0.96}Sr_{0.04}TiO_{3\pm\delta}$ crystal are in good agreement with the aimed for values (see table 3.7.4)
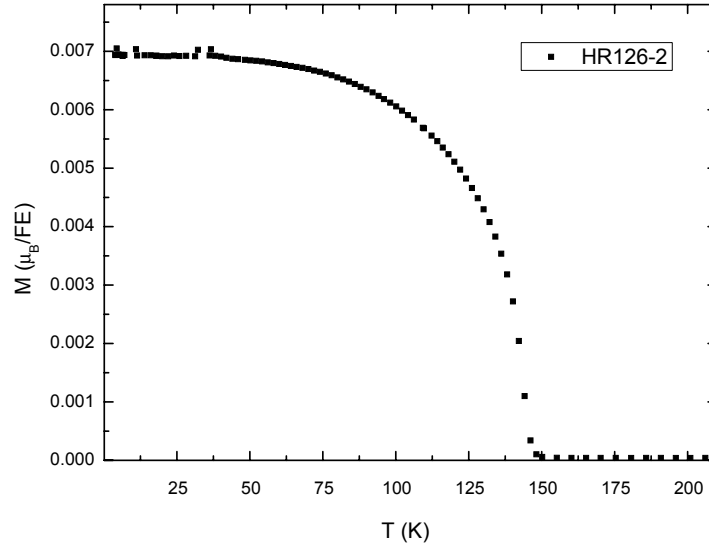
**Figure 3.29:** Magnetization curve of the crystal HR126. The Néel temperature is nearly as high as the one of pure LaTiO$_3$ indicating an oxygen deficit of $\delta \approx 0.02$.

indicating only small deviations of the oxygen content:

$$|\delta| \leq 0.005. \tag{3.11}$$

Also the Néel temperature of the crystal HR130 matches nicely to these of the top and bottom side of the LaTiO$_{3.05}$ sample, HR108-3[6], which was used for structural investigations in [87].

---

[6]The different T$_N$ of the two LaTiO$_{3.05}$ samples originates from a small deviation of the oxygen content, which is less than 0.005 (see figures 3.22 and 3.23).

| Oxygen content | Sample | $a\,(\text{Å})$ | $b\,(\text{Å})$ | $c\,(\text{Å})$ | $T_N\,(\text{K})$ |
|---:|---|---|---|---|---|
| 2.865 | HR119-2 | 5.578 | 5.564 | 7.878 | 0 |
|  | HR119-4 | 5.580 | 5.567 | 7.879 | — |
| 2.83 | HR121-2 | 5.585 | 5.574 | 7.892 | — |
|  | HR121-4 | 5.585 | 5.577 | 7.892 | — |
| 2.805 | HR122-3 | 5.607 | 5.592 | 7.907 | 80 |
| 2.785 | HR124-2 | 5.633 | 5.616 | 7.917 | 145 |
|  | HR124-4 | 5.634 | 5.615 | 7.918 | 145 |
| 2.795 | HR125-2 | 5.627 | 5.608 | 7.918 | — |
|  | HR125-4 | 5.627 | 5.608 | 7.917 | — |
| 2.803 | HR126-2 | 5.636 | 5.618 | 7.920 | 146 |
|  | HR126-4 | 5.533 | 5.615 | 7.921 | — |
| 2.818 | HR127-2 | 5.613 | 5.597 | 7.913 | — |
|  | HR127-4 | 5.600 | 5.590 | 7.906 | — |
| 2.812 | HR128-2 | 5.630 | 5.610 | 7.919 | — |
|  | HR128-3 | 5.626 | 5.608 | 7.919 | — |
|  | HR128-4 | 5.622 | 5.603 | 7.915 | 118 |
| 2.815 | HR129-2 | 5.635 | 5.618 | 7.919 | — |
|  | HR129-4 | 5.629 | 5.511 | 7.921 | 128 |

**Table 3.10:** The resulting lattice parameters and $T_N$'s of different $\text{La}_{0.96}\text{Sr}_{0.04}\text{TiO}_{3\pm\delta}$ crystals grown with thin feeding bars in comparison to the nominal oxygen content of the starting material. The listed values of the oxygen content hold for the top of the feeding rods. The bottom side of the feeding rods had 0.015 less oxygen. The absence of a systematic relation indicates that the oxygen content is uncontrollable when the crystals were grown in such a way.

| Sample | $a$ (Å) | $b$ (Å) | $c$ (Å) |
|---|---|---|---|
| LaTiO$_{3.05}$ | | | |
| HR108-2 | 5.618 | 5.600 | 7.909 |
| HR108-3-2 | 5.611 | 5.596 | 7.908 |
| La$_{0.96}$Sr$_{0.04}$TiO$_3$ | | | |
| HR130-3-2 | 5.621 | 5.603 | 7.914 |
| HR130-4 | 5.516 | 5.598 | 7.912 |

**Table 3.11:** Lattice parameters of the La$_{0.96}$Sr$_{0.04}$TiO$_3$ crystal HR130 in comparison with these of the LaTiO$_{3.05}$ crystal HR108.
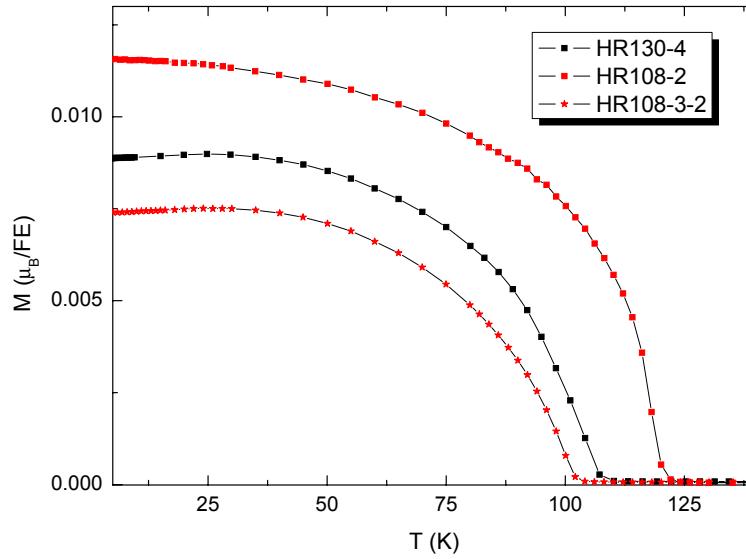


**Figure 3.30:** Magnetization curves of LaTiO$_{3.05}$ (HR108) and the La$_{0.96}$Sr$_{0.04}$TiO$_3$ sample HR130 have comparable Néel temperatures.

## 3.8 YTiO$_3$

For a detailed structure analysis via neutron diffraction (see [57,87]) YTiO$_3$ crystals should be grown [94]. As starting point a nominal composition of YTiO$_{2.89}$ was chosen for the feeding rod of the crystal HR70. The crystal was pulled with an growing speed of $6.20\,\mathrm{mm/h}$ under an inert argon atmosphere with 1.8 bar over pressure. Additionally the feeding rod was moved into the melting zone with $1\,\mathrm{mm/h}$. A black crystal with a length of
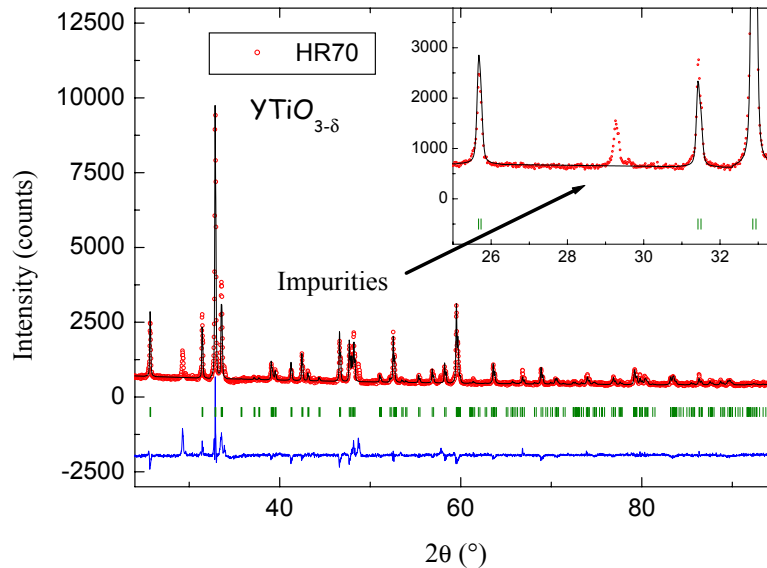


**Figure 3.31:** The XPD of the sample HR70-2 exhibits additional Bragg peaks from an impurity phase.

$\approx 30\,\mathrm{mm}$ could be obtained. The X-ray powder diffractogram of a sample of this crystal is shown in figure 3.31. In the area of $2\theta \approx 28\,^\circ$ Bragg reflections of an impurity phase can be seen.

Assuming that these impurity phase origins from oxygen deficit for a further YTiO$_3$ crystal, HR71, the oxygen content of the feeding bar was raised to a nominal value of YTiO$_{2.99}$. Then the crystal growth was done under the same conditions. The obtained crystal, HR71, exhibits also impurities what can be seen in the diffractogram of a part of this crystal in figure 3.32.

### 3.8.1 Structural Phase Width and Oxygen Content

Compared with the crystal HR70, the Bragg pattern of the impurity phase is totally different, what means that in the crystal HR71 is a different impurity phase and hence this should arise from excess oxygen now, because only the oxygen content was changed.
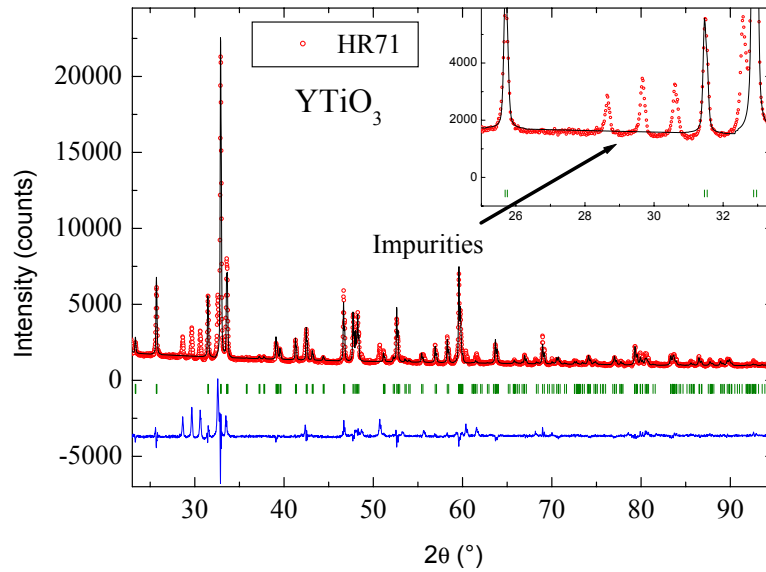


**Figure 3.32:** Also the powder diffractogram of the crystal HR71 contains peaks from an impurity phase which differ from these in the crystal HR70.

The lattice parameters of these two crystals are tabulated in table 3.8.1. Especially the lattice constant $b$ of the crystal HR71 is a bit smaller than

| Sample | $a$ (Å) | $b$ (Å) | $c$ (Å) |
|--------|---------|---------|---------|
| HR70-8 | 5.336 | 5.689 | 7.616 |
| HR71-3 | 5.336 | 5.682 | 7.617 |

**Table 3.12:** Lattice parameters of the $YTiO_{3\pm\delta}$ crystals HR70 and HR71.

the one of the crystal HR70 what is a good indication of a higher oxidation level of the titanium, what means here a higher oxygen content. So, in

comparison to the $LaTiO_{3\pm\delta}$ system, in $YTiO_{3\pm\delta}$ the range of phase purity is very small manifested in the small differences of the lattice parameters of the phase boundaries $YTiO_{3-\delta}$ and $YTiO_{3+\delta}$. An estimation of the $Ti^{4+}$ content of different $YTiO_3$ samples via XAS [96] shows, that a sample with lattice parameters comparable to the crystal HR70 (HR168-2 listed in table 3.8.1) contains no $Ti^{4+}$. On the other hand a sample with lattice parameters in between the two phase boundaries (HR158-4 also listed in table 3.8.1) contains $< 2\%$ $Ti^{4+}$. Hence the range of homogeneity reaches only up to $\approx YTiO_{3.02}$. Therefore phase purity of an obtained $YTiO_3$ crystal means



**Figure 3.33:** Parts of the $YTiO_3$ crystals HR167 (left) and HR168 (right).

high stoichiometry of the crystals and is satisfactory for most experiments[7]. For the next crystal growths, HR82 and HR158, the oxygen content of the starting material was raised up to a value of 2.97.

The powder diffractogram of the obtained crystals shows no impurities what can be seen for example at the diffractogram of the crystal HR82 in figure 3.34. So the oxygen content is quite acceptable. For later crystals growths, HR167 and HR168, the oxygen content was further optimized with a starting composition of $YTiO_{2.96}$. These crystals are shown in picture 3.33. They exhibit nearly perfect stoichiometry, what can be seen by means of the lattice parameters, and was also probed by XAS experiments [96] for the crystal HR168, where only $Ti^{3+}$ was detected.

---

[7]The character of the electrons in $YTiO_3$ is much more local than in $LaTiO_3$ hence deviations from stoichiometry have considerably smaller influence.
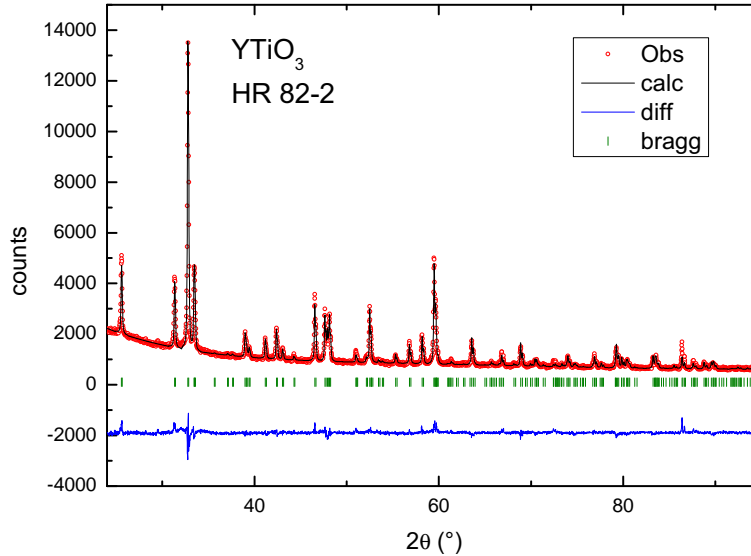
**Figure 3.34:** XPD pattern of the sample HR82-2. No impurities are detectable.

The lattice parameters of all the grown YTiO$_3$ crystals together with literature data [18, 58] are shown in table 3.8.1. Also the ferromagnetic transition temperature of the crystals was probed by magnetization measurements. These show a transition into an ferromagnetic state with a Curie temperature $T_c \approx 30\,\mathrm{K}$ in good agreement with literature [18,58]. This can be seen exemplarily in figure 3.35, where the magnetization curve of the sample HR158, recorded by Nils Hollmann is shown [97].

**Single Crystallinity**

At all the grown YTiO$_3$ crystals single crystallinity was proved via a comparison of Laue photography of the upper and lower surface. This is shown for the crystal HR82 in figure 3.36, indicating that the domains at the observed surfaces have at least the same orientation. Additionally polarization

| Sample | $a$ (Å) | $b$ (Å) | $c$ (Å) |
|---|---|---|---|
| HR82-2 | 5.339 | 5.687 | 7.618 |
| HR82-4 | 5.338 | 5.682 | 7.619 |
| HR158-2 | 5.339 | 5.690 | 7.615 |
| HR158-4 | 5.337 | 5.685 | 7.617 |
| HR167-2 | 5.337 | 5.690 | 7.613 |
| HR167-4 | 5.337 | 5.689 | 7.614 |
| HR168-2 | 5.336 | 5.689 | 7.612 |
| [18] | 5.336 | 5.679 | 7.611 |
| [58] | 5.335 | 5.689 | 7.609 |

**Table 3.13:** Lattice parameters of the $YTiO_3$ crystals.

microscopy on polished surfaces of the crystals was done. For example the result for the crystal HR158 is presented in picture 3.37. No twinning pattern like in the $LaTiO_3$ (figure 3.26) crystals but a homogeneous surface
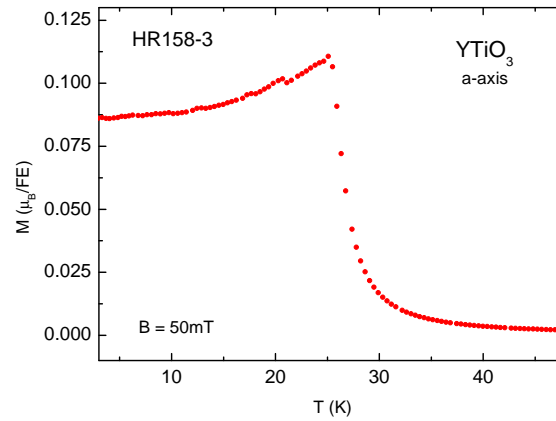


**Figure 3.35:** Magnetization curve of the $YTiO_3$ crystal HR158 along the "hard" axis taken from [97].
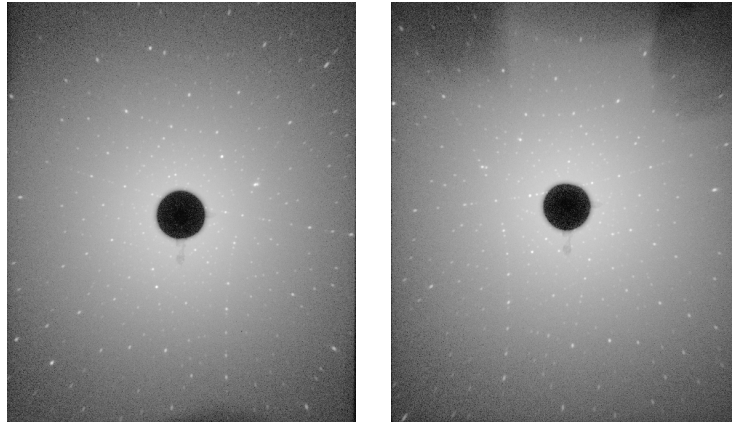
**Figure 3.36:** The Laue pattern of the top and bottom side of a YTiO$_3$ crystal indicating single crystallinity.

can be seen. Hence there is strong evidence that the grown YTiO$_3$ crystals are real single crystals.
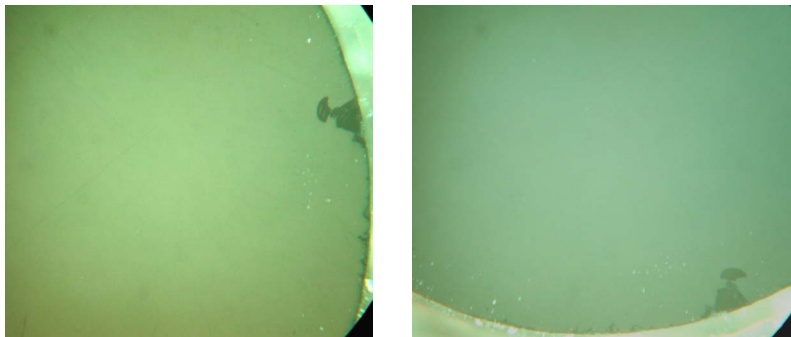


**Figure 3.37:** A polished surface of a YTiO$_3$ crystal observed by polarization microscopy. the surface looks homogeneous and especially exhibits no stripe-like pattern like in the LaTiO$_3$ crystals in figure 3.26. The color of the whole surface is changing when turning the sample indicating single crystallinity.

### 3.8.2 $Y_{1-x}Ca_xTiO_3$

In the $Y_{1-x}Ca_xTiO_3$ system occurs a metal to insulator transition at a doping level of $\approx 40\%$ [98, 99]. The origin of this transition is not well understood and still under debate. To observe especially the structural aspects of this transition [87,88], crystals of this system should be grown [94]. A first crystal with a doping level of $25\%$ Ca content was grown under the same conditions like the $YTiO_3$ crystal, HR82, even with the same oxygen content of the feeding rod: $Y_{0.75}Ca_{0.25}TiO_{2.97}$. The XPD pattern of this crystal, HR74, is shown in figure 3.38. It exhibits Bragg reflections of an
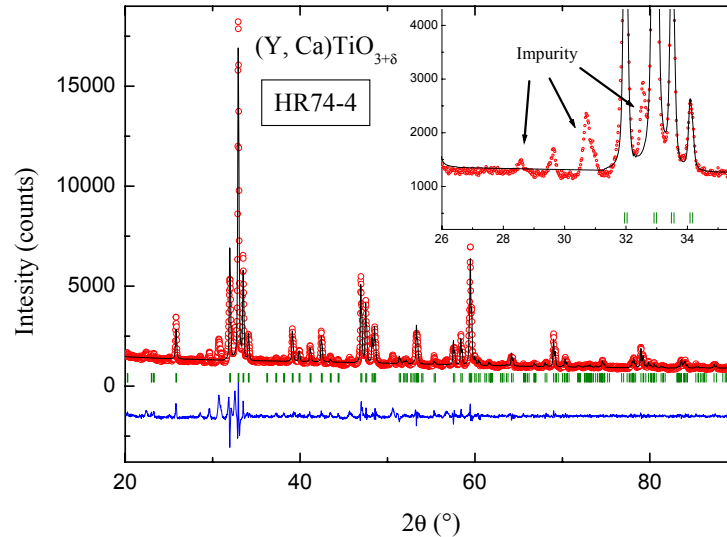


**Figure 3.38:** The Bragg pattern of the crystal HR74 containing impurities of a higher oxidized phase.

impurity phase, indicating that the Oxygen content is to high.

Hence the raising of the melting point with increasing Ca- doping seems to be connected with a stronger oxidizing effect. Therefore the oxygen content of the feeding rod was lowered to a value of $(Y, Ca)TiO_{2.96}$ for the growth of the crystal HR99. The diffractogram of this crystal is containing no reflections of an impurity phase (see figure 3.39).

Structural investigations of Ca doped samples (especially which exhibit impurities of oxygen excess) and TGA measurements [100] indicate that the region of homogeneity in the $(Y, Ca)TiO_3$ system is at least as narrow as in

the undoped YTiO$_3$, what is in good agreement with general expectation [53]. So this crystal HR99 has a well defined oxygen content.
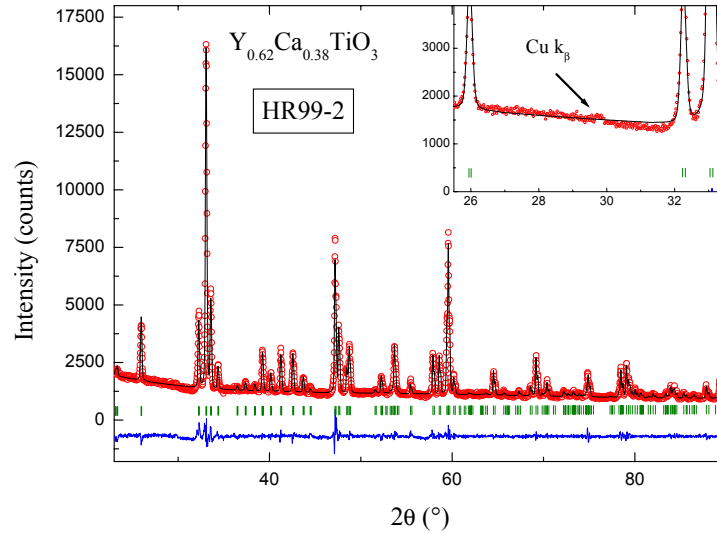


**Figure 3.39:** X-ray diffractogram of the crystal HR99 indicating phase purity.

But in contrast to the pure YTiO$_3$, where all the crystals of pure phase, were obtained as compact single crystals, the crystal HR99 is not homogeneous and cracks very easily see picture 3.40. This scenario was interpreted as an additional indicator for excess oxygen in the small deviation area around $\delta \approx 0.01$. So, to optimize the stoichiometry in further crystal growths the Oxygen content was lowered again to a value of $(Y, Ca)TiO_{2.945}$. Such a crystal, HR141, is also shown in picture 3.40 its surface is homogeneous and shiny. The Oxygen content was determined by TGA to a value of $Y_{0.59}Ca_{0.41}TiO_{3.003}$ indicating excellent stoichiometry.

The determined lattice parameters of this series are shown in figure 3.41.

**Susceptibility**

Even with magnetization measurements are the occurring phase transitions observable, what can be seen in figure 3.42, where the susceptibility $\chi(T)$ of this doping series is shown. The samples with a Ca content of 41, 50,

**Figure 3.40:** Parts of the crystals HR99 and HR141. The crystal HR99 exhibits a lot of cracks and splits very easily, while the crystal HR141 is a compact single crystal as an result of an optimized oxygen content.

and 55 % were measured by Nils Hollmann see [97]. The 38% doped sample exhibits a hysteresis indicating a first order transition at $\approx 120\,\mathrm{K}$. This tran-
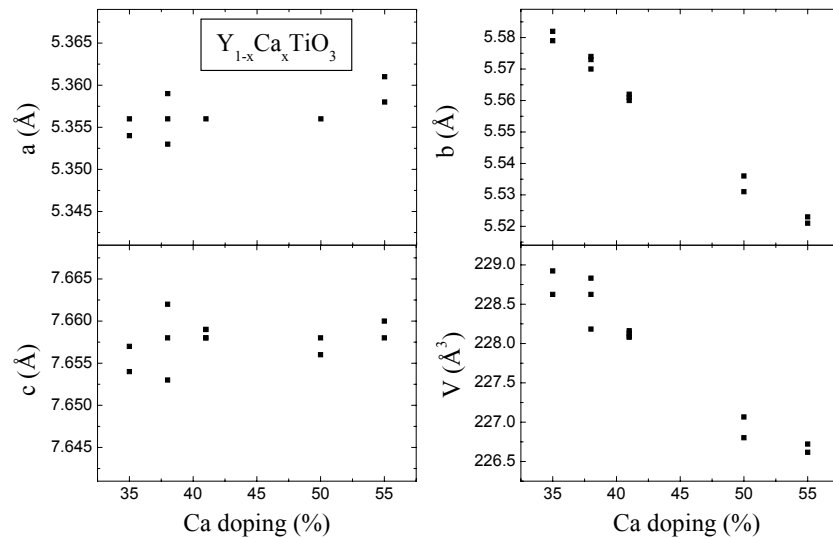


**Figure 3.41:** Lattice parameters of the doping series $\mathrm{Y}_{1-x}\mathrm{Ca}_x\mathrm{TiO}_3$.
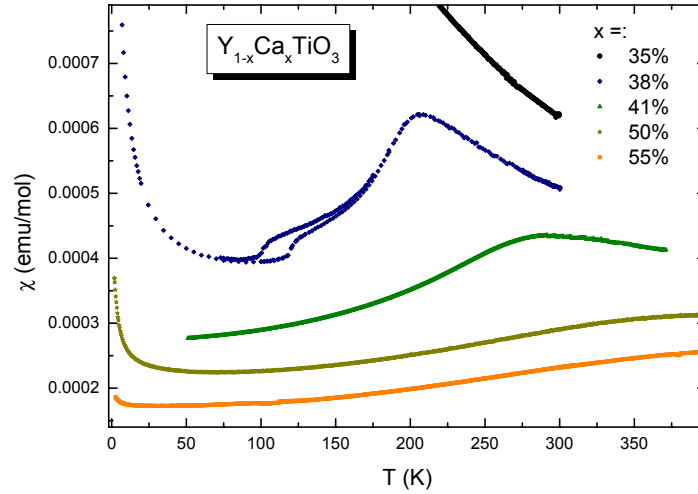
**Figure 3.42:** The susceptibility of the doping series $Y_{1-x}Ca_xTiO_3$ shows a high temperature maximum, which is shifted to higher temperatures with the doping level (up to a value of $\approx 0.55\,\%$). A first order transition occurs in the doping regime around $38\,\%$ Ca content.

sition coincides with a metal to insulator transition [87,99], shown in figure 3.43 and is connected with a structural change. While in the low temperature region a phase separation between an monoclinic and an orthorhombic phase occurs, in the intermediate temperature range only a monoclinic phase is existing [99].

Another feature is a high temperature maximum of the magnetic susceptibility of all the observed samples (except in the 35% doped sample). This maximum shifts systematically to higher temperatures with the doping level and is indicating a magnetic phase transition. This transition is also reported in literature and is connected with a structural phase transition [99] but only for lower doping levels. So as an new aspect we find here that this transition is still existing in an doping regime of $> 50\,\%$. Furthermore here is the transition temperature highest with an maximum of $T^* \approx 400\,K$ at an doping level of $\approx 55\,\%$ Ca doping.
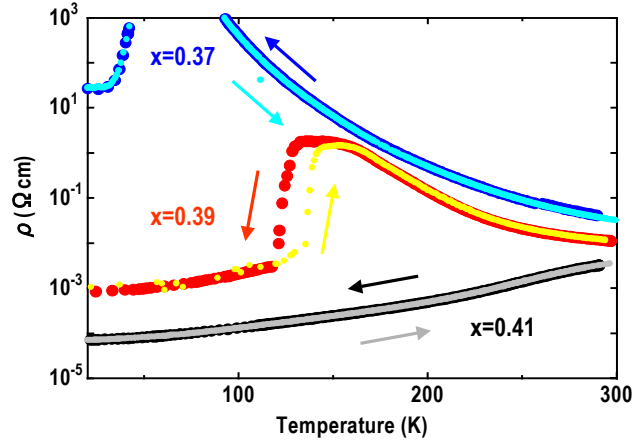
**Figure 3.43:** The resistivity of the $Y_{1-x}Ca_xTiO_3$ series, taken from [99], shows a MIT at $\approx 100\,K$ for the samples with a doping level up to $\approx 40\,\%$.

## 3.9 GdTiO$_3$

For an structural investigation of the $RETiO_3$ series [57,87] a $GdTiO_3$ crystal should be grown [94]. For the growth of the $GdTiO_3$ crystal, HR143, the nominal composition of the starting material was $GdTiO_{2.93}$. The crystal, HR143, was grown in an inert Argon atmosphere with a pressure of 1.8 bar and the growing speed was set to $10\,mm/h$.

Both the upper and the lower shaft were not rotated during the whole growth to avoid any turbulences like discussed in chapter 3.3.2. In comparison with $LaTiO_3$ and $YTiO_3$ the melting zone was more unstable. This effect appeared in all the $RETiO_3$ growths, thus it seems that the much higher specific mass of the RE let the melting zone drop down more easily like described in equation 3.1.

Figure 3.44 shows a part of the so obtained crystal, HR 143. It has a black, shiny look. In the X-Ray powder diffractogram (see figure 3.45) no impurities can be seen. The lattice parameters of the top (HR143-2) and the bottom part (HR143-4) are listed in table 3.9 and have nearly the same values. Hence the crystal is highly homogenous. For an estimation of the oxygen content the lattice parameters were compared with literature data also listed in table 3.9. The lattice parameters are nearly the same as reported in [18, 101].
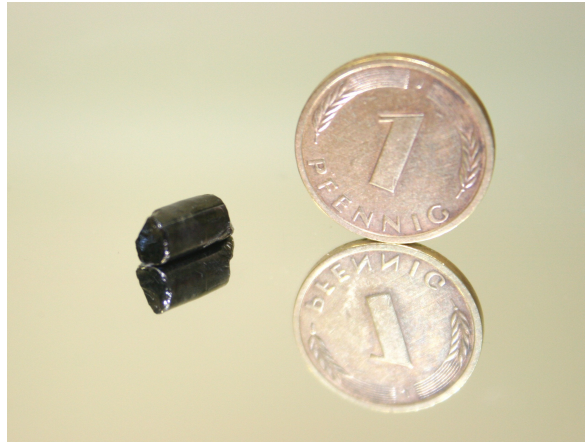
**Figure 3.44:** A part of the $GdTiO_3$ crystal HR143.

Figure 3.46 shows the field cooled magnetization curve M(T) of the sample HR143-2 [97]. The magnetic moment at 4 K is with $M(4\,K) \approx 2.6\,\mu_B/FE$ much to high for a $d^1$ system like the $Ti^{3+}$ ion only. Hence it also results from a $Gd^{3+}$ sublattice magnetization. The transition temperatures of the
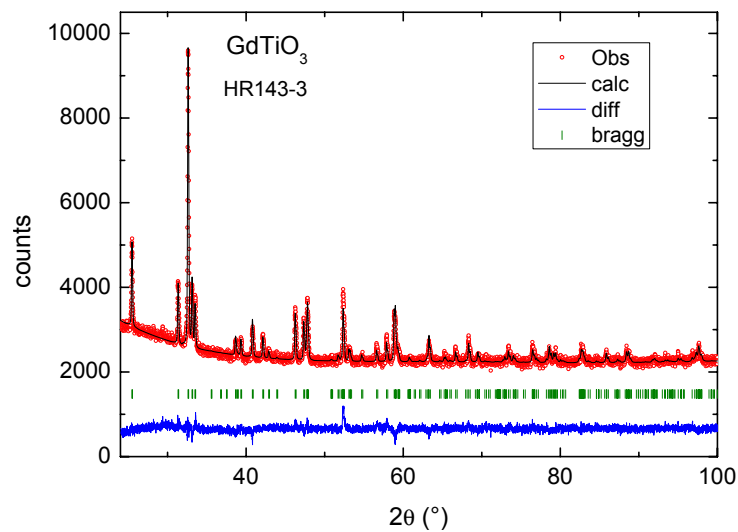


**Figure 3.45:** XPD pattern of the $GdTiO_3$ crystal HR143.

| Sample | $a\,(\text{Å})$ | $b\,(\text{Å})$ | $c\,(\text{Å})$ | $T_c\,(\text{K})$ |
|---|---|---|---|---|
| HR143-2 | 5.402 | 5.700 | 7.672 | 34 |
| HR143-5 | 5.401 | 5.696 | 7.676 | — |
| Ref.: [18] | 5.393 | 5.691 | 7.664 | 31 |
| Ref.: [101] | 5.395 | 5.696 | 7.664 | 32 |

**Table 3.14:** Lattice parameters of $GdTiO_3$.

ferromagnetic order of the two sublattices are close to each other, thus to determine the Curie temperature of the titanium, the inverse susceptibility $\chi^{-1}$ was used (inset of figure 3.46). It shows the transition of the Titanium sublattice at $T_c \approx 34\,\text{K}$, what is quite high in comparison with literature (see table 3.9). The high Curie temperature together with slightly greater lattice parameters than reported in literature indicate very high stoichiometry of the $GdTiO_3$ crystal HR143.
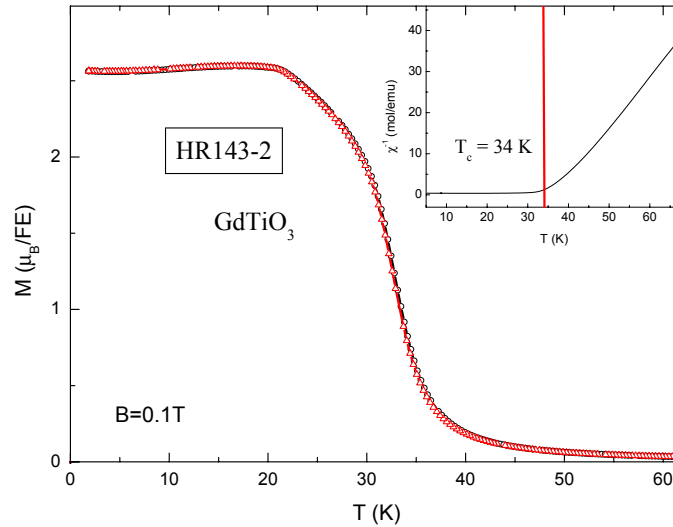


**Figure 3.46:** Magnetization $M(T)$ and inverse susceptibility $\chi^{-1}$ of $GdTiO_3$ from [97].

### 3.9.1 Single Crystallinity

Single crystallinity was checked by Laue photography and polarization microscopy. The Laue pictures of the top and bottom part of this crystal can be seen in figure 3.47, indicating that these two surfaces have the same orientation. A polished surface was observed by polarization microscopy and
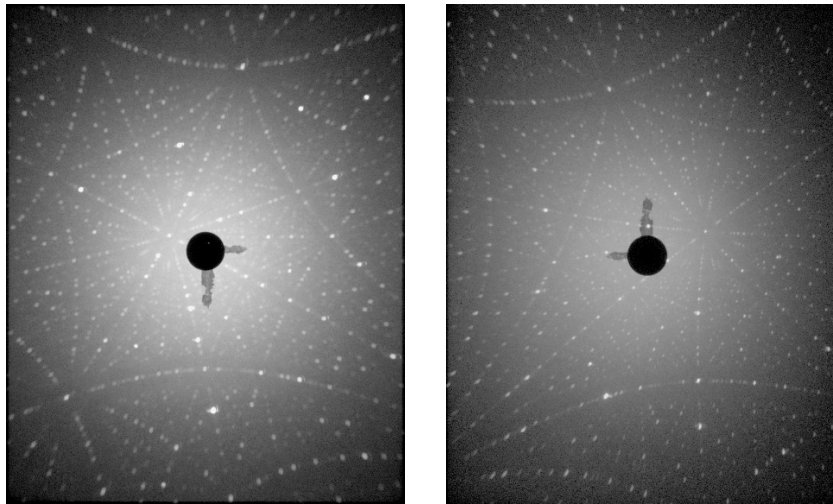


**Figure 3.47:** Laue pictures of the top and bottom side of the GdTiO$_3$ crystal HR143.

is illustrated in picture 3.48. Only a homogeneous surface can be seen which is changing the colour by turning the crystal. Hence the obtained GdTiO$_3$ crystal, HR143 should be an untwinned single crystal.

## 3.10   SmTiO$_3$

A mixture of Ti, TiO$_2$, and Sm$_2$O$_3$ powders of a nominal composition of SmTiO$_{2.92}$ was chosen for the feeding bar. Under an argon atmosphere of 1.8 bar with a growing speed of 9 mm/h was the crystal HR160 grown. Neither the upper nor the lower shaft were rotated (see chapter 3.3.2), like for the GdTiO$_3$ crystal growth, too. X-ray powder diffraction was done at samples of the upper and lower part of the crystal (see figure 3.49), and no impurities were detectable. The determined lattice parameters of the top
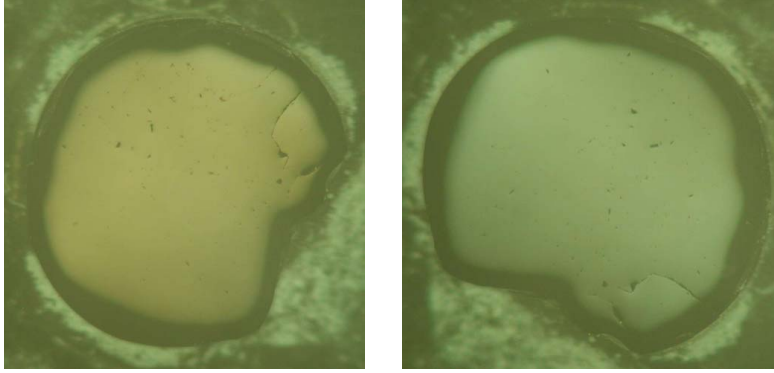
**Figure 3.48:** Photos of a polished surface of the crystal HR143 in the polarization microscope. The surface looks homogeneous and is changing its color when it is rotated.

(HR160-2) and bottom (HR160-4) part, which are listed in table 3.10, have nearly the same values, what indicates a high homogeneity.

To check the oxygen content the lattice parameters and the magnetic transition temperature were compared with data taken from literature [102] in table 3.10. The lattice parameters are slightly higher than the reported what indicates a lower oxygen content. To determine the Néel temperature the magnetization was measured and is shown in figure 3.50. A transition into an antiferromagnetic state appears at a temperature $T_N = 54\,\mathrm{K}$, what is quite high in comparison with literature (see table 3.10) indicating high stoichiometry.

| Sample | $a\,(\text{Å})$ | $b\,(\text{Å})$ | $c\,(\text{Å})$ | $T_N\,(\text{K})$ |
|---|---|---|---|---|
| HR160-2 | 5.464 | 5.676 | 7.729 | 54 |
| HR160-5 | 5.465 | 5.677 | 7.728 | — |
| Ref. [102] | 5.448 | 5.652 | 7.708 | 50 |

**Table 3.15:** Lattice parameters and transition temperature $T_N$ of the $\mathrm{Sm\,Ti O_3}$ crystal HR160 in comparison with literature.
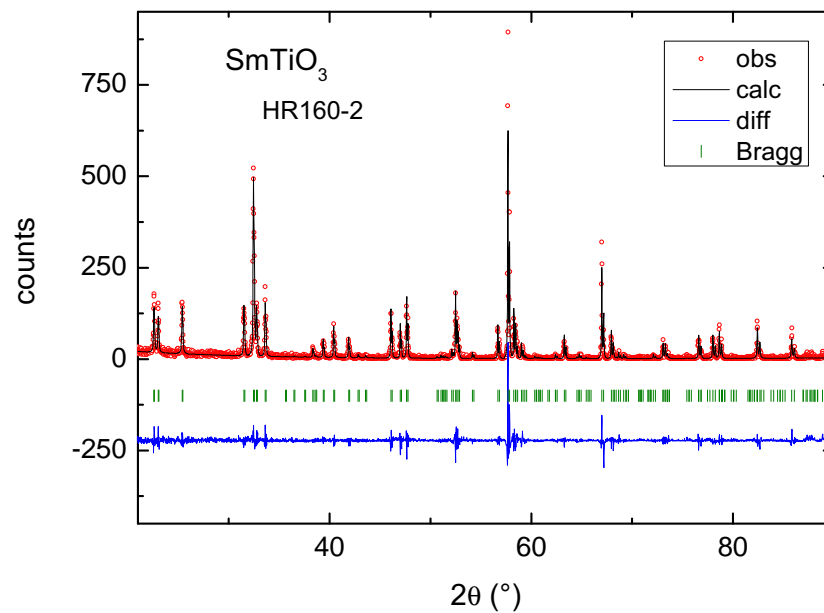
**Figure 3.49:** Powder pattern of the sample HR160-2 (top side) indicating phase purity.

### 3.10.1 Single Crystallinity

Laue pictures of the top and bottom side of the crystal HR160 were taken, see figure 3.51. They indicate that the domains of the observed surfaces have the same orientation. Additionally a cut and polished surface of the crystal was checked by polarization microscopy. The whole surface looks homogeneous what can be seen in picture 3.52. A change of the color was also detectable when rotating the sample. Hence the obtained SmTiO$_3$ crystal HR160 should be an untwinned single crystal.
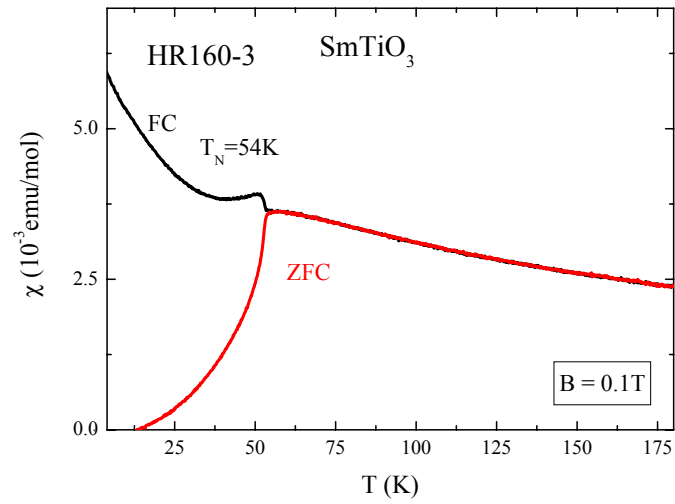
**Figure 3.50:** Field cooled and zero field cooled magnetization measurements of the $SmTiO_3$ sample HR160-3 from [97].
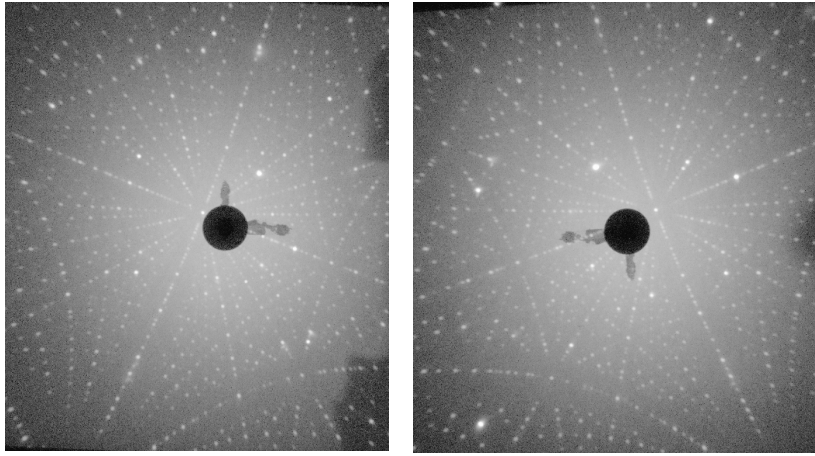
**Figure 3.51:** Obtained Laue pattern of the top and bottom side of the SmTiO$_3$ crystal HR160.
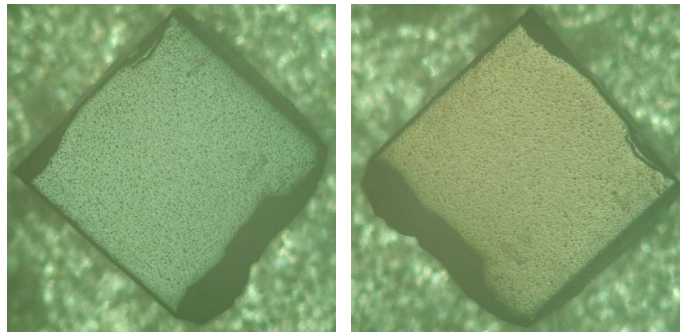


**Figure 3.52:** Photos of the SmTiO$_3$ crystal HR160 in the polarization microscope with different sample orientations.

## 3.11 NdTiO$_3$

For the NdTiO$_3$ crystal HR161 the composition of the starting material was NdTiO$_{2.91}$. An inert atmosphere of argon with a pressure of 1.8 bar was chosen for the growth. Shaft rotation was set to zero for both shafts like mentioned in chapter 3.3.2. The NdTiO$_3$ was pulled with a speed of 9 mm/h, while the upper shaft was not moved.

The X-ray diffractogram of this crystal shows no impurities as can be seen in figure 3.53. In table 3.11 the lattice parameters of the upper (HR161-2) and
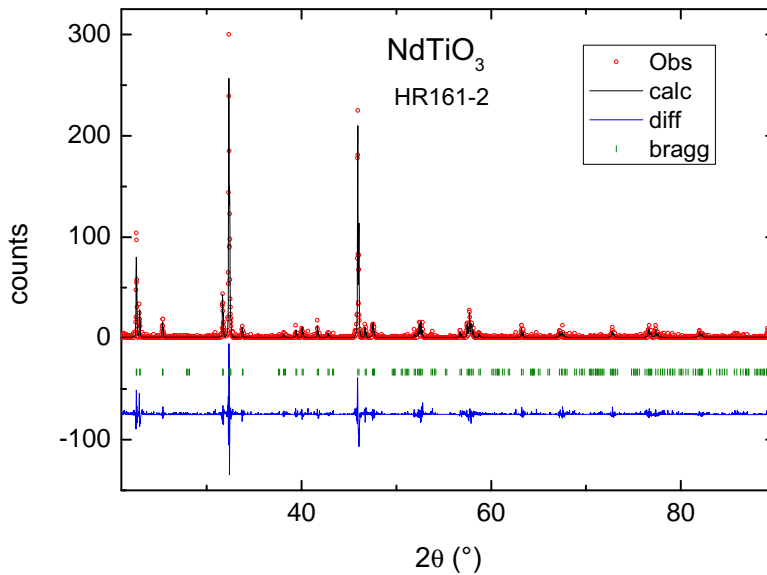


**Figure 3.53:** Powder diffractogram of the crystal HR161.

lower part (HR161-4) of this crystal are listed. The differences between top and bottom side are quite small, indicating high homogeneity of the crystal HR161. In comparison with literature, also listed in table 3.11, the lattice parameters of this crystal are a bit larger what indicates a lower oxygen content. The antiferromagnetic transition temperature $T_N$ was determined

| Sample | $a$ (Å) | $b$ (Å) | $c$ (Å) | $T_N$ (K) |
|:---:|:---:|:---:|:---:|:---:|
| HR161-2 | 5.545 | 5.655 | 7.788 | 94 |
| HR161-3 | 5.543 | 5.652 | 7.783 | — |
| Ref.: [?] | 5.495 | 5.589 | 7.779 | — |
| Ref.: [103] | 5.519 | 5.647 | 7.785 | 90 |

**Table 3.16:** Lattice parameters of NdTiO$_3$.

by magnetization measurements done by Nils Hollmann [97] and is shown in figure 3.54. The anomaly in the inverse susceptibility, $\chi^{-1}$ (shown in the
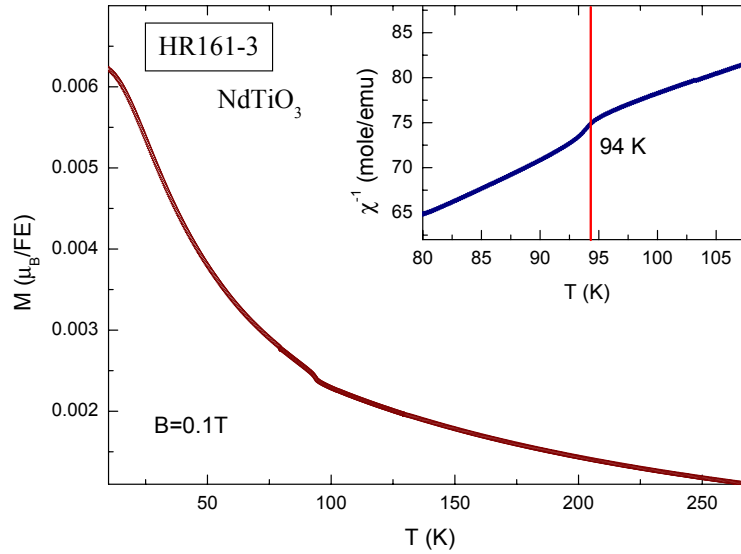


**Figure 3.54:** Magnetization $M$ and inverse susceptibility, $\chi^{-1}$, of the crystal HR161, recorded by Nils Hollmann [97].

inset) coincide with the antiferromagnetic order temperature $T_N = 94\,$K of this crystal what is quite high in comparison with literature, indicating an excellent stoichiometry of the obtained NdTiO$_3$ crystal HR161.

### 3.11.1   Single Crystallinity

Determination of single crystallinity was done by Laue photography and polarization microscopy. Laue pictures of the top and bottom side are shown in figure 3.55 indicating that the domains on these surfaces have the same orientation. In polarization microscopy the most part of a polished surface
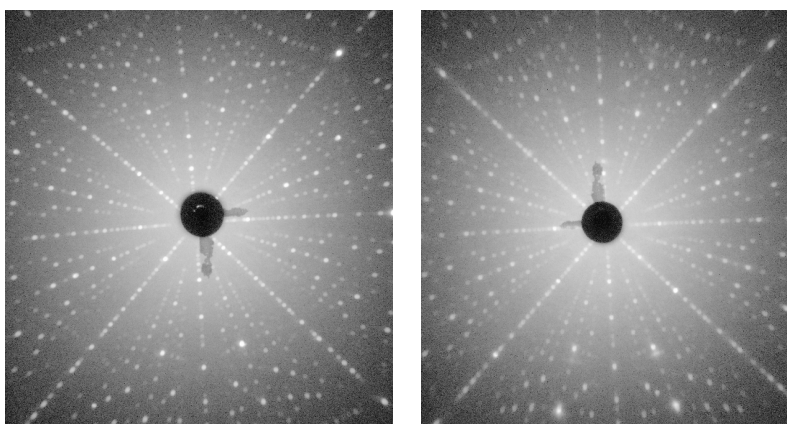


**Figure 3.55:** Laue pattern of the top and bottom side of the crystal HR161.

looks homogeneous with exception of two small stripes.

The bigger one of them can be seen in the pictures 3.56. This means that nearly the whole crystal HR161 is untwinned.
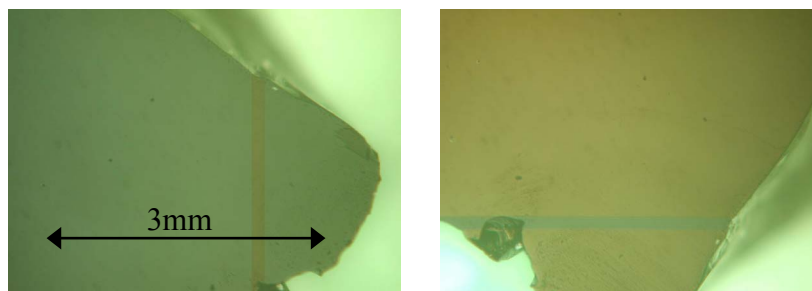


**Figure 3.56:** A part of the $NdTiO_3$ crystal HR161 in the polarization microscope. With exception of two small stripes the whole crystal looks like a monodomain crystal. The bigger one of these two stripes is shown here.

## 3.12  $V_{1-x}Cr_xO_2$

A typical way to grow $VO_2$ crystals is chemical transport and such grown crystals exhibit excellent quality [78]. But the size of the chromium doped crystals obtained with this technique is with less than 1 mm edge length to small for most experimental techniques. So the aim was to get chromium doped crystals in a size big enough for investigations via XAS and PES. For this project floating zone technique was proposed to be the adequate method to obtain bigger samples.
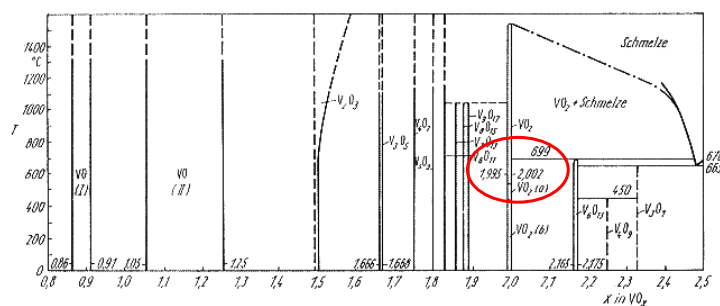


**Figure 3.57:** $VO_x$ phase diagram from [78]. The range of homogeneity of the $VO_2$ phase is quite small. It reaches only from $VO_{1.995}$ up to $VO_{2.002}$ what means less than 1% deviation from the 4+ valence of the Vanadium ions.

The problem of floating zone pulling of this system is the control of the Vanadium valence. A look at the phase diagram in figure 3.57, taken from [78], shows that the region of homogeneity of $VO_2$ is with $VO_{1.995}$ – $VO_{2.002}$ very narrow, and therefore very hard to hit by floating zone technique [104]. On the other hand such a small phase width means that characterisation of the oxygen content can be easily done by XPD. Because phase purity of the grown $VO_2$ crystals means practically no deviation of the vanadium valence.

For a first crystal growth of undoped $VO_2$ a nominal composition of $VO_{1.9}$ was chosen for the feeding bar in expectation of a slightly oxidation due to evaporation during the growth like in the titanates, too. As growing atmosphere argon with 1.8 bar overpressure was used. Because of the melting zone being very unstable neither the upper nor the lower shaft were rotated to avoid any turbulences in the melt. The growing speed was set to 5 mm/h

while the upper shaft was not moved. In this way a first $VO_2$ crystal, HR135, with a length of 5 cm could be obtained.
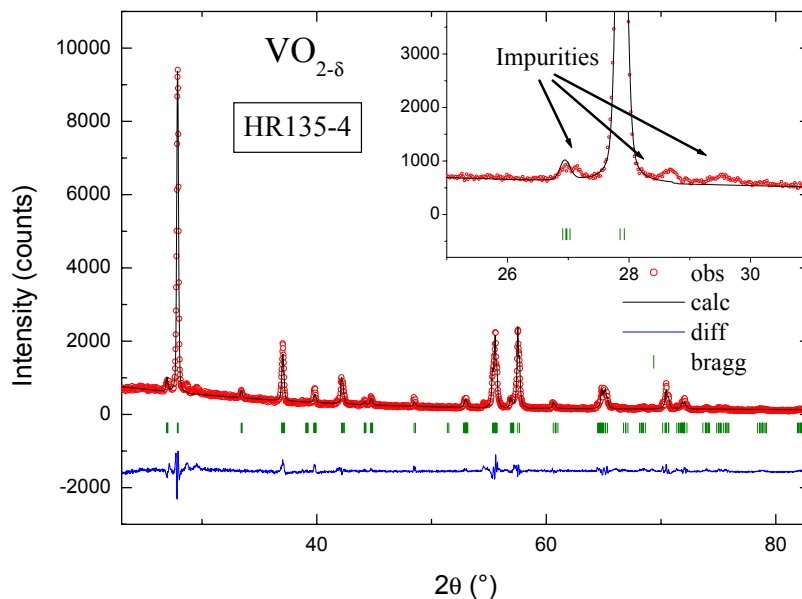


**Figure 3.58:** In the powder diffractogram of the first grown $VO_2$ crystal in this thesis Bragg peaks of an impurity phase are visible indicating off stoichiometry.

Figure 3.58 shows the XPD pattern of this crystal. In the inset Bragg peaks of an impurity phase can be seen indicating off stoichiometry. Additionally the oxygen content was determined by TGA to a value $VO_{1.95}$ which is 0.05 to low. Thus in the next crystal growths the oxygen content of the starting composition was raised step by step until the growth of the crystal HR138. In the diffractogram of the top side of this crystal no impurities are observable shown in figure 3.59 indicating the right oxygen content. But the bottom side habits impurities detected by X-ray diffraction in figure 3.60. This scenario is indicating an oxygen gradient due to the crystal growth like in the $LaTiO_3$ system, too. To balance the oxygen content in further crystal growths an Oxygen gradient of $\Delta\delta = 0.005$ along the feeding bar was chosen. Neither in the top (figure 3.61) nor in the bottom part (figure 3.62) of the such obtained crystal, HR151, impurities were found. Hence the
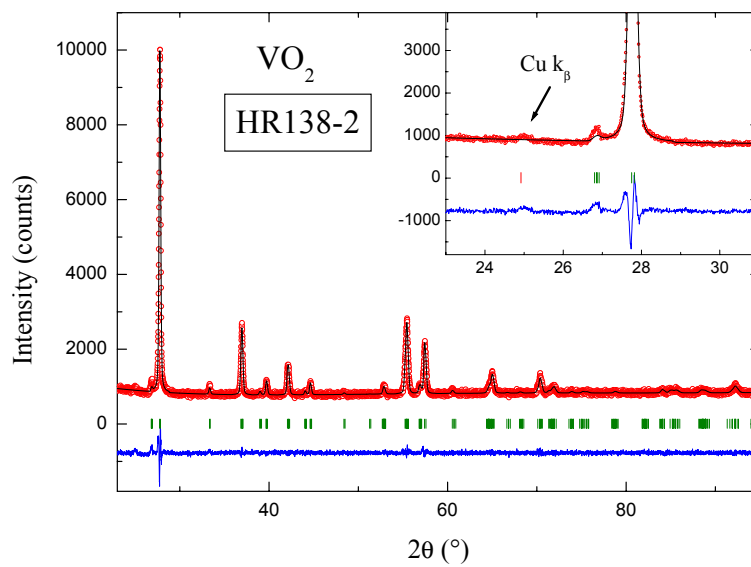
**Figure 3.59:** In the powder diffractogram of the upper part of the $VO_2$ crystal HR138 no reflections of an impurity phase can be seen.

crystal HR151 is highly homogeneous and has a well defined oxygen content. Parts of the so grown crystal are shown in picture 3.63.
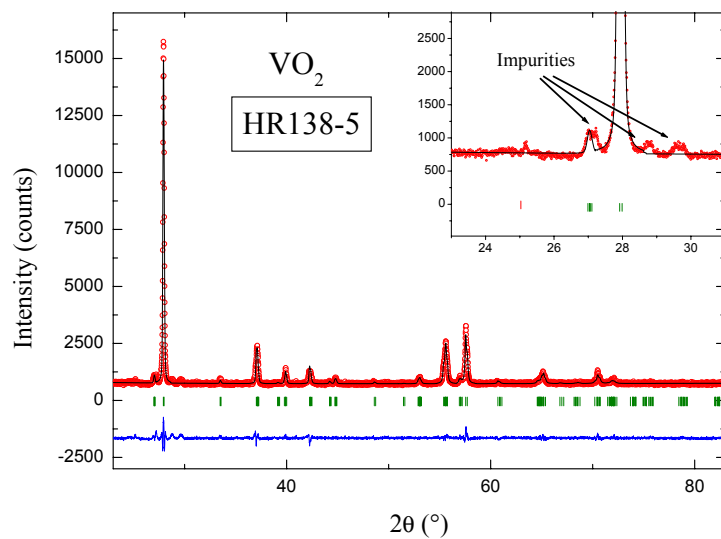
**Figure 3.60:** The lower part of the crystal HR138 habits impurities caused by off stoichiometry which could be observed by XPD.
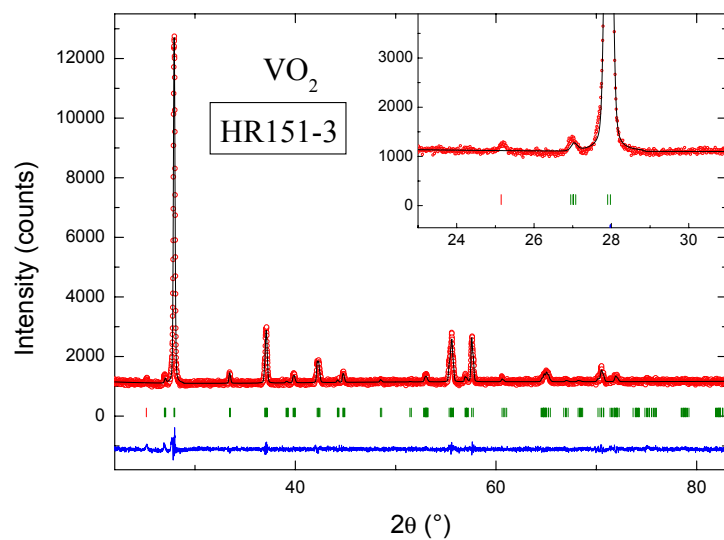


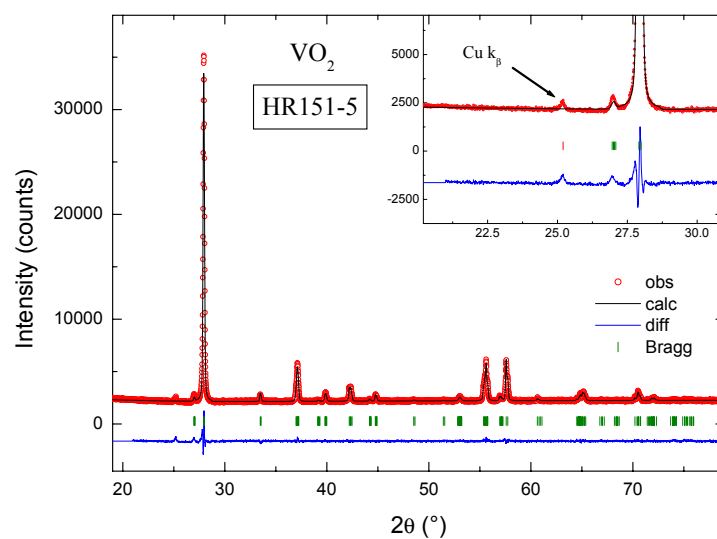**Figure 3.61:** X-ray diffractogram of the sample HR151-3 indicating phase pureness.

**Figure 3.62:** The powder diffractogram of the $VO_2$ crystal HR151-5. No Bragg peaks of any impurity phase can be seen.
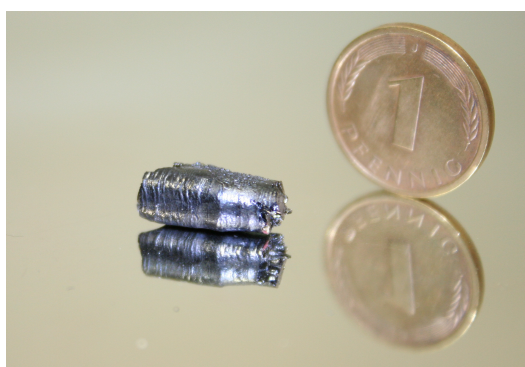


**Figure 3.63:** The $VO_2$ crystal HR151 obtained by floating zone technique.

### 3.12.1 Chromium Doping

Under the same conditions like for the crystal HR151, growths of $1\%$ and $2\%$ chromium doped crystals were done. Also in these crystals (HR152 with
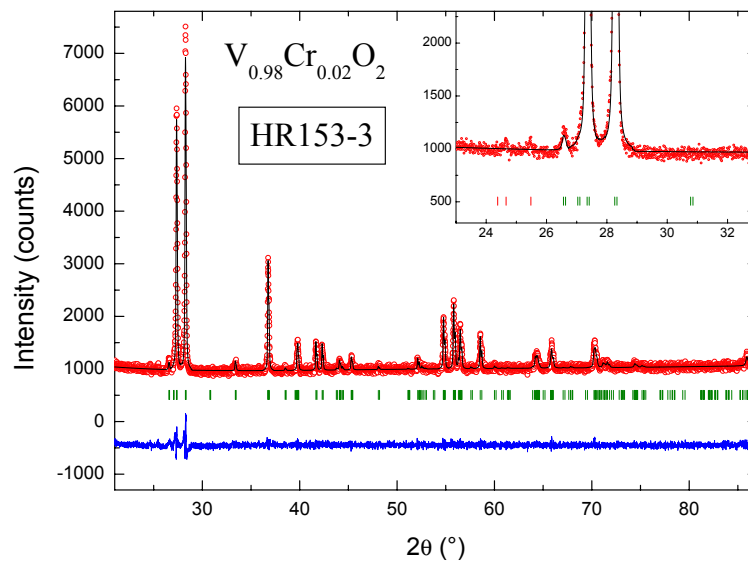


**Figure 3.64:** Powder pattern of the Cr doped $VO_2$ crystal HR153-3. No Bragg peaks of any impurity phase can be seen.

$1\%$ and HR153 with $2\%$ Cr) no impurities could be detected, what can be seen for example in the XPD pattern of the $V_{0.98}Cr_{0.02}O_2$ crystal, HR153, shown in figure 3.64. $VO_2$. But these crystals crack very easily in small pieces. Fortunately some of them are big enough for XAS measurements.

To determine the temperature of the the structural phase transitions the susceptibility $\chi(T)$ was measured by Nils Hollmann [97] and is shown in figure 3.65. The first transition from a rhombohedral high temperature phase to an intermediate monoclinic phase occurs at a transition temperature $T_{RM1} \approx 340\,\mathrm{K}$. The second transition from the monoclinic $M1$ phase to a second monoclinic phase $M2$ happens at a temperature $T_{M1M2} \approx 285\,\mathrm{K}$.
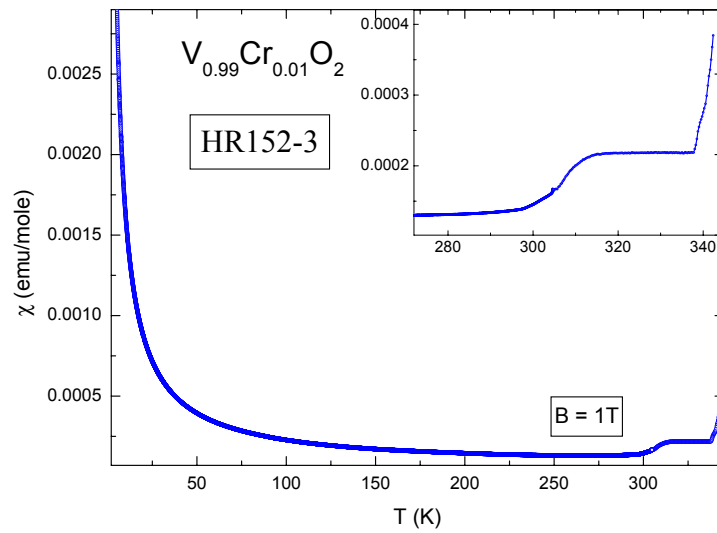
**Figure 3.65:** $\chi(T)$ of the 1% Cr doped $VO_2$ crystal HR152 from [97] indicating two phase transitions, one at $\approx 310\,K$ and the other at $\approx 335\,K$.

### 3.12.2 Single Crystallinity

Single crystallinity was proved by Laue photography and polarization microscopy. The results are shown in picture 3.66 and 3.67 indicating that the obtained $VO_2$ crystal is a single crystal.
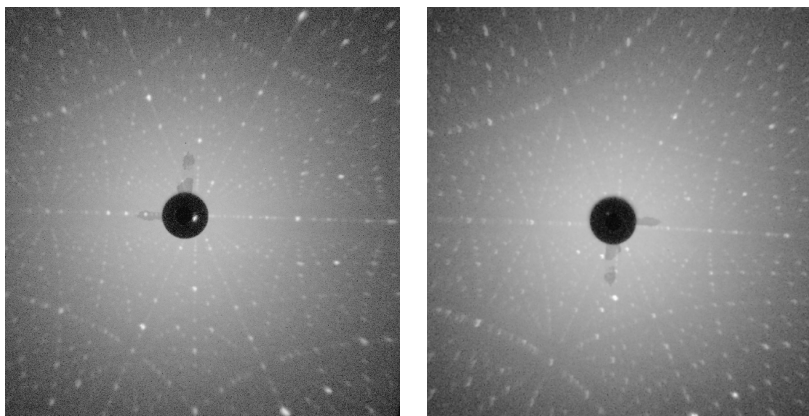
**Figure 3.66:** Single crystallinity of the crystal HR151 observed by Laue photography.



**Figure 3.67:** Polarization microscopy indicating single crystallinity for the $VO_2$ crystal HR151.

# Chapter 4

# Photoelectron Spectroscopy

Photoelectron spectroscopy (PES) is one of the most powerful techniques to determine the electronic structure of materials, and is a standard method in today's solid state research. It is based on the photoelectric effect discovered by Hertz in 1887 and explained by Einstein in 1905 by the quantum nature of light [105]. In a PES experiment, a sample is irradiated by monochromatic light. X-ray photoelectron spectroscopy (XPS) uses x-rays with energies of several hundred eV or keV. In ultra-violet photoelectron spectroscopy (UPS), the light has energies below $100\,\text{eV}$. Typical light sources for UPS are He-discharge lamps with $\hbar\omega = 21.2\,\text{eV}$ (He I) or $\hbar\omega = 40.8\,\text{eV}$ (He II), or x-ray sources using characteristic radiation of Al $K_\alpha$ with $\hbar\omega = 1486.6\,\text{eV}$ or Mg $K\alpha$ with $\hbar\omega = 1253.6\,\text{eV}$ for XPS. Nowadays, synchrotron radiation sources with high intensities and tunable energies are widely used. The photoelectron emission rate is measured as a function of the kinetic energy of the outgoing electrons. Since each element has a unique set of core-level spectra, that is a unique set of binding energies, this technique is also a powerful tool for chemical analysis: XPS is often also called ESCA, electron spectroscopy for chemical analysis.

PES probes excitations from the ground state of the N-particle system to all accessible one-hole final states. That is, electrons are ejected into the vacuum, provided that the excitation energy absorbed is equal to or greater than the energy separation between the bound electron and the vacuum level. In this case, an incoming photon of energy $\hbar\omega$ will excite the system from the initial $N$-electron state with the ground state energy $E_i^N$ into a set of states with one electron in the vacuum, i.e. the photoelectron, and

an $(N-1)$-electron state of the system with the final state energy $E_f^{(N-1)}$. Conservation of energy requires

$$\hbar\omega + E_i^N = E_{\text{kin}} + \phi + E_f^{(N-1)}, \tag{4.1}$$

where $E_{\text{kin}}$ denotes the kinetic energy of the photoelectron after photoemission and $\phi$ the workfunction of the solid. The binding energy $E_{\text{b}}$ of this electron in the solid is defined as

$$E_{\text{b}} = E_f^{(N-1)} - E_i^N \tag{4.2}$$

Note that $E_{\text{b}}$ is defined with respect to the chemical potential $\mu$ or $E_{\text{F}}$ of the solid, whereas $E_{\text{kin}}$ is measured with respect to the vacuum level $E_{\text{vac}}$ as sketched in figure 4.1. The kinetic energy of a photoelectron can now be written as

$$E_{\text{kin}} = \hbar\omega - E_{\text{b}} - \phi, \tag{4.3}$$

Here, it is assumed that during a photoemission process, no interactions occur between the emitted electron and the remaining (N-1) particles, that means, the electronic system is frozen and does not rearrange while the photoelectron is escaping the solid. This assumption is referred to as the *sudden approximation*. In a simplified one-electron picture, PES probes the "occupied" density of states by analyzing the photoelectron emission rate as a function of the kinetic energy. This is shown schematically in figure 4.1. The measured spectra consist of well-defined core level peaks and valence bands due to electrons that leave the surface without prior energy loss, as well as a continuous background that arises from electrons which undergo random inelastic scattering processes while travelling through the solid. The peak width is a convolution of a broadening due to lifetime and instrumental resolution (energy width of the incident radiation and resolution of the electron energy analyzer).

PES is a powerful tool to unravel the basic electronic structure of strongly correlated materials since use can be made of the extremely large dynamic range in energy that this type of spectroscopy can cover. By studying excitation spectra in the energy range from several eV up to several hundreds of eV's, one can obtain direct information about the 'bare' electrons, e.g. the charge, spin, and orbital state of the ions that make up the correlated material. By measuring the excitation spectra with ultra-high resolution in the meV range from the chemical potential, one can find directly the
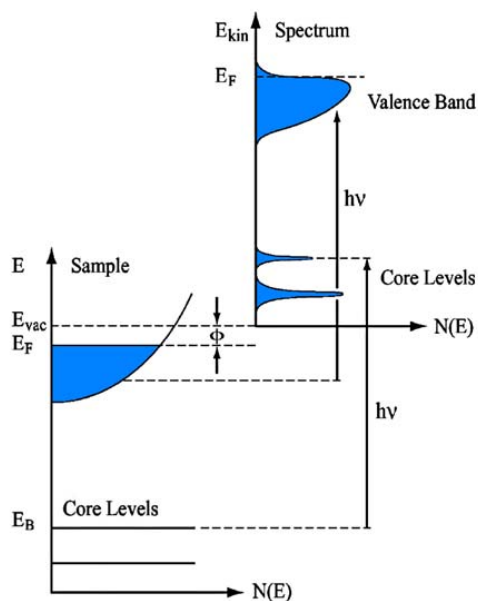
**Figure 4.1:** Energy level diagram of a PES experiment in a one-electron picture [106]. Left: The schematic density of states of a metallic sample consisting of several sharp core levels and a broad valence band which is filled up to the Fermi level $E_\mathrm{F}$. Right: The corresponding spectrum generated by PES.

momentum dependent behavior of the 'dressed' electrons, e.g. quasi particles. Here we would like to note that it is not the excitation energy that determines whether the measurement probes the high or low energy scale physics. Instead, it is the resolution with which the measurement is carried out, since this determines the quality of the observed features, and thus of the measured low energy scale phenomena if the measurement is focused on the region near the chemical potential.

## 4.1 Theoretical Concept

The observed intensity in a PES experiment is given by the transition probability of the photoemission process within Fermi's Golden Rule,

$$W_{IS,FS}^{\text{PES}} \propto |\langle FS_N|\mathcal{O}^{\text{PES}}|IS_N^0\rangle|^2 \delta\left(E_N^{FS} - E_N^0 - h\nu\right). \tag{4.4}$$

Here, $|IS_N^0\rangle$ represents the initial state, which is the ground state of the system with energy $E_N^0$. $|FS_N\rangle$ refers to a $N$–particle final state with energy $E_N^{FS}$, a product state of both the remaining $(N-1)$ particle system and the photoelectron. The photoemission operator $\mathcal{O}^{\text{PES}}$ can be identified with the electromagnetic dipole interaction, $-e\hat{\mathbf{r}}$, with the unit charge $e$, and takes in second quantization the form

$$\mathcal{O}^{\text{PES}} = \sum_{k,i} M_{k,i} \varepsilon_k^\dagger c_i, \tag{4.5}$$

composed of the optical matrix elements $M_{k,i} = \langle k|\mathcal{O}^{\text{PES}}|i\rangle$, the creation operators $\varepsilon_k^\dagger$ of a photoelectron with momentum $k$, and the annihilation operators $c_i$ of a bound electron in the one–particle state $|i\rangle$. In the sudden approximation, the $N$-particle final states are given by

$$|FS_N(k,j)\rangle = \hat{a}|k\rangle|FS_{N-1}(j)\rangle, \tag{4.6}$$

where $\hat{a}$ is the anti–symmetrization operator, $|k\rangle$ represents the photoelectron with momentum $k$ and energy $E_k$, and $|FS_{N-1}(j)\rangle$ denotes the eigenstates of the $(N-1)$–electron system with quantum numbers $j$ and energies $E_{N-1}^{FS}(j)$. In order to evaluate the matrix element in (4.4), we also express the initial state as an anti–symmetrized product of a one–particle state, which is annihilated in the photoemission process, and a $(N-1)$ particle state,

$$|IS_N^0\rangle = \hat{a}|i\rangle|IS_{N-1}(i)\rangle = c_i^\dagger|IS_{N-1}(i)\rangle, \tag{4.7}$$

in which $|IS_{N-1}(i)\rangle$ does not need to be the ground state or even an eigenstate of the $(N-1)$ electron subsystem. In fact, such a separation of the $N$ electron state does not necessarily have to be meaningful, but we can always find an approximate product state instead. From the representation (4.5) of the photoemission operator in second quantization, we see that it acts on the one–particle states only, and with the $\delta$–function rewritten by use of

$\lim_{\eta \to 0} \mathrm{Im} \frac{1}{x - \mathrm{i}\eta} = \pi\delta(x)$, we find

$$W^{\mathrm{PES}}_{i,(k,j)} \propto \lim_{\eta \to 0} \frac{1}{\pi} \mathrm{Im} \frac{|\langle k|\mathcal{O}^{PES}|i\rangle\langle FS_{N-1}(j)|c_i|IS^0_N\rangle|^2}{E^{FS}_{N-1} + E_k - E^0_N - h\nu - \mathrm{i}\eta}. \tag{4.8}$$

The photoemission spectrum as a function of the photoelectron energy $E_k$ is given by the sum of (4.8) over $i$, corresponding to all possibilities of exciting bound electrons, and over $j$, according to all possible final states fulfilling energy conservation. We can use the completeness relation of the eigenstates of the $(N-1)$ electron system in the sum of (4.8) over $j$, yielding the *photocurrent*

$$I^{\mathrm{PES}}(E_k) \propto \lim_{\eta \to 0} \frac{1}{\pi} \mathrm{Im} \sum_{i,i'} M_{k,i} M_{i',k} \langle IS^0_N | c^\dagger_{i'} \frac{1}{\mathcal{H} + E_k - E^0_N - h\nu - \mathrm{i}\eta} c_i | IS^0_N \rangle. \tag{4.9}$$

We recognize on the right hand side of (4.9) the spectral function $A(E_k)$ in the limit $\eta \to 0$, convoluted with optical matrix elements. The spectral function is given by the imaginary part of the one–*hole* propagator, the Green's function $\mathcal{G}(E_k)$. The photoemission spectrum peaks at photoelectron energies corresponding to poles in (4.8), i.e. at

$$E_k = E^0_N + h\nu - E^{FS}_{N-1}. \tag{4.10}$$

The conceptually simple and elegant description of PES in (4.9) makes it a powerful and appealing experimental tool for the investigation of solid state systems. It is valid for one-particle systems as well as for systems with many-body interactions. In this respect we must stress that the correspondence between the occupied electronic density of states in a one-electron description as sketched in figure 4.1 and the photoemission spectrum of a system is incorrect if electron correlation effects play a role, not only because the concept of occupied one-electron density of states has then already lost its meaning.

## 4.2 Bulk- vs Surface sensitivity

In a PES experiment, the light can penetrate into the solid over a distance of order micrometers and the ionization can take place in this region, whereas the escape depth of the generated photoelectrons is only a few Å. This escape

depth defines the probing depth of the photoemission technique. Figure 4.2 shows the photoelectron escape depth as a function of the electron kinetic energy for various metals. It approximately follows the so-called "universal" curve. As can be seen from the figure, the probing depth of PES is only in the order of some nanometers. This is due to a very short inelastic mean free path of the photoelectrons in the solid which arises from interactions with the lattice and the very strong electron-electron scattering, which in turn depends on the electronic structure of the system. Since PES predominantly samples electrons from only the top few atomic layers, it is a rather surface sensitive technique. One always has to ask to what extent the measured spectrum is representative for the bulk material. We can write the relative
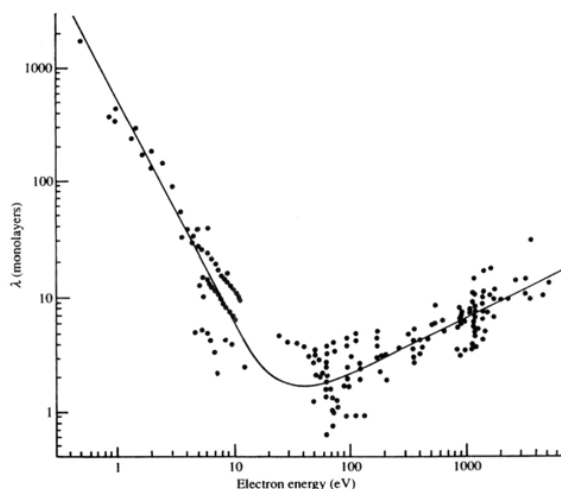


**Figure 4.2:** Approximate photoelectron mean free path as a function of the electron kinetic energy for various metals [107].

number of photoelectrons escaping the sample with distance $z$ from the surface with an inelastic mean free path $\lambda$, as

$$N(z) = N_0 e^{-z/\lambda}. \tag{4.11}$$

The total photoelectron intensity from the volume of the sample probed in the experiment is then given by the integral of $N(z)$ from $z$=-$\infty$ to $z$=0, and is thus proportional to $\lambda$. A geometrical factor has to be included if

the emission direction of the photoelectrons makes an angle with the surface normal (cf. figure 4.3). Important is to keep in mind that according to (4.11) the intensity from the surface layers will be disproportionately higher than from deeper layers, causing the spectra to be even more surface sensitive. As the universal curve in figure 4.2 suggests, the escape depth is maximized by choosing the highest possible photon energy. In conventional soft x–ray photoemission, escape depths of $15 - 20$ Å can be realized with photon energies of a several hundred eV, customarily available in contemporary synchrotron beam lines or conventional x–ray sources, thus providing a reasonable bulk sensitivity in most cases. Note that the validity of the universal curve in the case of correlated systems, especially the increase of the escape depth for photon energies below 10 eV is continuously being questioned, see e.g. [108].

The influence of the emission angle, mentioned above, is illustrated in figure 4.3. With a fixed photon energy, resulting in a constant inelastic mean free path of the photoelectrons, given by the height of the blue hatched area, the contribution from the bulk (green) to the spectrum is maximized for electrons emitted normal to the surface (blue arrow), resulting in the most bulk sensitive geometry. Note that the surface region (yellow) still makes up a significant fraction of the total probing volume (blue hatched). In contrast, electrons emitted under an angle to the surface normal (red arrow), can still travel the same distance through the solid to the surface, however, a substantially larger fraction of the path is in the surface region, which means that a correspondingly smaller number of photoelectrons originates from the bulk region. In other words, while the surface volume is the same as for normal emission, the bulk contribution to the probed volume (red hatched) is noticeably smaller. At an angle of 60° with respect to the surface normal, the effective probing depth is reduced by a factor $1/2$. The issue of surface versus bulk is crucial for photoemission experiments especially on correlated electron systems. It is being realized only in recent years, that the electronic structure of the surface of a material could be quite different from that of the bulk. This is in fact a natural tendency especially for strongly correlated systems, in which the local coordination play a significant role for the electronic structure. Obviously, atoms or ions at the surface have quite different coordination than those in the bulk, with consequences for the crystal field levels, the strength of the hopping integrals and the magnitude of the charge transfer and Coulomb energies.

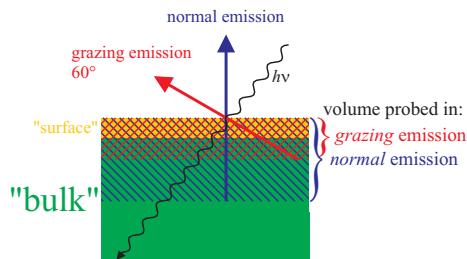Significant differences between surface and bulk electronic structure has

**Figure 4.3:** The probing volume for normal emission (blue hatched) maximizes the contribution of the bulk (green). The contribution of the surface (yellow) is the same in grazing emission (red hatched), but due to the fixed escape depth, the probing depth is reduced by a factor $1/2$ at $60°$.

been found not only for rare-earth intermetallics [40–44], but also for oxides [45, 46]. An instructive textbook-example is Ce metal, which displays a phase transition from a low temperature phase ($\alpha$-Ce) characterized by strong hybridization between the valence band and $4f$ levels, to the high temperature phase ($\gamma$-Ce) with weak hybridization. In figure 4.4, the spectra of both phases are shown, measured by Weschke *et al.* with $h\nu = 120$ eV (bottom) and $h\nu = 884$ eV (top) [41]. While the spectrum of the high temperature phase does not change with photon energy, the low temperature phase spectrum do change significantly. Knowing that the low photon energy spectrum has the larger surface sensitivity, one can immediately conclude that the electronic properties of bulk and surface is rather similar in the $\gamma$ phase, but strongly different in the $\alpha$ phase. The different contributions of the bulk and surface to the low and high photon energy spectra can be utilized to separate the two contributions by performing a subtraction of the spectra with appropriate weights, primarily determined by the different escape depths. Thus, the pure bulk and surface spectra of the $\alpha$ phase can be found, as shown in figure 4.5. First of all, we notice the significantly different line shape of the bulk and surface spectra, in accordance with the observed photon energy dependence. Secondly, the surface spectrum is quite the same as in the high temperature phase, supporting the lack of photon energy dependence in the latter. And most of all, using this method, a quan-
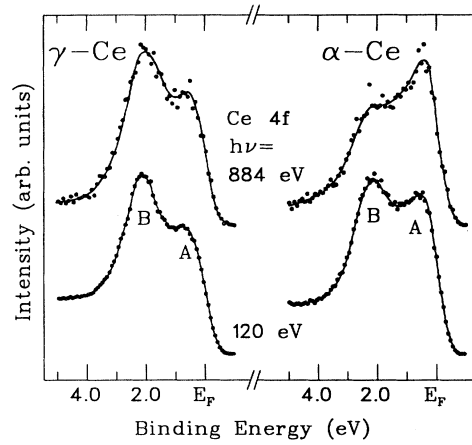
**Figure 4.4:** Photoemission spectra of $\gamma$- and $\alpha$-Ce metal, taken at the $4d \to 4f$ ($h\nu = 120$ eV) and $3d \to 4f$($h\nu = 884$ eV) resonance, respectively. To facilitate a comparison, the total-system resolutions were set equal in both ($= 700$ meV, FWHM). The solid lines serve as guides to the eye, from [41].

titative and reliable analysis of the two contributions (peaks "A" and "B") to the spectra can be made, which results in a more consistent description of the electronic properties of $\alpha$-Ce.

The same phenomena have been observed in other $\alpha$-like Ce-compounds. Ce $3d$ core–level photoemission spectra of CeIr$_2$ taken by Laubschat *et al.* under varying conditions of surface sensitivity are shown in figure 4.6. The spectra consist of three spin–orbit doublets $A$, $B$ and $C$ related to different final state configurations, $4f^0$, $4f^1$ and $4f^2$, respectively. It turns out that the intensity of structure $B$ changes noticeably both with photon energy, and with emission angle, indicating that it is strongly related to the surface sensitivity of the spectra. In both cases, the intensity consistently appears to be enhanced in the more surface sensitive setup, suggesting that the corresponding final state has an increased overlap with the ground state at the surface. The stabilization of the respective ground state contribution $4f^1$ at the surface is supported by similar findings in Ce–$4f$ core–level PES. This
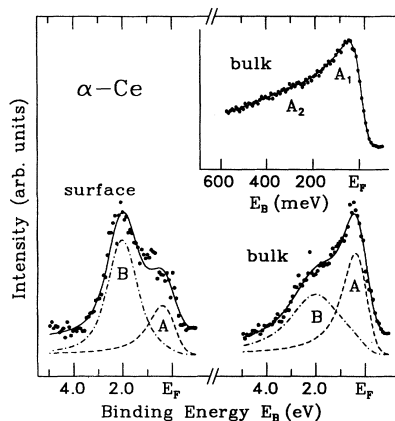
**Figure 4.5:** Surface and bulk photoemission spectra of $\alpha$-Ce metal from [41] derived from the spectra in 4.4. The solid lines represent the result of model calculations. The inset displays the bulk contribution of the high-resolution $4d \rightarrow 4f$ resonant photoemission spectrum of $\alpha$-Ce metal in the region close to $E_F$. The solid lines are guides to the eye.

is interpreted as a strong reduction in the $4f$ hybridization at the surface, which can be confirmed by quantitative simulation of the spectra. The analysis of the surface sensitivity dependence not only demonstrates drastically the degree of dissimilarity in the electronic structures of bulk and surface, but also gives a quantitative example of the importance of a consideration of surface effects: previous PES studies of the same systems not taking surface effects into account, had given averaged values of hybridization energies of less than 50% of the true bulk value, and as a result were in disagreement with theoretical predictions [109].

It is by now clear that one needs to use relatively high photon energies for Ce compounds to obtain spectra which can be considered as representative for the bulks. A recent example with improved instrumental resolution is given for $CeRu_2Si_2$ $CeRu_2$ [44].

Another famous example where the surface sensitivity issue of PES has led to a misinterpretation of the results, and as a consequence to a wrong model, is the calcium substitution series of the perovskite strontium vanadates, $Sr_{1-x}Ca_xVO_3$ [31, 34]. The valence band photoemission spectra of
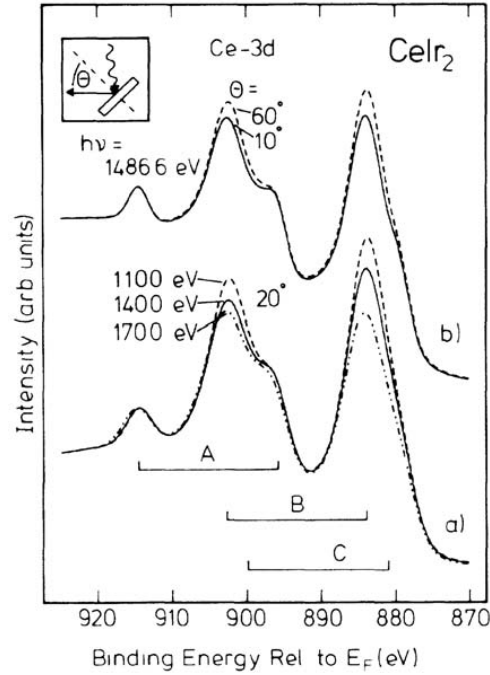
**Figure 4.6:** Ce–3$d$ core–level photoemission spectra of CeIr$_2$ recorded with varying surface sensitivity: (a) for different photon energies and constant electron–emission angle, $\theta = 20°$; (b) for different angles $\theta$ and constant $h\nu = 1486.6$ eV. The spectra consist of three $3d_{3/2}$–$3d_{5/2}$ doublets due to different $4f$ final state configurations; they are normalized to the same intensity of doublet $A$ and corrected for background. Figure taken from Laubschat *et al.* [40].

polycrystalline samples taken with UV light ($\hbar\omega \leq 50$ eV) display a striking $x$ dependence which was interpreted as a consequence of the increasing distortion from the regular structure for $x = 0$ with a V–O–V bond angle of 180°. As the bandwidth $W$ is assumed to be reduced with distortion, the value of $U/W$ increases and correlation effects are expected to gain importance on the spectra. Thus the system was concluded to be close to a Mott–Hubbard transition controlled by bandwidth on tuning the composi-

tion. The observed spectra were explained in terms of non–local correlation effects introducing a $k$–dependent self–energy. On the other hand, thermodynamic and magnetic studies of the vanadates did not show according $x$ dependent behavior, which led to some confusion and a controversial discussion of either findings [110]. A reinvestigation of the photoemission study using higher photon energies up to 900 eV, and applying a careful surface treatment, was necessary to resolve this issue [45]. Figure 4.7 shows the
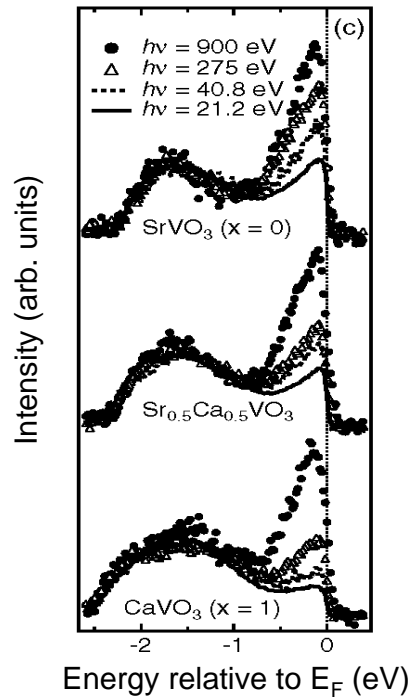


**Figure 4.7:** Photon energy dependent V3$d$ PES of $Sr_{1-x}Ca_xVO_3$. While the low photon energy spectra change with composition, the high photon energy spectra are independent of $x$. Taken from Sekiyama *et al.* [45].

changes of the V 3$d$ spectrum with photon energy, and demonstrates that the seeming $x$ dependence at low photon energies vanishes at higher ones. The decisive improvement of this approach over the previous ones consists

in the bulk sensitivity achieved by both a much longer escape depth, from figure 4.2 estimated a factor four, and a well defined clean surface. The changes in the spectra observed in UPS were thus traced back to surface effects and therefore not representative of the bulk.

## 4.3  Sample preparation and experimental setup

Another significant issue in terms of bulk sensitivity is the sample preparation, not only in the sense of composition, but also of the surface definition. In this respect, the use of single crystals is naturally preferable, since here the surface is well defined in terms of lattice planes, and usually an even surface termination can be achieved. By contrast, the surface of a polycrystalline sample does not have a well defined orientation, and will therefore not be flat and even. As a result, the surface contribution to the photoemission spectrum of a polycrystalline sample is considerably enhanced with respect to the bulk contribution, as compared to a single crystal sample. Moreover, to establish a clean surface is for polycrystalline samples much harder. First of all, the roughness of the surface results in a higher degree of contamination. The often used method to scrape off surface contamination rather tends to carve adsorbate atoms into the surface instead of removing them, due to the granular consistence. Upon fracturing polycrystalline samples instead, again a rough surface is produced, which is rather determined by grain boundaries and impurities, than by the crystal structure, and so is of poor crystalline quality.

These difficulties exist in principle for single crystals as well, but mostly are less severe. Scraping the surface is unfavorable, not only due to the danger to rub in impurities, but also because of the macroscopic scratches left on the surface, which in turn becomes more like a polycrystalline sample. The bottom line is, that the desirable condition is a single crystal which is cleaved *in–situ*, this means split in such a way, that a well defined surface of low crystallographic indices shows up. This is not always possible, however. While many ionic compounds of simple lattice structure usually cleave nicely into specular surfaces, systems of more complicated structure, or soft materials rather break into terraced surfaces or are simply cut along the blade.

In order to obtain reliable results, a PES experiment requires an ultrahigh vacuum (UHV) environment ($\approx 10^{-10}$ mbar), as the sample exposes a

surface of a certain reactivity to an atmosphere of residual gas in the spectrometer chamber. As an example, we consider the case that every particle which hits the surface, will stick there, expressed by a sticking coefficient $S = 1$. An exposure of this surface to a pressure of $2.5 \times 10^{-6}$ torr over one second, a quantity referred to as 2.5 L (Langmuir), results in an estimated contamination of one monolayer. As a result, at a pressure of $10^{-9}$ mbar, and with a sticking coefficient of one, the surface is completely covered with adsorbate particles within one hour. Therefore, the sample has to be kept under UHV conditions, and the experiment should be completed in a few hours — depending on the actual pressure, and the sticking coefficient, which fortunately often is small. As a measure of the surface contamination, photoemission lines of the most common contaminants carbon and oxygen (mostly in form of carbon monoxide and water) can be monitored repeatedly over the time of measurement — usually, if the photon energy permits, the $1s$ core levels at $\approx 285$ and $530\,\mathrm{eV}$, respectively, with the precise binding energies depending on the chemical environment. On the other hand, not only surface contamination effectively changes the sample actually being measured, but also the chemical stability of the system. The sample might either react with contaminants like oxygen, or the chemical composition might change due to evaporation of some constituents, both leading possibly to a system with completely different properties. Since the line shapes and energy positions of the peaks depend on the chemical species, changes in the spectra with time show up clearly and indicate sample degradation.

High resolution, bulk sensitive photoemission spectra were taken in our Cologne laboratory with a VG twin crystal monochromatized Al $K_\alpha$ x–ray source ($h\nu = 1486.6$ eV), and a Scienta SES 100 analyzer. The setup is shown in Figure 4.8. For Fermi–level calibration, spectra of a polycrystalline silver sample were taken before and after each experiment, indicating the stability of the conditions during measurements within $50\,\mathrm{meV}$. The experimental energy resolution was set to $350\,\mathrm{meV}$ for core levels and wide range valence band spectra, and to $270\,\mathrm{meV}$ for the high resolution narrow range valence band spectra. The pressure in the spectrometer chamber was kept in the low $10^{-10}$ mbar range throughout the experiment. The crystals were cleaved *in-situ* exposing a flat surface with an area of $\approx 3 \times 2\,\mathrm{mm}^2$. The probing depth is maximized by measuring at normal emission.
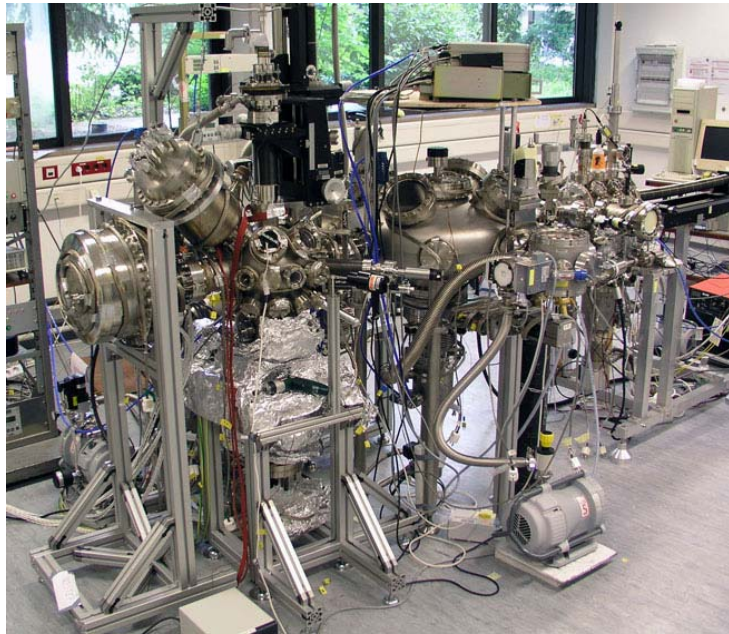
**Figure 4.8:** XPS setup in Cologne.

# Chapter 5

# Evolution of spectral weight

## 5.1 Introduction

One of the long standing topics in theoretical solid state physics concerns the single-particle spectral weight distribution in Mott-Hubbard systems across the metal-insulator transition (MIT) [2, 30]. Several principle models have been proposed to describe the spectral changes which could occur when the strength of the Coulomb energy $U$ is tuned relative to that of the one-electron band width $W$. In Hubbard's original approach [111–113], the transition is a simple splitting of the half-filled single band into the now-called lower and upper Hubbard band (LHB and UHB). This approach works well for the large $U$ limit, but fails to describe the low energy excitations of the metal. Brinkman and Rice [114], by contrast, predicted that the transition should be accompanied by a divergence of the effective mass. Their model is suitable to describe the low energy physics of the metal, but not for the high energy excitations nor the insulating state. Most recent studies based on the dynamical mean field theories (DMFT) [47–50] are aiming to describe both the low and high energy excitations. A sketch of these different scenarios is given in figure 5.1.

On the experimental side, there are only very few studies which aim to systematically address the $U$ vs. $W$ issue. Although numerous spectroscopic measurements have been carried out on materials showing MIT, it turns out that in most cases the interpretation cannot be done in terms of $U$ vs. $W$ only. Photoemission (PES) experiments on the famous $V_2O_3$ [116] and $VO_2$ [13] systems, for example, show changes which are so dramatic that
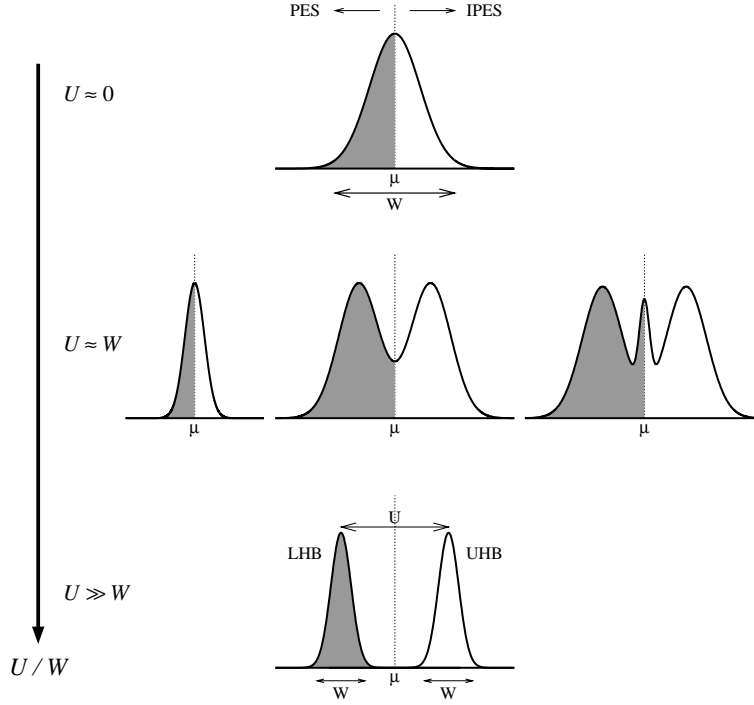
**Figure 5.1:** Photoemission and inverse photoemission spectra as expected in a Hubbard model for different values of U/W. The grey shading indicates occupied states. Adapted from Morikawa *et al.* [37] and Hesper [115].

one should seriously consider the involvement of inter-site spin and orbital correlations [10–12, 117]. In this respect, the class of $d^1$ perovskites may form a unique window of opportunity [31–37, 118–120], related possibly to the near degeneracy of its orbital states [24, 25, 121].

Indeed, the comparative PES study on the band-width-controlled material, $Ca_{1-x}Sr_xVO_3$, by Inoue *et al.* [34] yield striking systematic changes which triggered strong interest from the community working in the field of correlated electron systems. Nevertheless, recent PES investigations [45, 46] inferred that most of those observations could be artifacts related to the surface of the material, and that the changes between bulk $CaVO_3$ and $SrVO_3$ are too small to be detected. DMFT calculations also indicate that
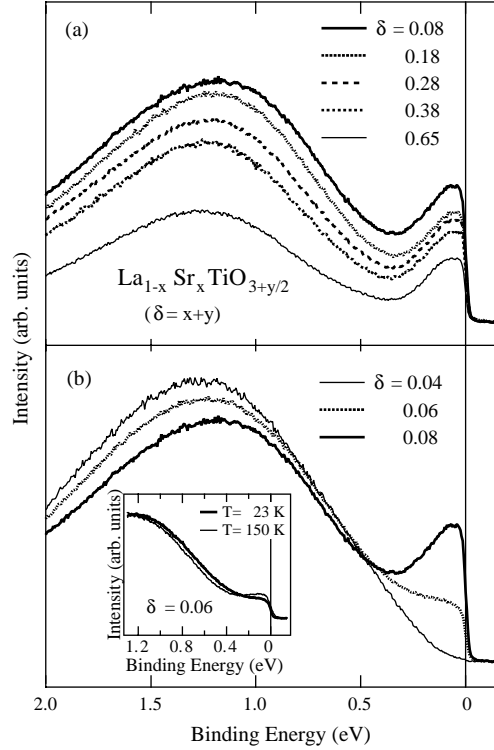
**Figure 5.2:** Photoemission spectra of $La_{1-x}Sr_xTiO_3 + y/2$ in the Ti $3d$ band region in the high-doping regime (a) and the low-doping regime (b). The inset shows the spectra of the AFM sample ($\delta = 0.06$) below and above $T_N = 112\,K$, from [120].

the differences in band width are too small to have a noticeable impact on the spectra [27, 45, 51].

Also in the titanates one could observe very interesting features: upon doping new states are created in the vicinity of the chemical potential in the $La_{1-x}Sr_xTiO_{3+\delta}$ as shown in figure 5.2 from the PES study by Yoshida *et al.* [120]. Important is that this occurs with an appreciable sharp Fermi cut-off, very much unlike magnetite in the metallic phase [38,39]. This seems to indicate that polaronic effects do not play a major role, making the system ideal to study the basics of the evolution of spectral weight in doped mag-
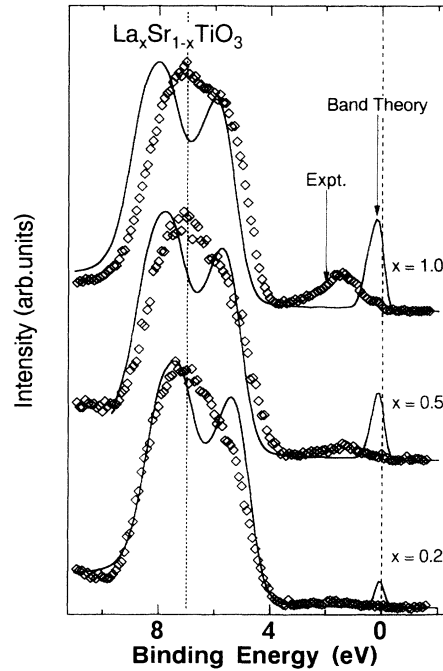
**Figure 5.3:** Photoemission spectra ($h\nu = 48\,\text{eV}$) compared with the band-structure calculation. the vertical line shows th efixed position of the $2p$ band, from [32].

netic insulators without extra complications. Surprising is that this PES study found very heavy masses for the doped charge carriers, not so consistent with data obtained from thermodynamic measurements. Puzzling is the fact that other PES studies of similar type of materials [31, 32, 37, 118–120] produce different weights at the Fermi level upon doping, with some of them even staying insulating. Directly worrying is that the reported O $2p$ valence bands from these PES experiments are not consistent with the LDA band structure calculations, while one does expect that band structure calculations should work for the O $2p$ bands since electron correlation effects will not be too pronounced for these relatively broad bands. This discrepancy is illustrated by figure 5.3 from the PES study by Fujimori *et al.* [32].

Our conjecture is that all PES spectra reported so far in the literature are plagued by the surface sensitivity of the type of photoemission used in those

studies, and that therefore they are not representative for the bulk material. Recent PES studies on correlated oxides using high photon energies (soft-x-rays and x-rays) to be more bulk sensitive [45, 46] have indeed revealed quite different spectra than those taken with ultra-violet light.

## 5.2 LaTiO$_3$ and YTiO$_3$: bulk-sensitive PES

To investigate to what extent photoelectron spectroscopy is valuable for the detailed understanding of the electronic structure of the titanates, we have to establish first that spectra can be obtained which which are truely representative for the bulk material. We will start with PES measurements on LaTiO$_3$ and YTi$_3$, where efforts are made to optimize the bulk-sensitivity of the technique: we use single crystals cleaved *in-situ* and measure them at normal emission, and we use Al-K$\alpha$ x-rays rather than the ultra-violet light used so far in the literature. The single crystals of LaTiO$_3$ and YTiO$_3$ have high magnetic ordering temperatures, namely a Néel temperature of 148 K for the LaTiO$_3$ and a Curie temperature of 29 K for the YTiO$_3$, indicating the accurate oxygen stoichiometry.

The top curves of Fig.5.4 show the valence band PES spectra of LaTiO$_3$ and YTiO$_3$. The spectra consist of the Ti 3$d$-derived states centered at around 1-2 eV binding energy, well separated from the O 2$p$ bands which are spread out between 5 and 9 eV. These spectra have quite different lineshapes from the ones published so far [31–33, 37], not only for the Ti 3$d$ but also for the O 2$p$ region. To test the correctness of our spectra, we will analyze the O 2$p$ lineshapes of Fig. 5.4 in detail, with attention also to the fact that the O 2$p$ band of LaTiO$_3$ is *not* identical to that of YTiO$_3$. To do so we will utilize band structure calculations, since one can safely assume that electron correlation effects will not be too pronounced for the relatively broad O 2$p$ bands.

We perform our GGA calculations in the non-magnetic state by using the full-potential augmented plane waves plus local orbital method [122]. We take the crystal structure data of LaTiO$_3$ determined by neutron diffraction at 8 K [20] and of YTiO$_3$ by X-ray diffraction at 127 K [58]. The muffin-tin sphere radii are chosen to be 2.9, 2.5, 2.1 and 1.6 Bohr for La, Y, Ti, and O atoms, respectively. The cut-off energy of 16 Ryd is used for plane wave expansion of interstitial wave functions, and 6×4×6 **k**-mesh for integrations over the Brillouin zone. The results are in good general agreement with

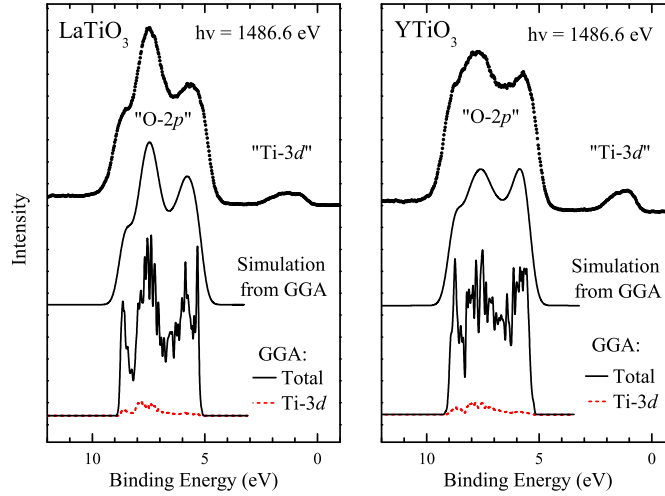**Figure 5.4:** (color online) Valence band of $LaTiO_3$ (left panel) and $YTiO_3$ (right panel). Top: experimental spectra taken at $100\,K$ with $1486.6\,eV$ photons and $0.35\,eV$ overall resolution. Middle: simulation for the O $2p$ region based on the GGA. Bottom: total (black/solid), and Ti $3d$ (red/dashed) GGA density of states.

earlier calculations [27, 31–33, 37, 67–69]. The total density of states (DOS) for the O $2p$ band region is shown as the bottom curves of Fig. 1. Here the Ti $3d$ partial DOS, as defined within the Ti muffin-tin sphere, is also plotted separately, to show that its contribution to the total DOS in the O $2p$ region is negligible, or in other words, that the total DOS in this region is given indeed overwhelmingly by the O $2p$.

To compare the GGA results with the experiment, we broaden the total DOS by about $0.6\,eV$ FWHM (full-width-half-maximum) to account for the experimental resolution as well as lifetime and phonon broadening. The results are shown as the middle curves of Fig. 5.4. One can clearly observe the excellent agreement between the simulations and the experiments. Important is also the fact that the experimental lineshape differences between $LaTiO_3$ and $YTiO_3$ are reproduced to a great detail by the simulations. While the excellence of the agreement may be somewhat fortuitous, it provides us at least with the confidence that there are indeed observable

differences in the one-electron band width which can be associated with differences in the local distortions of the TiO$_6$ octahedra and in the Ti-O-Ti bond angles. It also leads us to conclude that our spectra are indeed representative for the bulk materials considered, so that we are in the position now to study reliably the many body effects in the Ti $3d$ spectral weight distribution as a function of the one-electron band width.

## 5.3 LaTiO$_3$ and YTiO$_3$: $d^1$ Spectral Weight

The left and middle panels of Fig. 5.5 show the Ti $3d$ spectral weight distribution of LaTiO$_3$ and YTiO$_3$. The curves labelled "$h\nu$=1486.6 eV" are the experimental spectra taken at 100 K with an overall energy resolution of 0.27 eV. One can clearly see also here that there are substantial differences between the two compounds. While in the O $2p$ region the differences are mainly in the relative heights of the peaks, in the Ti $3d$ the differences are in the width: LaTiO$_3$ has about 20% larger band width than YTiO$_3$. We note that the lineshapes of these spectra are quite dissimilar to those reported in the literature [31–33,37]. In fact, the literature PES data show Gaussian-like lineshapes with almost no difference between the two compounds, which is quite puzzling in view of the general expectation that the difference in the optical gap should somehow be related to differences in the one-electron band width [35]. By contrast, our spectra are very consistent with the optical data. The larger band gap for YTiO$_3$ is also reflected by the fact that the top of its valence band is located at a higher binding energy than that of LaTiO$_3$.

To investigate to what extent correlation effects play a role in these two titanates, we compare the Ti $3d$ spectra with the occupied Ti $3d$ density of states as calculated using the GGA. The top curves of Fig. 5.5 reveal first of all that such a one-electron approach predicts the system to be a metal, in stark contrast to reality. The second point which calls for attention is the narrowness of the calculated occupied band: it is about a factor three too small as compared with the experiment. While the first point indicates that correlation effects are indeed sufficiently strong to open up a band gap and make these titanates to be Mott insulators, the second point requires a more subtle explanation, as we will describe below.

As an *ansatz* to take into account correlation effects, we perform GGA+U calculations with the Hubbard $U$ set at 3 eV and the Hund exchange $J$ at
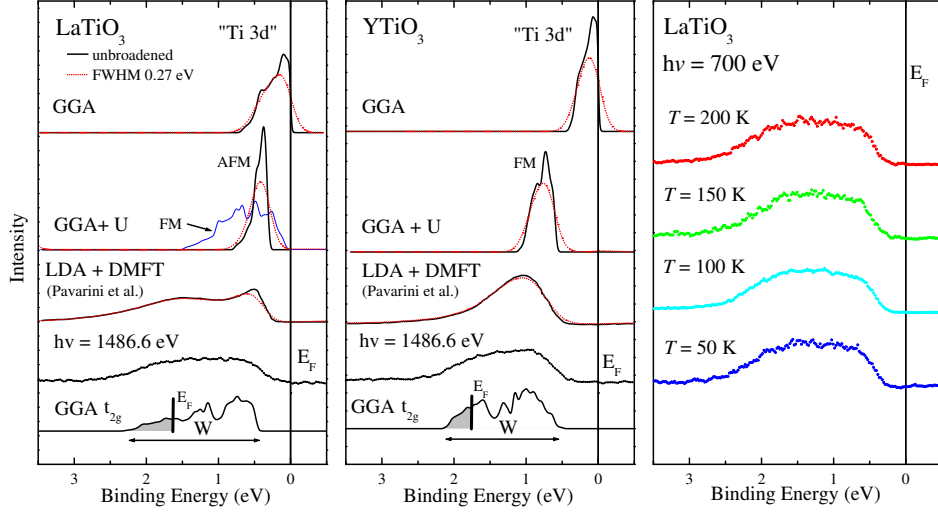
**Figure 5.5:** (color online) Ti $3d$ region of the valence band of $LaTiO_3$ (left panel), $YTiO_3$ (middle panel). Top two curves: occupied total density of states from GGA and GGA+U calculations (unbroadened/black, 0.27 eV FWHM broadened/red-dashed). The GGA+U result for an artificially ferromagnetic (FM) $LaTiO_3$ is also included (thin-blue-line). Middle curves: spectral weight from LDA+DMFT calculations as reproduced from E. Pavarini *et al.* [27]. Bottom two curves: experimental spectra taken at 100 K with 1486.6 eV photons and 0.27 eV overall resolution, together with the occupied (filled-grey) and unoccupied GGA $t_{2g}$ density of states (shifted and unbroadened). Right panel: Experimental spectra of $LaTiO_3$ taken at 50, 100, 150 and 200 K.

0.7 eV for the Ti $3d$ electrons. We find a band gap of 0.4 eV for antiferromagnetic (AFM) $LaTiO_3$ and 0.8 eV for ferromagnetic (FM) $YTiO_3$, in close agreement with the optical data [35]. The calculated Ti $3d$ densities of states are plotted in Fig. 5.5 and labelled by GGA+U. One can clearly see that they do not reproduce the experimental spectra at all as they are much too narrow.

In the GGA+U for $LaTiO_3$ the band width is much reduced since in the G-type AFM structure the nearest neighbor Ti-O-Ti hopping in each spin channel involves states which are split by $U$. This explanation can be confirmed by repeating the calculation but now for an artificially FM

state. In the latter case the lowest occupied majority-spin orbitals at each site have similar energies, allowing for nearest neighbor hopping without the involvement of $U$ and thus producing a much wider band as shown by the thin-blue-line in Fig. 5.5. For YTiO$_3$ we find that in the GGA+U the Ti-O-Ti transfer integrals for the occupied orbitals are very small despite the FM state. This is due to their near-orthogonality in the G-type-like antiferro-orbital structure. A calculation for an artificially AFM state produces even narrower bands (not shown). So the GGA+U formalism is able to reproduce the insulating state and the magnitude of the band gap, but fails completely for describing spectral weight distributions [67, 69]. This can also be said about other methods which include electron correlations in a mean field manner [23, 68, 123].

A quite different approach is offered by methods based on the DMFT [47–50]. Aiming to describe both the low and high energy excitations simultaneously, one projects self-consistently the electronic structure of the solid with its dynamic response onto a solvable impurity problem. The price to pay is that the $k$-dependence of the self-energy is lost [124, 125]. This could be a serious omission for cases where, for instance, the effective band width is affected by the significant Hund's rule exchange via the inter-site exchange interactions [10], but perhaps this causes less of an error for the propagation of a hole in a $d^1$ system. In Fig. 5.5 we reproduce the results of the LDA+DMFT obtained very recently by Pavarini *et al.* [27]. Here we took the liberty to align the theoretical spectra in energy so that the leading edge near $E_F$ coincides with that of the experiment. One can observe the very good correspondence between theory and experiment. The large width of the spectra is well reproduced. This is a major improvement in comparison to the GGA and GGA+U. The lineshape for the LaTiO$_3$ is explained remarkably well, although the hint for a peak at the top of the valence band is lacking in the experiment. The appearance of this peak is perhaps related to the fact that the calculations have been done using a quantum Monte Carlo scheme down to a temperature of 770 K only [27], causing crystal-field-split excited states to be thermally populated. The calculated spectrum for YTiO$_3$ fits satisfactorily, with also here the remark that the theory shows the tendency to put too much weight on the low binding energy side of the spectrum.
With the encouraging agreement between the DMFT results and the experiment, there is also the finding that these titanates are Mott insulators having

strongly polarized orbital occupations [27,29]. The question therefore arises to what extent charge fluctuations, which the DMFT is designed to handle, are relevant here. To answer this, we show in the bottom of Fig. 5.5 the *entire* GGA $t_{2g}$ band of $LaTiO_3$ and $YTiO_3$, i.e. both the occupied and unoccupied parts. It is surprising how well these one-electron band widths $W$ fit to the widths of the experimental spectra, including the 20% larger width in $LaTiO_3$ as compared to $YTiO_3$.

To see the astonishing implications of this observation, we consider the case of the ferromagnetic half-filled single-band Hubbard insulator in the large $U$ limit. In this simple system, an extra hole, once injected by PES, can propagate without experiencing additional Coulomb repulsions and with transfer integrals given by the one-electron band width. In other words, the valence band of this correlated insulator is the same as the combined occupied and unoccupied band of the uncorrelated metal. It is extremely surprising that these characteristics fit the titanates since they have electronically quite distinct orbital- and/or spin (super-) structures. One would at least expect that the propagation of an extra hole would lead to a wake of wrongly oriented orbitals and/or spins, thereby reducing the quasi-particle or the coherent band width in a manner which may be explained by the well known $t$-$J$ models [126]. Nevertheless, the entire band width, i.e. including the incoherent part, may very well be given by the bare one-electron band width [127,128]. The question is then why the nearest-neighbor spin and orbital correlations in such a $t$-$J$ like $d^1$ system do not show up clearly in the $k$-integrated photoemission experiment. Our assertion is that the energy scale associated with these inter-site correlations (typically much less than $0.1\,eV$), is too small in comparison with the total band width ($1.5$-$2.0\,eV$) and the experimental broadening ($0.3\,eV$). To support this idea experimentally, we measured the valence band of $LaTiO_3$ as a function of temperature ($50$–$200$ K) as to go from the antiferromagnetic to the paramagnetic phase. The results are shown in the right panel of Fig. 5.5. The data reveal essentially no detectable temperature dependence. Again, this is surprising by itself since we know that the spin-spin correlations change considerably across the Néel temperature, but it is consistent with and confirming our assertion about the energy scales involved.

## 5.4 La$_{1-x}$Sr$_x$TiO$_{3+\delta}$: doping dependence

In the previous sections we have established that photoelectron spectroscopy using x-rays on La TiO$_3$ and Y TiO$_3$ single crystals do provide spectra which are representative for the bulk material. We also have observed that the $d$ spectral weight distribution in these $d^1$ Mott insulators has surprisingly strong similarities with that of a classic $t$-$J$ model developed for high $T_c$ cuprate superconductors. Our next step is to study the doping dependence of the spectral weight distribution in these titanate materials.
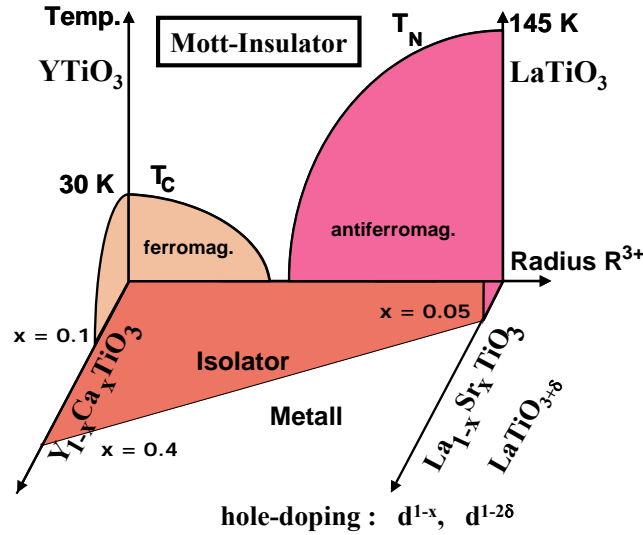


**Figure 5.6:** Phase diagram of the Y TiO$_3$-La TiO$_3$ system with Ca, Sr and O doping.

Fig. 5.6 shows the phase diagram of the YTiO$_3$-LaTiO$_3$ system with Ca, Sr and O doping. For our study here we will focus on the La$_{1-x}$Sr$_x$TiO$_{3+\delta}$ series. The introduction of Sr or excess oxygen into the LaTiO$_3$ system implies in both cases the doping of holes as charge carriers. However, the amount of doped holes will be different. In the case of Sr, the hole concentration will be given by the Sr concentration $x$ leading to a nominal $d^{1-x}$ configuration for the Ti ions, while in the case of excess oxygen the hole concentration will be equal to twice the amount of excess oxygen $\delta$ setting

the nominal Ti configuration to $d^{1-2\delta}$, since each excess oxygen ion takes away two electrons from the system.
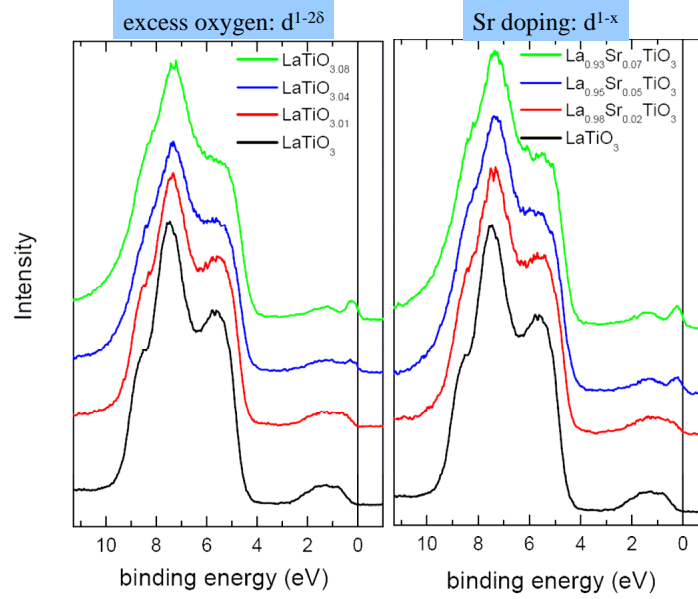


**Figure 5.7:**   (color online) Valence band photoemission spectra of $La\,TiO_{3+\delta}$ (left panel) and $La_{1-x}Sr_x TiO_3$ (right panel). The spectra were taken at 100 K with 1486.6 eV photons and 0.35 eV overall resolution.

Fig. 5.7 shows the valence band PES spectra of $La\,TiO_{3+\delta}$ (left panel) and $La_{1-x}Sr_x TiO_3$ (right panel). The $\delta$ values range from 0 to 0.08 and the $x$ from 0 to 0.07. The structures in the O $2p$ derived bands of the undoped $La\,TiO_3$ become washed out upon doping and the overall band width becomes also somewhat larger. This may not be inconsistent with the crystallographic observation that the tilt angles of the $TiO_6$ octahedra is reduced upon doping, in which case one could envision that this would lead to larger hopping integrals. More important is that the Ti $3d$-derived states centered at around 1-2 eV binding energy show quite dramatic changes upon doping. We note that our spectra have quite different lineshapes from the ones published so far [31, 32, 37, 118–120].

To analyze the Ti $d$ spectral weight in more detail, we present in Fig.5.8
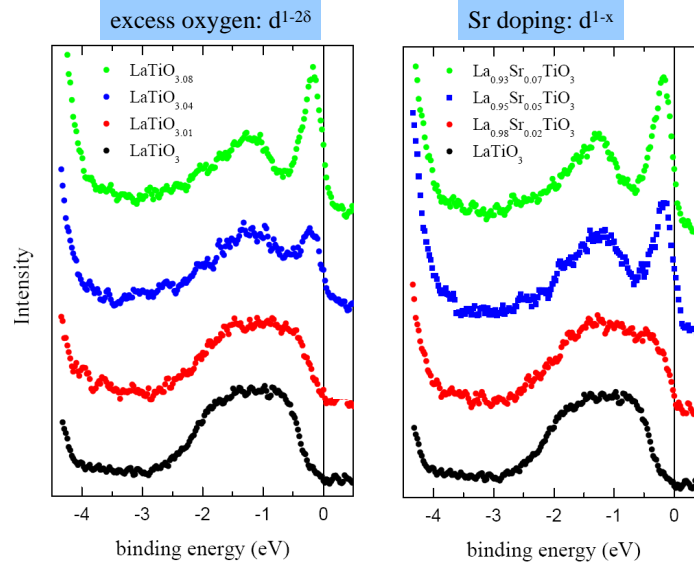
**Figure 5.8:** (color online) Close-up on the Ti $3d$ valence band photoemission spectra of La TiO$_{3+\delta}$ (left panel) and La$_{1-x}$Sr$_x$TiO$_3$ (right panel). The spectra were taken with $0.27\,\text{eV}$ overall resolution.

a close-up of the valence band PES spectra in the vicinity of the Fermi level. These spectra were taken with a (slightly) higher overall energy resolution: $0.27\,\text{eV}$. One can clearly see that in the initial stages of doping, i.e. for the smallest doping concentrations namely $\delta$=0.01 and $x$=0.02, the Fermi level gets pinned at the top of the valence band while it was located inside the band gap for the undoped (pure) La TiO$_3$. This confirms spectroscopically that Sr doping or excess oxygen corresponds to hole doping.

Upon further doping, a new state at the Fermi level is being built up quickly, thereby showing a very clear Fermi cut-off with a sharpness which is determined by the experimental resolution. The doped material seem to be a 'good' metal, very much unlike magnetite in the metallic phase [38,39]. Polaronic effects seem not play a major role in the titanates. Important is also the observation that the creation of the new state at the Fermi level is accompanied by a rapid decrease of the spectral intensity at about $1\,\text{eV}$ binding energy. This rapid transfer of spectral weight, from the so-called

incoherent peak at $1\,\mathrm{eV}$ energy to the coherent peak at the Fermi level, is very characteristic for the correlated nature of this material. An ordinary band semiconductor will not show such a transfer of spectral weight upon doping.

Comparing our data with those of Yoshida *et al.* as displayed in Fig. 5.9 [120] reveals that the transfer of spectral weight as function of doping occurs more rapidly in our bulk-sensitive photoemission spectra. This means directly that the charge carrier mass renormalization is not as large as suggested by the Yoshida study. Making a crude estimate, we expect that our data would yield a factor of three smaller values than Yoshida, thereby arriving at a result which is more consistent with the thermodynamic measurements.
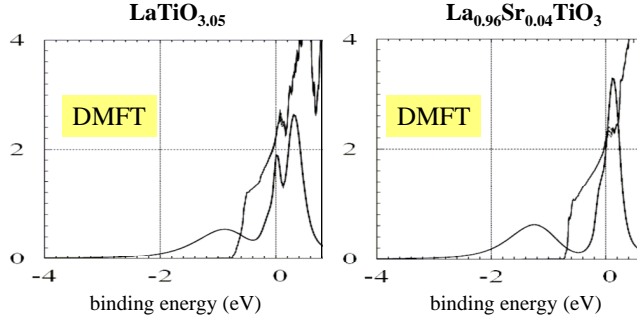


**Figure 5.9:** (color online) Calculated Ti $d$ spectral weight using LDA+DMFT by E. Pavarini (unpublished): $LaTiO_{3.05}$ (left panel) and $La_{0.96}Sr_{0.04}TiO_3$ (right panel). Real crystal structures have been used.

In comparing the oxygen excess data with those for Sr doping, we notice that the transfer of spectral weight for $\delta=0.04$ is not more than for $x=0.05$, and that it is practically equal for $\delta=0.08$ and $x=0.07$. This is surprising since one would expect that the transfer of spectral weight would be proportional to $2\delta$ and $x$. Apparently, the oxygen excess system is different from the Sr system. Very recently, E. Pavarini has calculated the Ti $d$ spectral weight for $LaTiO_{3.05}$ and $La_{0.96}Sr_{0.04}TiO_3$ using the real crystal structure for each of these two compositions. These LDA+DMFT results are displayed in Fig. 5.9. We can clearly see that the spectral weight for the coherent peak at the Fermi level ($0\,\mathrm{eV}$ energy) relative to the incoherent peak at $1\,\mathrm{eV}$ energy in

the $\delta$=0.05 compound is almost the same as that in the $x$=0.04 compound, although the amount of hole doping relates as 2×0.05 to 1 × 0.04, i.e. differing by a factor 2.5. A closer look at the coherent spectral weight in the vicinity of the Fermi level reveals the origin of this remarkable result: the coherent peak in the oxygen excess sample has a larger width than that in the Sr material. This is related to the fact that the Sr material has a crystal structure closer to the ideal cubic perovskite, so that the crystal field splitting in the $t_{2g}$ levels is smaller than that in the oxygen excess sample. We then infer that a smaller crystal field splitting would effectively mean a larger degeneracy, and thus a smaller effective $U/W$ ratio [129–131], so that a coherent peak can be built up much quicker upon doping.

# Summary

One of the most intriguing aspects of transition metal oxides is the wide variety and richness of their physical properties. They display quite often unconventional magnetic and electronic phenomena, including metal-insulator transitions, colossal magneto-resistance, superconductivity, spin-state transitions, magneto-optical activity and spin-dependent transport. Much of these properties can be traced back to the correlated motion of the electrons in these materials. There is a strong interplay of a large number of microscopic interactions, leading often to an abundance of competing electronic phases which respond extremely sensitive to small changes in their chemical or physical environment. This feature makes transition metal oxides to be valuable ingredients for the design of advanced materials with novel functional properties.

Microscopic understanding of the unconventional behavior of this class of materials is at the heart of modern solid state physics research. The many body nature of the problem forms a true intellectual challenge requiring modern experimental and theoretical methods. There is a need for well-defined materials which can serve as model systems. The class of the $RE$TiO$_3$ ($RE =$ rare earth) materials forms in this context a very interesting 'playground' for the quantitative study of the properties and excitation spectra of correlated oxides. It has the relatively simple perovskite crystal structure, and the Ti ions have (formally) only one electron in their $3d$ shell so that complications related to atomic multiplet effects can be avoided. Yet, the orbital degeneracy together with the presence of a small band gap lead to a number of interesting physics which are then subject of a flurry of detailed experimental and theoretical studies. Efforts are being made for a quantitative analysis as to test the accuracy of various theoretical approaches.

Here we report on a detailed experimental study of the electronic struc-

ture of the $RE$TiO$_3$ system. The study aims to address one of the long standing topics in theoretical solid state physics, namely the single-particle spectral weight distribution in Mott-Hubbard systems in the vicinity of the metal-insulator transition. In view of the existing discussions in the literature, it turned out to be crucial to use well defined samples: we have to grow titanate single crystals with well defined stoichiometry and doping. This activity in fact forms the basis of this thesis work and much effort is also put into the characterization of the crystals using various methods including x-ray and neutron diffraction, as well as magnetic, transport and thermodynamic measurements.

We have used photoelectron spectroscopy to investigate the electronic structure of the $RE$TiO$_3$ system. Although many photoemission studies have been reported in the literature, it is also realized more and more that those published results may not be representative for the material due to the extreme surface sensitivity of the particular photoemission technique used in those studies. This is important since the electronic structure of the surface is very different from the bulk, especially for strongly correlated systems. Essential aspect of the work is therefore to carefully optimize the conditions for this type of experiments as to make sure that the spectra obtained are truly representative for the bulk material. Only in this manner we can do a critical and quantitative evaluation of the various advanced many-body models currently available trying to describe the excitation spectra of strongly correlated systems.

The main result of our spectroscopic study is as follows: we have utilized bulk-sensitive x-ray photoelectron spectroscopy to study the valence band spectral weight distribution of $d^1$ Mott insulators LaTiO$_3$ and YTiO$_3$. We observed appreciable differences in the spectra, reflecting the difference in the one-electron band width $W$. We also found that the Ti 3$d$ spectra of both materials are much broader than the occupied 3$d$ bands calculated by band theories. The mean-field inclusion of the Hubbard $U$ explains the band gap but produces even narrower bands, indicating the complete breakdown of standard mean-field theories in describing excitation spectra. We associate the observed spectra with the propagation of a hole in a system with surprisingly well suppressed charge fluctuations thereby showing characteristics of a $t$-$J$ model. Upon doping we observe the creation of the new state at the Fermi level which is accompanied by a rapid decrease of the spectral intensity at about 1 eV binding energy. This rapid transfer of spectral weight

characterizes the correlated nature of this material, and distinguishes this material clearly from ordinary band semiconductors. Surprisingly, we find also a large difference in the speed of transfer of spectral weight when comparing doping using excess oxygen or using Sr substitution. LDA+DMFT calculations suggest that this could be related to the fact that the Sr material has a smaller crystal field splitting in the $t_{2g}$ levels than the oxygen excess sample, yielding an effectively larger degeneracy and thus a smaller effective $U$ versus $W$ ratio.

# Zusammenfassung

Eine der faszinierendsten Aspekte der Übergangsmetalloxide sind ihre vielfältigen Eigenschaften und reichhaltigen physikalischen Eigenschaften. Sie zeigen sehr häufig ungewöhnliche Eigenschaften wie der Kollosale Magnetwiderstand, Supraleitung, Spinübergange, magnetooptische Aktivität sowie spinnabhängigen Transport. Viele dieser Eigenschaften können auf das korrelierte Verhalten der Elektronen zurückgef"hrt werden. Es ergibt sich ein starkes Zusammenwirken der vielzahligen mikroskopischen Wechselwirkungen, welches häufig zu einer Fülle von konkurrierenden electronischen Phasen f̈hrt, und so sehr empfindlich schon auf geringste änderungen der chemischen und physikalischen Randbedingungen reagiert. Diese Eigenschaft macht macht die Übergangsmetalloxide wertvollen Klasse für die Entwicklung von intelligenten Materialien mit neuen funktionellen Eigenschaften.

Das mikroscopische Verständnis des unkonventionellen Verhaltens dieser Materialklasse ist das Herzstück der modernen Festkörperforschung. Der Vielteilchen-Charakter des Problems stellt eine intellektuelle Herausforderung dar, die moderne experimentelle und theoretische Methoden benötigt. Es gibt eine Bedarf an gut definierten Materialien, welche als Modellsysteme dienen können. Die Klasse der RETiO$_3$ (RE = rare earth) Verbindungen bietet in diesem Zusammenhang ein sehr interessantes Spielfeld zur quantitativen Studie der Eigenschaften und der Anregungsspektren der korrelierten Oxide. Sie besitzt eine relativ einfachen Perowskitstruktur, und jedes Ti-Ion besitzt formal nur ein Elektron in der $3d$ Schale wodurch sich keine komplizierten atomaren Multipletteffekte ergeben. Erst die orbitale Entartung zusammen mit einer kleinen Bandlücke führt zu einer reichhaltigen und interessanten Physik, welche das Objekt unzähliger experimentellen und theoretischen Studien ist. Große Anstrengungen wurden für eine quan-

titative Analyse unternommen, um verschidene theoretische Annäherungen zu testen. Hier stellen wir ein detaillierte experimentelle Studie der elektronischen Struktur des RETiO$_3$ Systems vor. Das Ziel dieser Untersuchung ist es, einen lange austhehenden Gesichtspunkt der theoretischen Festkörperphysik zu prsentieren, nmlich die Einteilchen- Verteilung des spektralen Gewichts im Mott-Hubbard System in der nähe des Metall-Isolator-Übergangs. Bei der Betrachtung der Literatur zu diesem Thema, stellt sich heraus, wie entscheidend die Verwendung von gut definierten Proben ist: Deshalb haben wir zunächst Titanat Einkristalle mit einer gut definierten Stöchiometrie bzw. Dotierungsgrad gezüchtet. Diese Aufgabe stellt die Grundlage dieser Arbeit dar, bei der ebenfalls große Sorgfalt zur Charakterisierung der Kristalle aufgebracht wurde. Hierbei wurden verschiedene Methoden wie Röntgen- und Neutronendiffraktion oder Messungen der magnetischen thermischen und Transporteigenschaften angewendet.

Zur Untersuchung der elektronischen Struktur haben wir Photoelektronspektroskopie verwendet. Obwohl schon viele Photoemissionsstudien in der Literatur bekannt sind, zeigte sich mehr und mehr, dass die veröffentlichten Ergebnisse nicht represäntativ für das Material waren, da die verwendeten Photoemmisionstechniken äußerst oberflächenempfindlich sind. Dies ist sehr wesentlich, da sich die elektronische Struktur der Oberfläche deutlich von den der des Bulks unterscheidet, insbesondere bei den korrelierten Elektronensystemen. Ein wesentlich Aspekt dieser Arbeit war deshalb die gewissenhafte Optimierung der Bedingungen für diese Art von Experimenten, um sicherzustellen, dass die aufgenommenen Spektren auch wirklich represäntativ für die Bulkeigenschaften sind. Nur auf diesem Wege kann eine kritische und quantitative Prüfung der unterschiedlichen aktuelle Vielteilchenmodelle, die versuchen, das Anregungsspektrum der korrelierten Elektronensysteme zu beschreiben, erfolgen.

Das Hauptergebnis unserer spektroskopischen Studie ist das folgende: Wir haben bulksensitive Röntgen Photoelektronenspektroskopie betrieben, um die spektrale Gewichtsverteilung des Valenzbandes der $d^1$ Mottisolatoren LaTiO$_3$ und YTiO$_3$ zu untersuchen. Dabei beobachten wir merkliche Unterschiede in den Spektren, was die unterschiedliche Bandbreite des Einelektronenbandes widerspiegelt. Wir stellen dabei fest, dass das Ti $3d$ Spektrum der beiden Materialien deutlich größer ist, als dies Bandtheorien ergeben. Der Meanfield-Ansatz des Hubbard U beschreibt zwar die Bandlücke, erzeugt aber viel zu schmale Bänder, was einen kompletten

## 5.4 La$_{1-x}$Sr$_x$TiO$_{3+\delta}$: doping dependence

Zusammenbruch der normalen Meanfield-Theorien zur Beschreibung des Anregungsspectrums bedeutet.

Wir verbinden mit den beobachteten Spektren das Propagieren eines Lochs in einem System mit erstaunlicherweise stark unterdrückten Ladungs-fluktuationen, was den Charakteristiken des t-J Modells entspricht. Bei der Ladungsdotierung beobachten wir das Erscheinen eines neuen Zustandes am Ferminiveau, welches mit einem raschen Anstieg der spektralen Intensität bei einer Bindungsenergie von ca. 1 eV verbunden ist. Diese rasche Ver-schiebung des spektralen Gewichts ist charakteristisch für die Natur korre-lierter Elektronensysteme, und hebt diese Materialien deutlich von gewöhn-lichen Bandhalbleitern ab. Überraschenderweise zeigt sich auch einen großen Unterschied in der Verschiebung des spektralen Gewichts im Vergleich zwi-schen Lochdotierung durch Sr-Substitution und Sauerstoffüberschuss.

LDA+DMFT Berechnungen legen nahe, dass dieser Effekt daher rührt, dass das Sr dotierte Material eine kleinere $t_{2g}$ Auspaltung besitzt als das sauerstoffdotierte System, was einer größeren Entartung und damit einem kleineren effektiven Verhältnis von U/V entspricht.

# Bibliography

[1] For a review see: "Electronic Conduction in Oxides" by N. Tsuda, K. Nasu, A. Yanase, and K. Siratori, Springer Series in Solid-State Sciences 94, (Springer Verlag, Berlin 1991).

[2] M. Imada, A. Fujimori, and Y. Tokura, Rev. Mod. Phys. **70**, 1040 (1998).

[3] R. Birgenau and M. Kastner, Science **288**, 437 (2000).

[4] Y. Tokura and N. Nagaosa, Science **288**, 462 (2000).

[5] J. Orenstein and A. Millis, Science **288**, 468 (2000).

[6] For a review see: A. P. Ramirez, J. Phys.: Conden. Matter **9**, 8171 (1997).

[7] D. I. Khomskii and G. A. Sawtzky, Sol. State Commun. **102**, 87 (1997).

[8] A. Maignan, C. Martin, D. Pelloquin, N. Nguyen, and B. Raveau, J. of Solid State Chem. **142**, 247 (1999).

[9] A. Maignan, V. Caignaert, B. Raveau, D. Khomskii, and G. Sawatzky, Phys. Rev. Lett. **93**, 026401 (2004).

[10] J.-H. Park, L. Tjeng, J. Allen, C. Chen, M. P., and H. J.M., Phys. Rev. B **61**, 11506 (2000).

[11] S. Biermann, A. Poteryaev, A. Lichtenstein, and G. A., Phys. Rev. Lett. **94**, 026404 (2005).

[12] M. W. Haverkort, Z. Hu, W. Tanaka, A.and Reichelt, S. Streltsov, M. Korotin, V. Anisimov, H. Hsieh, H.-J. Lin, C.-T. Chen, D. Khomskii, and L. H. Tjeng, Phys. Rev. Lett. **95**, 196404 (2005).

[13] T. Koethe, Z. Hu, M. Haverkort, C. Schüßler-Langeheine, F. Venturini, N. Brookes, O. Tjernberg, W. Reichelt, H. Hsieh, H.-J. Lin, C.-T. Chen, and L. Tjeng, Phys. Rev. Lett. **97**, 116402 (2006).

[14] T. Mizokawa, L. Tjeng, G. Sawatzky, G. Ghiringhelli, O. Tjernberg, N. Brookes, H. Fukazawa, S. Nakatsuji, and M. Y., Phys. Rev. Lett. **87**, 077202 (2001).

[15] T. Mizokawa, L. Tjeng, H. Hsieh, H.-J. Lin, C. Chen, S. Schuppler, S. Nakatsuji, H. Fukazawa, and M. Y., Phys. Rev. B **69**, 132410 (2004).

[16] H.-J. Noh, S. J. Oh, B. G. Park, J.-H. Park, J. Y. Kim, H. D. Kim, T. Mizokawa, H.-J. Tjeng, L. H.and Lin, C. T. Chen, S. Schuppler, S. Nakatsuji, H. Fukazawa, and Y. Maeno, Phys. Rev. B **72**, 052411 (2005).

[17] Hua Wu, Z. Hu, T. Burnus, J. Denlinger, P. Khalifah, D. Mandrus, L.-Y. Jang, H. Hsieh, A. Tanaka, K. Liang, J. Allen, R. Cava, D. Khomskii, and L. Tjeng, Phys. Rev. Lett. **96**, 256402 (2006).

[18] D. MacLean, J. of Solid State Chem. **30**, 35 (1979).

[19] M. Eitel and J. E. Greedan, J. Less Common Metals **116**, 076402 (1986).

[20] M. Cwik, T. Lorenz, J. Baier, R. Müller, G. André, F. Bourée, F. Lichtenberg, A. Freimuth, R. Schmitz, E. Müller-Hartmann, and M. Braden, Phys. Rev. B **68**, 060401 (2003).

[21] J. P. Goral and J. E. Greedan, J. Magnetism Magnetic Materials **37**, 315 (1983).

[22] G. Meijer, W. Heggeler, J. Brown, O.-S. Becker, J. Bednorz, C. Rossel, and P. Wachter, Phys. Rev. B **59**, 11832 (1999).

[23] T. Mizokawa and A. Fujimori, Phys. Rev. B **54**, 5368 (1996).

[24] B. Keimer, D. Casa, A. Ivanov, J. Lynn, M. von Zimmermann, J. Hill, D. Gibbs, Y. Taguchi, and Y. Tokura, Phys. Rev. Lett. **85**, 3946 (2000).

[25] G. Khaliullin and S. Maekawa, Phys. Rev. Lett. **85**, 3950 (2000).

## BIBLIOGRAPHY

[26] M. Mochizuki and M. Imada, Phys. Rev. Lett. **91**, 167203 (2003).

[27] E. Pavarini, S. Biermann, A. Poteryaev, A. I. Lichtenstein, A. Georges, and O. K. Andersen, Phys. Rev. Lett. **92**, 176403 (2004).

[28] I. V. Solovyev, Phys. Rev. B **69**, 134403 (2004).

[29] M. W. Haverkort, Z. Hu, A. Tanaka, G. Ghiringhelli, H. Roth, M. Cwik, T. Lorenz, C. Schüßler-Langeheine, S. V. Streltsov, A. S. Mylnikova, V. I. Anisimov, C. de Nadai, N. B. Brookes, H. H. Hsieh, H.-J. Lin, C. T. Chen, T. Mizokawa, Y. Taguchi, Y. Tokura, D. I. Khomskii, and L. H. Tjeng, Phys. Rev. Lett. **94**, 056401 (2005).

[30] N. Mott, Metal-Insulator Transitions, 1990.

[31] A. Fujimori, I. Hase, H. Namatame, Y. Fujishima, Y. Tokura, H. Eisaki, S. Uchida, K. Takegahara, and F. M. F. de Groot, Phys. Rev. Lett. **69**, 1796 (1992).

[32] A. Fujimori, I. Hase, M. Nakamura, H. Namatame, Y. Fujishima, Y. Tokura, M. Abbate, F. M. F. de Groot, M. T. Czyzyk, J. C. Fuggle, O. Strebel, F. Lopez, M. Domke, and G. Kaindl, Phys. Rev. B **46**, 9841 (1992).

[33] A. Fujimori, I. Hase, Y. Tokura, M. Abbate, F. M. F. de Groot, J. C. Fuggle, H. Eisaki, and S. Uchida, Physica B **186**, 981 (1993).

[34] I. H. Inoue, I. Hase, Y. Aiura, A. Fujimori, Y. Haruyama, T. Maruyama, and Y. Nishihara, Phys. Rev. Lett. **74**, 2539 (1995).

[35] Y. Okimoto, T. Katsufuji, Y. Okada, T. Arima, and Y. Tokura, Phys. Rev. B **51**, 9581 (1995).

[36] K. Morikawa, T. Mizokawa, K. Kobayashi, A. Fujimori, H. Eisaki, S. Uchida, F. Iga, and Y. Nishihara, Phys. Rev. B **52**, 13711 (1995).

[37] K. Morikawa, T. Mizokawa, A. Fujimori, Y. Taguchi, and Y. Tokura, Phys. Rev. B **54**, 8446 (1996).

[38] J. Park, Ph.D. thesis, University of Michigan, 1994.

[39] D. Schrupp, M. Sing, T. M., H. Fujiwara, S. Kasai, S. A., T. B.-V. Suga, S. Muro, and R. Claessen, Europhys. Lett. **70**, 789 (2005).

[40] C. Laubschat, E. Weschke, C. Holtz, M. Domke, O. Strebel, and G. Kaindl, Phys. Rev. Lett. **65**, 1639 (1990).

[41] E. Weschke, C. Laubschat, T. Simmons, M. Domke, O. Strebel, and G. Kaindl, Phys. Rev. B **44**, 8304 (1991).

[42] E. Weschke, A. Höhr, G. Kaindl, S. L. Molodtsov, S. Danzenbächer, M. Richter, and C. Laubschat, Phys. Rev. B **58**, 3682 (1998).

[43] Y. Kucherenko, S. L. Molodtsov, M. Heber, and C. Laubschat, Phys. Rev. B **66**, 155116 (2002).

[44] A. Sekiyama, T. Iwasaki, K. Metsuda, Y. Saitoh, Y. Onuki, and S. Suga, Nature (London) **403**, 396 (2000).

[45] A. Sekiyama, H. Fujiwara, S. Imada, S. Suga, H. Eisaki, S. I. Uchida, K. Takegahara, H. Harima, Y. Saitoh, I. A. Nekrasov, G. Keller, D. E. Kondakov, A. V. Kozhevnikov, T. Pruschke, K. Held, D. Vollhardt, and V. I. Anisimov, Phys. Rev. Lett. **93**, 156402 (2004).

[46] R. Eguchi *et al.*, Phys. Rev. Lett. **96**, 076402 (2006).

[47] W. Metzner and D. Vollhardt, Phys. Rev. Lett. **62**, 324 (1989).

[48] M. Jarrell, Phys. Rev. Lett. **69**, 168 (1992).

[49] X. Y. Zhang, M. J. Rozenberg, and G. Kotliar, Phys. Rev. Lett. **70**, 1666 (1993).

[50] A. Georges, G. Kotliar, W. Krauth, and M. J. Rozenberg, Rev. Mod. Phys. **68**, 13 (1996).

[51] I. A. Nekrasov, G. Keller, D. E. Kondakov, A. V. Kozhevnikov, T. Pruschke, K. Held, D. Vollhardt, and V. I. Anisimov1, Phys. Rev. B **72**, 155106 (2005).

[52] H. Roth, Master's thesis, Universität zu Köln, 2003.

[53] U. Müller, Anorganische Strukturchemie, 1996.

[54] V. M. Goldschmidt, Geometrische Verteilungsgesetze der Elemente, 1927/28.

## BIBLIOGRAPHY

[55] J. B. Goodenough and J. M. Lomgo, Landolt-Börnstein Tabellen (New Series), 1970.

[56] A. M. Glazer, Acta Cryst. **B28**, 751 (1972).

[57] A. C. Komarek, H. Roth, M. Cwik, W.-D. Stein, J. Baier, M. Kriener, F. Bouree, T. Lorenz, and M. Braden, Phys. Rev. B **75**, 224402 (2007).

[58] J. Hester, Acta Crystallografica B **5**, 739 (1997).

[59] J. E. Greedan, J. Less Common Metals **111**, 335 (1985).

[60] T. Katsufuji, Y. Taguchi, and Y. Tokura, Phys. Rev. B **56**, 10145 (1997).

[61] J. Goral, J. E. Greedan, and D. A. MacLean, J. of Solid State Chem. **43**, 244 (1982).

[62] J. B. Goodenough, Phys. Rev. **100**, 564 (1955).

[63] J. Kanamori, J. Phys. C – Solid State Phys. **10**, 87 (1959).

[64] P. W. Anderson, Phys. Rev. **155**, 2 (1959).

[65] Y. Tokura, Y. Taguchi, Y. Moritomo, K. Kumagai, T. Suzuki, and Y. Iye, Phys. Rev. B **48**, 14063 (1993).

[66] R. Rückamp, E. Benckiser, M. W. Haverkort, H. Roth, T. Lorenz, A. Freimuth, L. Jongen, A. Möller, G. Meyer, P. Reutler, B. Büchner, A. Revcolevschi, S.-W. Cheong, C. Sekar, G. Krabbes, and M. Grüninger, New J. Phys. **7**, 144 (2005).

[67] I. Solovyev, N. Hamada, and K. Terakura, Phys. Rev. B **53**, 7158 (1996).

[68] H. Sawada and K. Terakura, Phys. Rev. B **58**, 6831 (1998).

[69] S. Okatov, A. Poteryaev, , and A. Lichtenstein, Europhys. Lett. **70**, 499 (2005).

[70] O. K. Andersen and O. Jepsen, Phys. Rev. Lett. **53**, 2571 (1984).

[71] E. Pavarini, A. Yamasaki, J. Nuss, and O. Andersen, New J. Phys. **7**, 188 (2005).

[72] A. Freimuth, Magnetismus, Vorlesungsskript, 2001.

[73] S. Blundell, Magnetism in Condensed Matter, 2001.

[74] M. Mochizuki and M. Imada, New J. Phys. **7**, 144 (2005).

[75] J. Akimitsu, H. Ichikawa, N. E. T. Miyano, M. Nishi, and K. Kakurai, J. Phys. Soc. Japan **70**, 3052 (2001).

[76] A. Smakula, Einkristalle, 1962.

[77] W. G. Pfann, Zone Melting, 1958.

[78] H. Oppermann, Vanadiumoxide, 1983.

[79] U. Ammerahl, Ph.D. thesis, Universität zu Köln, 2003.

[80] *Optical floating zone system FZ - 10000 - H - VI - VP*, Crystal Systems Inc.

[81] M. Mühlberg, Theorie der Kristallzucht, Vorlesungsskript, 2001.

[82] K. T. Wilke, Methoden der Kristallzüchtung, 1963.

[83] F. Rosenberger, Fundamental of Crysal Growth, 1979.

[84] M. Benomar, Ph.D. thesis, Universität zu Köln, 2007.

[85] A. Reichl, Master's thesis, Universität zu Köln, 2002.

[86] M. Reuther, Master's thesis, Universität zu Köln, 2005.

[87] A. Komarek, Master's thesis, Universität zu Köln, 2005.

[88] A. C. Komarek, Ph.D. thesis, Universität zu Köln, .

[89] M. Cwik, Master's thesis, Universität zu Köln, 2002.

[90] F. Lichtenberg, D. Widmer, J. Bednorz, T. Williams, and A. Reller, Z. Physik B – condensed matter **82**, 211 (1991).

[91] A. Nugruho, private communication.

[92] Revised and Suplementary Tables Band IV, 1974.

## BIBLIOGRAPHY

[93] J. Rodriguez-Carvajal, An Introduction to the Programm FullProf 2000, http://www-llb.cea.fr/fullweb/fp2k/fp2k.htm.

[94] M. Braden, private communication.

[95] C. C. Hays, J.-S. Zhou, J. T. Markert, and J. B. Goodenough, Phys. Rev. B **60**, 10367 (1999).

[96] Z. Hu, unpublished.

[97] N. Hollman, Master's thesis, Universität zu Köln, 2006.

[98] F. Iga, T. Naka, T. Matsumoto, N. Shirakawa, K. Murata, and Y. Nishihara, Physica B **224**, 526 (1996).

[99] K. Kato, E. Nishibori, M. Takata, M. Sakata, T. Nakano, K. Uchihira, M. Tsubota, F. Iga, and T. Takabatake, J. Phys. Soc. Jpn. **71**, 2082 (2002).

[100] H. Roth, unpublished.

[101] G. Amow, N. Raju, and J. Greedan, J. of Solid State Chem. **155**, 177 (2000).

[102] G. Amow, J. of Solid State Chem. **141**, 262 (98).

[103] G. Amow, J. of Solid State Chem. **121**, 443 (1996).

[104] W. Reichelt, private communication.

[105] A. Einstein, Annalen der Physik **17**, 17 (1905).

[106] S. Hüfner, Photoelectron Spectroscopy, 2003.

[107] M. Prutton, Introduction to Surface Physics, 1994.

[108] A. Sekiyama, H. Fujiwara, S. Imada, S. Suga, H. Eisaki, S. I. Uchida, K. Takegahara, H. Harima, Y. Saitoh, I. A. Nekrasov, G. Keller, D. E. Kondakov, A. V. Kozhevnikov, T. Pruschke, K. Held, D. Vollhardt, and V. I. Anisimov, Phys. Rev. Lett. **93**, 156402 (2004).

[109] J. W. Allen, S. J. Oh, O. Gunnarsson, K. Schönhammer, M. B. Maple, M. S. Torikachvili, and I. Lindau, Ann. Phys. **35**, 275 (1986).

[110] I. H. Inoue, O. Goto, H. Makino, N. E. Hussey, and M. Ishikawa, Phys. Rev. B **58**, 4372 (1998).

[111] J. Hubbard, Proc. Roy. Soc. A **276**, 238 (1963).

[112] J. Hubbard, Proc. Roy. Soc. A **277**, 237 (1964).

[113] J. Hubbard, Proc. Roy. Soc. A **281**, 401 (1963).

[114] W.F.Brinkman and T. M. Rice, PRB **2**, 4302 (1970).

[115] R. Hesper, Ph.D. thesis, University of Groningen, 2000.

[116] S.-K. Mo, J. D. Denlinger, H.-D. Kim, J.-H. Park, J. W. Allen, A. Sekiyama, A. Yamasaki, K. Kadono, S. Suga, Y. Saitoh, T. Muro, P. Metcalf, G. Keller, K. Held, V. Eyert, V. I. Anisimov, and D. Vollhardt, Phys. Rev. Lett. **9o**, 186403 (20043).

[117] A. Tanaka, J. Phys. Soc. Japan **73**, 152 (2004).

[118] S. W. Robey, L. T. Hudson, C. Eylem, and B. Eichorn, Phys. Rev. B **48**, 562 (1993).

[119] S. W. Robey, V. E. Henrich, C. Eylem, and B. W. Eichhorn, Phys. Rev. B **52**, 2395 (1995).

[120] T. Yoshida, A. Ino, T. Mizokawa, A. Fujimori, Y. Taguchi, T. Katsufuji, , and Y. Tokura, Europhys. Lett. **59**, 258 (2002).

[121] C. Ulrich, G. Khaliullin, S. Okamoto, M. Reehuis, A. Ivanov, H. He, Y. Taguchi, Y. Tokura, and B. Keimer, Phys. Rev. Lett. **89**, 167202 (2002).

[122] P. Blaha, K. Schwarz, G. Madsen, D. Kvasnicka, and J. Luitz, http://www.wien2k.at .

[123] V. I. Anisimov, I. V. Solovyev, M. A. Korotin, M. T. Czyżyk, and G. A. Sawatzky, Phys. Rev. B **48**, 16929 (1993).

[124] S. Moukouri and M. Jarrell, Phys. Rev. Lett. **87**, 167010 (2001).

[125] T. Maier, M. Jarrell, T. Pruschke, and M. H. Hettler, Rev. Mod. Phys. **77**, 1027 (2005).

# BIBLIOGRAPHY

[126] E. Dagotto, Rev. Mod. Phys. **66**, 763 (1994).

[127] P. Béran, D. Poilblanc, and R. B. Laughlin, Nucl. Phys. B **473**, 707 (1996).

[128] R. Eder and Y. Ohta, Phys. Rev. B **56**, 2542 (1997).

[129] O. Gunnarsson, E. Koch, and R. M. Martin, Phys. Rev. B **54**, R11026 (1996).

[130] O. Gunnarsson, E. Koch, and R. M. Martin, Phys. Rev. B **56**, 1146 (1997).

[131] E. Koch, O. Gunnarsson, and R. M. Martin, Phys. Rev. B **60**, 15714 (1999).

# Acknowledgements

An dieser Stelle möchte ich die Gelegenheit nutzen um all denjenigen Menschen zu danken, die zum Erfolg dieser Arbeit beigetragen haben.

Zuallererst gilt mein Dank natürlich meinem Doktorvater, Hao Tjeng. Du hast mich in Deiner Arbeitsgruppe willkommen geheißen und es mir dadurch erst ermöglicht diese Arbeit anzufertigen. Außerdem brachtest Du mir das gesamte Spektrum der Grundlagenforschung im Bereich der Übergangsmetalloxide näher. Durch Dich wurde ich bis buchstäblich zur letzten Minute, speziell in den letzten Tagen vor der Abgabe betreut. Hierfür muss ich mich auch bei Deiner Familie bedanken, die auf ihren Vater und Ehemann verzichten mussten.

Mein weiterer Dank gilt dem 2. Gutachter dieser Arbeit, Markus Grüninger. Schon seit Beginn meiner Diplom ... sogar schon vorher im Oberseminar ... hattest Du stets ein offenes Ohr bei Fragen bezüglich der Physik im allgemeinen und der optischen Leitfähigkeit im besonderen. Als sehr angenehm empfand ich auch die Zusammenarbeit mit deiner Forschungsgruppe.

Danken möchte ich auch Herrn Ladislav Bohaty, dem Vorsitzenden der Prüfungskommision, für die Übernahme dieses Amtes.

Der gesamten Arbeitsgruppe Tjeng danke ich, in der ich sehr herzlich aufgenommen wurde. Hier sei zuallererst dem Chef, Zhiwei Hu, gedankt für die Leitung und Betreuung der Soft X-ray Experimente. Durch Dich wurde die Messreise nach Taiwan zu einem einzigartigen Erlebnis. Neben der wissenschaftlichen Seite hast Du mir auch die chinesische Kultur und speziell die chinesische Küche näher gebracht. Die freudschafliche Athmosphäre auch über die Forschungsarbeit hinaus habe ich sehr genossen.

Im Bereich der Photoemmisonsspektroskopie sei besonders Thomas Koethe gedankt, der bei der Durchführung dieser Experiment federführend war. Des weiteren organisierte er auch den Abgabe dieser Arbeit in den letzten Wochen, wodurch mir so manches Pendeln zwischen Leverkusen und der

# Erklärung

Ich versichere, dass ich die von mir vorgelegte Dissertation selbständig angefertigt, die benutzten Quellen und Hilfsmittel vollständig angegeben und die Stellen der Arbeit - einschließlich Tabellen, Karten und Abbildungen -, die anderen Werken im Wortlaut oder dem Sinn nach entnommen sind, in jedem Einzelfall als Entlehnung kenntlich gemacht habe; dass diese Dissertation noch keiner Fakultät oder Universität zur Prüfung vorgelegen hat; dass sie - abgesehen von unten angegebenen Teilpublikationen - noch nicht veröffentlicht worden ist sowie, dass ich eine solche Veröffentlichung vor Abschluss des Promotionsverfahrens nicht vornehmen werde. Die Bestimmungen dieser Promotionsordnung sind mir bekannt. Die von mir vorgelegte Dissertation ist von Prof. Dr. L. H. Tjeng betreut worden.

Holger Roth

# Publications

*Raman scattering in the mott insulators $LaTiO_3$ and $YTiO_3$: Evidence for orbital excitations*
C. Ulrich, A. Gössling, M. Grüninger, M. Guennou, H. Roth, T. Lorenz, G. Khaliullin, and B. Keimer,
Phys. Rev. Lett. **97**, 157401 (2006).

*Magnetic heat transport in $R_2CuO_4$ (R=La, Pr, Nd, Sm, Eu, and Gd)*
K. Berggold, T. Lorenz, J. Baier, M. Kriener, D. Senff, H. Roth, A. Severing, H. Hartmann, A. Freimuth, S. Barilo and F. Nakamura,
Physical Review B **73**, 104430 (2006).

*Optical study of orbital excitations in transition-metal oxides*
R. Rückamp, E. Benckiser, M. W. Haverkort, H. Roth, T. Lorenz, A. Freimuth, L. Jongen, A. Möller, G. Meyer, P. Reutler, B. Büchner, S.W. Cheong, C. Sekar, G. Krabbes and M. Grüninger,
New J. Phys. **7**, 144 (2005).

*Determination of the orbital moment and crystal field splitting in $LaTiO_3$.*
M. W. Haverkort, Z. Hu, A. Tanaka, G. Ghiringhelli, H. Roth, M. Cwik, T. Lorenz, C. Schueßler-Langeheine, S. V. Streltsov, A. S. Mylnikova, V. I. Anisimov, C. de Nadai, N. B. Brookes, H. H. Hsieh, H.-J. Lin, C. T. Chen, T. Mizokawa, Y. Taguchi, Y. Tokura, D. I. Khomskii, and L. H. Tjeng,
Physical Review Letters **94**, 056401 (2005); cond-mat/0405516.

*Magnetoelastic coupling in $RETiO_3$ (RE = La, Nd, Sm, Gd, Y)*
A. C. Komarek, H. Roth, M. Cwik, W.-D. Stein, J. Baier, M. Kriener, F. Bourée, T. Lorenz and M. Braden,
Physical Review B **73**, 104430 (2006).

*Pressure driven orbital reorientation and change in Mott-Hubbard gap in YTiO₃*
I. Loa, X. Wang K. Syassen, H. Roth, T. Lorenz, M. Hanfland and Y. L. Mathis
J PHYS-CONDENS MAT **19**, 406223 (2007); cond-mat/0504383.

*Mott-Hubbard excitations in YTiO₃ probed by ellipsometry*
A. Gössling, R. Schmitz, H. Roth, T. Lorenz, J. A. Maydosh, E. Müller-Hartmann and M. Grüninger
Submitted to Physical Review Letters; cond-mat/0608531.

*Spectral weight distributions of d1 Mott insulators LaTiO₃ and YTiO₃*
H. Roth, T. C. Koethe, H. Wu, M. W. Haverkort, Z. Hu, T. Lorenz, I. S. Elfimov, G. A. Sawatzky, and L. H. Tjeng
Submitted to Physical Review Letters.

# Curriculum vitae

**Persönliche Daten**

| | |
|---|---|
| Name | Holger Roth |
| Geburtsdatum | 22 April 1973 |
| Geburtsort | Siegen |
| Staatsangehörigkeit | deutsch |
| Personenstand | ledig |

**Studium**

| | |
|---|---|
| Juli 1992 | Abitur |
| Oktober 1994 - September 2003 | Universität zu Köln |
| | Diplom in Physik |
| Oktober 2003 | Beginn der Doktorarbeit am II. Physikalischen Institut, Universität zu Köln |